SYSTEMATIC ANALYSIS OF TGF-β SIGNALING AND ACTIVATION IN LIVER FIBROSIS

WANG JUNJIE
(*B.S., Fudan University*)

A THESIS SUBMITTED

FOR THE DEGREE OF DOCTOR OF PHILOSOPHY

IN COMPUTATIONAL SYSTEMS BIOLOGY (CSB)

SINGAPORE-MIT ALLIANCE

NATIONAL UNIVERSITY OF SINGAPORE

2013

DECLARATION

I hereby declare that this thesis is my original work and it has been written by me in its entirety. I have duly acknowledged all the sources of information which have been used in the thesis.

This thesis has also not been submitted for any degree in any university previously.

Wang Junjie

25 January 2013

Acknowledgements

I would like to express my deepest gratitude to my supervisors, Prof. Hanry Yu, Prof. Jacob K. White, and Prof. P. S. Thiagarajan. They are not only great scientists who guided me to through all kinds of research problems with their brilliant mind, but also great mentor who focused on education of students. Prof. Yu is an open-minded biologist and does excellent integrative science. I appreciate that he could spend a lot of time in understanding computational problems and provide me insights into the biological implications behind. Prof. Thiagarajan's advices are always sharp and helpful. He is very good at picking up the emphasis and helping me get focused. I am especially grateful to Prof. White. His patience helped me a lot with my mathematics when I started my Ph.D. study as a biologically trained student. The way he thinks about scientific problems as well as they way he educates students influenced me a lot. These would further influence me as I move on in the way I reason and the way I treat other people.

Besides my supervisors, I would also like to thank Dr. Lisa Tucker-Kellogg. She is a great computational biologist who is very knowledgeable in both computational and biological sides. She gave me a lot of important suggestions during our collaboration. It is also a pleasure to join her group of computational biology. I would like to thank all the members in this group for their discussions and suggestions.

It was a great time when I started to learn basics of computational biology and modeling in MIT. At that time, many members in Prof. White's lab and Prof.

Bruce Tidor's lab was greatly helpful. I would like to especially thank Bo Kim, Jared Toettcher and Caitlin Bever for their patient guidance about very basic tutorials and knowledge of computational biology.

I would like to thank all the lab members in Prof. Yu's lab for their help in biological experiments. Chia Ser Mien and Lakshmi Venkatraman helped me understand TGF-β and its role in liver fibrosis. Ng Inn Chuan helped me with some experimental techniques.

I also appreciate the time when I study together with my classmates in the Computational Systems Biology program of Singapore-MIT Alliance. Among all classmates, I especially thank Shi Yuan for the collaboration and discussion on many aspects of my research.

Finally, I want to thank Singapore-MIT Alliance for the scholarship and research funding. The officers in SMA were also very kind and helpful. It was a great experience studying in Singapore and MIT. I would be absolutely benefit from these years of experience in the rest of my life.

Table of Contents

Summary

Transforming growth factor-β (TGF-β) is a key cytokine in liver fibrosis. It induces the activation of hepatic stellate cells (HSCs) leading to its expression of excessive extra-cellular matrix (ECM). TGF-β is expressed in its latent form and it needs to be activated to be functional. Previous studies have modeled a network of TGF-β activation in liver fibrosis regarding two major players, plasmin and Thrombospondin-1 (TSP1). TGF-β regulates cellular responses mainly through the Smad signaling pathway. In this network model of TGF-β activation, two species were regulated by TGF-β through Smad signaling, but this model treated the Smad pathway as a black box.

We then first aimed to study the Smad signaling pathway using computational modeling. In this work, we used tightly coupled model analysis and experiments to systematically study the negative regulatory mechanisms in this pathway. Superisingly, we found no combinations of known mechanisms could explain the dynamics of phosphorylated R-Smad, the output species of this pathway. We then sought to find alternative mechanisms. Finally we concluded with a model with PPM1A, the phosphatase upregulated by TGF-β. This model was validated by our experiments and could explain all observations of phosphorylated R-Smad.

After we had the updated model of downstream Smad pathway, we could possibly integrate it with the previous upstream network of TGF-β activation. This was not a simple integration as we noticed that the two species regulated by TGF-β signaling in the upstream network should be averaged responses from a population

of cells. An efficient algorithm to simulate the population behavior could be useful for our integration of two networks. We then developed two efficient algorithms to approximate cell population behavior and applied one of them, Population ODE to the integration of two networks. The integrated model maintained the bistable behavior and our algorithms could also be applied to other systems in which cell-population behavior needs to be considered.

Finally, we moved one step further from the population-level model to study the bistable switch of the TGF-β activation network in space. As we know that fibrotic regions often distribute unevenly in liver fibrosis. How the fibrotic regions and normal regions of liver tissue could affect each other remained a question. It is difficult to study the spatial dynamics using biologcial experiments but computational modeling could provide some hints. Our modeling assumed diffusion of molecules in space. This diffusion effect could cause a traveling wave of species steady states in space. Based on our simulations and experimental test, we could infer that normal liver tissue has the capability of switching the state of its neighbouring fibrotic tissue. Our simulations also predicted that this switching could be slowed down because of excessive ECM accumulation. This could be an explanation to how liver fibrosis is induced by chronic injury.

List of Tables

List of Figures

List of Symbols

TGF-β: Transforming Growth Factor-β

PAI1: Plasminogen Activator Inhibitor-1

TSP1: Thrombospondin-1

HSC: Hepatic Stellate Cell

ECM: Extracellular Matrix

ODE: Ordinary Differential Equation

R-Smad: Receptor-regulated Smad

I-Smad: Inhibitor Smad

Phospho-R-Smad: phosphorylated R-Smad

T1R: Type I Receptor

PPM1A: Protein Phosphatase 1A

1 Chapter 1: Introduction

The discovery of DNA and central dogma of molecular biology back in 1950s exploded biological studies. Basic molecular biological tools such as PCR and western blotting were developed afterwards promoting the studies of individual genes and proteins. Most of biological phenotypes are based on the functions of genes and proteins, and these functions are performed mainly by networks of protein-protein interactions and gene regulations. All the genes and proteins are connected in some way to form a complex system that works like a machine, but a much more complicated one than what human beings can build. Lead by the human genome project in the early 2000s and functional genomics, a large amount of data about genes and proteins were generated. Newly developed techniques such as microarray, RNAi, and immunofluorescence imaging allow high-throughput, more efficient and more accurate measurement of biological systems. With increasing efforts made in biological research and accumulating knowledge and data from biological studies, pieces in a large biological system, such as a signaling pathway were connected. This led us to look at biological systems from a systematic view, putting all genes or proteins that have interactions together. Then, systems biology emerges as a new type of approach in biological science.

Systems biology, a concept have been widely used since 2000s, focuses on the study of biological systems as a whole, considering all species involved in a system and the interactions between species. This concept is somehow opposite to traditional molecular biological studies, in which elements or factors were taken

apart and often a single element or factor was emphasized to have the most important effect to a certain biological phenomenon. However, after more and more of these factors have been discovered, it is now a common sense that a biological phenomenon is often affected by multiple factors. High complexity is a nature of biological systems. The more components in the systems we discover, the more complex we realize they are. Therefore, without knowing how these components interact with each other to form and manipulate the system, we cannot fully understand the system. If we think the traditional molecular biology type of approach to be a top-down approach that breaks up each component in a system to study its role, systems biology type of approach is a bottom-up approach that integrates the components discovered or identified by the top-down approach. This bottom-up approach is necessary because the final goal of all biological research is to either change a biological system from outside, or maintain a system in the presence of outside changes. When any change or perturbation is applied to a biological system, the system itself will behave as a whole and we need to understand its behavior from a systematic point of view.

The systems biology approach often utilizes computational models to integrate the biological data. There are various ways of building models for biological systems (Different modeling methods will be introduced in Chapter 2: Background and Related Work), but there is a general discipline of systems biology modeling. Modeling in systems biology generally goes through a cyclic process of theory, modeling, model-driven hypothesis, experimental validation, refinement of theory and models (Alberghina and Westerhoff, 2005). In most cases, the available

biological data is much less than the data required to build an enough complete or accurate model. Therefore, models of a biological system is also usually updated and refined step by step and from study to study. Computational modeling has been applied to a variety of biological systems and predicts systematic behaviors that are non-intuitive from just examining a single part of the system. Computational modeling has also been used to study the activation of a key cytokine, TGF-β in liver fibrosis. It has also been shown that the activation of TGF-β exhibits a bistable behavior in liver fibrosis. This is an initiative work to study the systematic behavior of TGF-β in liver fibrosis. However, some aspects of this model of TGF-β activation could be improved. In the following section, we introduce why and how we planned to contribute to the modeling of TGF-β related network in liver fibrosis.

1.1 Context and Motivations

Liver fibrosis is a disease affecting hundreds of millions of patients globally. The end stage of liver fibrosis, cirrhosis, may further lead to liver failure and liver cancer, causing millions of death worldwide every year. Major causes of liver fibrosis include chronic viral hepatitis, alcohol abuse (Iredale, 2007). Liver fibrosis is a would-healing process which is potentially reversible. It has been found in many studies that after removing the source of liver injury, liver fibrosis is regressed spontaneously (Hammel et al., 2001, Benyon and Iredale, 2000). However, some sources of liver injury are sustained and hard to be removed or stopped, such as viral hepatitis. Thus, therapies of liver fibrosis have focused on both removal of

liver injury and targeting liver fibrosis regression. In order to target liver fibrosis regression, understanding of the mechanisms of liver fibrosis progression and regression is important.

During liver fibrosis progression, a major change of the liver tissue is the accumulation of excessive extracellular matrix (ECM) (Arthur, 1997). Hepatic stellate cells (HSCs) are the primary source of the ECM (Bataller and Brenner, 2005, Friedman, 2003). HSCs are quiescent in normal liver but activated in fibrotic liver. In its quiescent state, ECM production and degradation is balanced, while in its activated state, excessive ECM proteins are produced. The activation of HSCs is primary in liver fibrosis progression and understanding of its activation process is crucial in finding targets to block this process and further block fibrosis progression (Kinnman et al., 2001, Iredale et al., 1998).

TGF-β is one of the key cytokine that can induce the activation of HSCs (Gressner and Weiskirchen, 2006, Gressner et al., 2002). Several studies have targeted TGF-β related signaling and regulations as therapies for liver fibrosis (Kondou et al., 2003, Currier et al., 2003, Salgado et al., 2000). TGF-β is expressed in its latent form (latent TGF-β), enclosed by the latency-associated protein (LAP) (Annes et al., 2003). Many activator and activation process can release active TGF-β from LAP. These activators and activation process could form a complex network that regulates TGF-β. Active TGF-β then binds to receptors on the cell surface and induces Smad signaling cascade inside the cell to regulate gene expression (Shi and Massague, 2003, Attisano and Wrana, 2002, Massague and Wotton, 2000). Smad signaling is tightly controlled by downstream regulations.

This thesis was first motivated by lack of understanding of downstream Smad signaling regulations. Therefore, we initiated our study from systematic analysis of Smad signaling pathway. Different negative regulatory mechanisms in Smad pathway have been studied biologically and individually built into computational models. However, the roles of these mechanisms in regulating Smad signaling have not been compared. We used computational models to analyze each mechanism and combination of mechanisms. Model-based predictions and experimental validations provided us new insights into Smad pathway negative regulations. This part is a cellular level study of TGF-β in liver fibrosis.

Secondly, previous work has shown that the activation of TGF-β in liver fibrosis may exhibit a bistable behavior (Venkatraman et al., 2012), meaning that the TGF-β concentration may stay at two different steady states. The two steady state of TGF-β could switch back and forth by external perturbations to the system of TGF-β regulation. This network of TGF-β upstream activation consists of many reactions in the ECM and assumes cells are identical to each other. It is known that cell-to-cell variability is common in many types of cell populations. Cell-to-cell variability may affect the bistable behavior of the system. We therefore wanted to integrate our downstream Smad signaling model with the upstream TGF-β activation network and to see if the bistability could be affected by cell-to-cell variability. Simulating a population of cells is a computationally expensive task. To achieve our goal, we developed efficient algorithms for simulating signaling pathway in a population of cells. This part is a cell-population level study of TGF-β in liver fibrosis.

Last but not least, fibrotic tissue in liver fibrosis does not distribute evenly in space. As Venkatraman's model shows bistability of TGF-β activation, two steady states of TGF-β levels may also be present in different region of liver tissue. We therefore wanted to study how two steady states of TGF-β regulation network would affect each other in space. By assuming simple diffusion/transportation effect of molecules in the ECM, we were able to simulate the behavior of bistable system in space. This part is a tissue level study of TGF-β in liver fibrosis.

1.2 Our Approaches and Contributions

As mentioned, we use systems biology methods to study the TGF-β related regulations at three different levels: cellular level, cell-population level and tissue level. Since different levels of regulation have distinct behaviors, we use different approaches for different levels of study.

For cellular level of TGF-β regulation, we studied the TGF-β signaling pathway within the cells. We used ODEs to build computational models to study different mechanisms of downstream regulation in TGF-β signaling pathway. The ODE models were based on mass action law of chemical reactions and they were able to simulate the time variant of reaction species concentrations. This approach allowed us to observe and analyze the dynamics of each step in this pathway. Besides using ODE as the modeling approach, we utilize parameter estimation to fit our model to experimental data and to closely look at the relationship between different regulatory mechanisms in TGF-β signaling pathway and the dynamics of the signal

transduction. ODE modeling allowed us to analyze detailed dynamics such as timing of different events. With this analysis, we found that there needs to be at least one “fast-mode” mechanism and one “slow-mode” mechanism to explain the dynamics of TGF-β signaling. However, modeling analysis combined with experimental measurements suggested that known mechanisms were not sufficient to explain the observed dynamics. This could not be discovered without ODE modeling. We then utilized the models to help us find possible alternatives. Model prediction and experimental validation showed that PPM1A, the phosphatase was upregulated in the presence of TGF-β. Our study showed that system level of analysis was able to refine some qualitative knowledge in biological discoveries and gain insights beyond a collection of biological information.

For the cell-population level of TGF-β regulation, we wanted to integrate the models of upstream network of TGF-β activation and the downstream Smad pathway. Since the upstream network is in the ECM, the molecules regulated by Smad signaling in this network should be the average response of a population of cells. Thus, what we really needed was to integrate the upstream network and a population of Smad pathway. There is a naïve way of simulating cell population behavior, which is called Monte Carlo simulation. It simply takes random samples of the parameters of a system and then simulates all samples to approximate the population behavior. However, this method is often time consuming as the biological system is often complex and the sample size needs to be large. In the case of integrating two networks of TGF-β regulation, this type of sampling-based could not synchronize the species existing in both networks. Therefore, we first developed

an algorithm, Population ODE, which was more efficient than Monte Carlo simulation and not sampling-based. This approach approximated the population behavior by a new ODE system derived from single-cell ODE model. Because it is still an ODE system, it is easy to integrate a population of Smad pathways with the upstream network using this approach. This is a good approach and we wanted to extend its application. We found it works well in some well known pathway models. However, this algorithm did not approximate bistable system well. We then moved on to develop the second algorithm called Sample Reduction method, which is based on Monte Carlo simulation, however with significantly reduced the sample size. This method is a sampling type of method so that it can be applied to all types of systems. Sample reduction was tested in this method in apoptosis pathway, a well-known bistable system. The results showed that it significantly reduced sample size compared to Monte Carlo simulation.

For the tissue level of TGF-β regulation, we built a spatial model of TGF-β upstream regulations. In this study, we integrated the effect of diffusion of molecules and the reactions of molecules to have a reaction-diffusion system, and we discretized the space so that we can use ODE system to simulate the effect of diffusion. As the TGF-β upstream regulations have a bistable behavior, this particular reaction-diffusion system showed a wave of bistable switch in space. This kind of behavior has been proven analytically in the field of physics but has not been shown in biological systems. Our simulation also showed that the ECM accumulation in liver fibrosis would slow down the wave and then prevent the fibrotic steady state from switching to normal steady state. This could be an

explanation to the phenomenon that chronic injury could cause continuous ECM accumulation but liver may regress back to normal if injury is terminated. This is one of the pioneer studies of tissue level modeling. Although the lack of quantitative information and complexity of the system allows us to only take one spatial property, diffusion, into consideration, we have already shown that the spatial information is important for biological systems. With new tools and data available, further models for biological systems may be able to include more and more components and aspects of an organism, and help us understand biological systems, the most complex system, better.

1.3 Overview

The following contents of this thesis are organized in this way:

A single chapter (Chapter 2) introducing background information followed by three chapters (Chapter 3,4 and 5) of three studies at cellular level, cell-population level and tissue level of liver fibrosis. Finally we conclude this thesis in Chapter 6.

2 Chapter 2: Background and Related Work

2.1 Approaches for Modeling Biological Systems

Modeling is one primary task in systems biology. A variety of modeling approaches are applied to model different types of systems, including molecular systems (such as protein structure and molecule-molecule binding) (Kelley and Sternberg, 2009), cellular systems (such as genetic networks, metabolic systems and signaling pathways) (Barabasi and Oltvai, 2004, Weiss et al., 2003), and higher-level systems (such as brain model, virtual liver and model of immune system) (Numminen et al., 2005). As different types of biological systems contain completely different information and require completely different ways of analysis, modeling approach for molecular, cellular and physiological systems have almost no overlaps. Here, we introduce the major approaches for modeling cellular systems as our models were built for cellular systems.

Although there are also subtypes of cellular systems, they share some common. Firstly, the structure of a cellular system is often like a network, consisting of species and their interactions. These species can be small molecules (i.e. in metabolic systems), proteins (i.e. enzymes in metabolic systems and proteins in signaling pathways), or genes (i.e. genetic network). The interactions between two species can be as simple as a chemical reaction or as complex as a multiple-step regulation. Secondly, the network of a cellular system is often dynamic, meaning that the states of species may change as a result of their interactions. The dynamics

of a cellular system can be as abstract as order of interactions (i.e. genetic network) or as detailed as continuous time-evolution of the states of species. The states of species can also have different levels of precisions (a boolean value, a discrete state number, or a value of its concentration). Thus, the main task of modeling cellular systems becomes modeling the structure and dynamics of the system. Because of that, many modeling approaches for cellular systems can be applied to all subtypes of cellular systems (metabolic systems, signaling pathways, genetic networks, etc.) and other approaches can be applied to a subset of all subtypes. These different approaches have their own advantages and disadvantages. Here, we introduce some representative approaches in modeling cellular systems. In addition, we will explain more details about the approach we use in this thesis.

2.1.1 Boolean Network

In Boolean network, species were modeled as Boolean values, which has only two states: ON and OFF. A Boolean network can be defined as a directional graph (Figure 2.1A), in which each node represents a species and each edge represents a regulation process (such as activation and inhibition). In addition, a rule for each node is defined to determine the result of all regulations applied to that node. As species have only two states, a rule can be simply defined by a set of logic gates (Figure 2.1B). A Boolean network can be simulated synchronously (all states are updated in one time step) and asynchronously (one or some states are updated in one time step). The advantage of Boolean network is that it can be used to model large-scale networks, as it requires less information of the states of species. The

disadvantage of it is that the results it can provide have also less information and they are not quantitative.

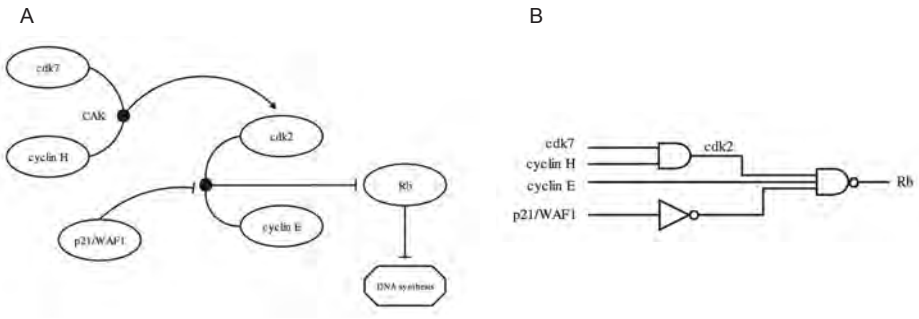

Figure 2.1 A Boolean network example of cell cycle gene regulation (Shmulevich et al., 2002). (A) A diagram of the regulation network showing the species as ellipses and regulations as lines (with arrow head: activation; with flat head: inhibition). The black dots explicitly show the rules applied to cdk2 and Rb. (B) The logic diagram of the network describing the rules applied to cdk2 and Rb.

One of the major applications of Boolean network in biological models is modeling genetic network. The biological basis for this application is that genes often have switch-like behavior, which means the expression of a gene is often turned on and off in its regulations. This switch-like behavior allows us to ignore some quantitative details of the state of a gene, and being qualitative makes modeling of large-scale network possible. With the efforts of Human Genome Project and functional genomics, numerous data for gene regulations are available and most of them are qualitative data. Thus, Boolean network takes advantage of large qualitative dataset and helps us to analyze large-scale genetic networks.

2.1.2 Bayesian Network

Bayesian network is widely used to build statistical models. It is also applied to biological systems to represent and inference the causal relationship among species.

A Bayesian network can be described as a directed acyclic graph (DAG, a graph with no loops). The nodes in the graph represent the species and the edges in the graph represent the relationship/dependencies between species. Each species has no states but a probability of certain state (high/medium/low, on/off) and this probability is dependent on other species. Thus, we have a joint probability distribution (JPD) for all species in a Bayesian network. The relationship/dependencies between species are encoded by a conditional probability table (CPD). Through this CPD, we are able to infer the JPD of all species. Simulation of a classical Bayesian network is a one-step event. Therefore this method simulates static behaviors of the network. Derivatives of Bayesian network such as Dynamic Bayesian Network (DBN) can simulate dynamical changes of probabilities and can have loops in the network model. Bayesian network takes consideration of the uncertainties of biological observations and can be applied for inference of unknown causal relationship between species.

2.1.3 Petri Nets

A Petri net is a directed bipartite graph, in which there are two types of nodes, representing places and transitions (Figure 2.2). Classical Petri nets represent the states of a species as tokens in a place. The number of tokens represents the level of species. A transition connects different places and it can consume and produce tokens. When a transition fires, a token is consumed in any input places of this transition and a token is produced in any output places of this transition. As a result of that, the token moves from one place to another and the states of species change because of firings of transitions. The classical Petri nets are time-free (firing

transitions does not take time), deterministic and discrete (or semi-quantitative). But there are some extensions of Petri nets which make Petri nets more powerful of modeling biological systems. Stochastic Petri Nets (SPN) fires transitions in a stochastic way associating probabilistically distributed firing rates. Continuous Petri Nets (CPN) use continuous values (not tokens) for species states and have a continuous firing rate for each transition. These extensions allow Petri nets to model systems at different abstraction levels and to meet requirements of biological experiments with different accuracies and precisions.

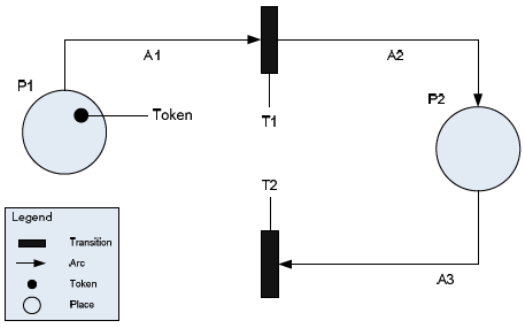

Figure 2.2 A diagram of a Petri net. Circles represent places (P1 and P2). Black rectangles represent transitions (T1 and T2). Black dots represent tokens. Arrows represent the direction for the movement of tokens.

2.1.4 Ordinary Differential Equations (ODEs)

Ordinary Differential Equation (ODE) models describe the time-derivative of the states of species as a function of time and the states (Equation (2.1)). The states in ODEs are continuous values (i.e. concentration of species).

$$\frac{d\boldsymbol{x}}{dt} = F(t,\boldsymbol{x}) \tag{2.1}$$

The biological/biochemical basis of ODE models is the law of mass action. Associating the event of molecule collision and reaction, the law of mass action describes the rate of an elementary reaction (a reaction with a single mechanistic

step) is proportional to the concentrations of reactants. For example, the rate of the reaction $A+B \xrightarrow{k} C$ is $k[A][B]$, in which $[A]$ and $[B]$ represent concentrations of species A and B, and k is a rate constant determined by the natural properties of this reaction (i.e. the affinity of A and B, the pH, the temperature, etc.). As ODE models have strong theoretical basis, ODE is an ideal framework for modeling metabolic systems and signaling pathways, consisting of chemical reactions or biochemical reactions (i.e. enzymatic reactions and protein-protein binding). ODE models are also powerful in analyzing the dynamics of a system since the species concentrations are continuous in time. Another advantage of ODE models is that some reaction rates measured in previous biochemical studies can be directly used in ODE models. Although many rates were measured *in vitro*, they can still be considered as a good approximation of the rates *in vivo*. Sometimes, theoretically ideal methods are not best practically. ODE models have a significant drawback that they often require large amounts of quantitative data. We all know that biological studies often lack quantitative data. In biological studies, it is also difficult to generate large amounts of quantitative data with high accuracy. This makes building ODE models difficult, but with more biological systems studied in detail and more high throughput and quantitative measurements developed, ODE models will become more and more powerful.

In this thesis, we built our models using ODEs because we need to study detailed dynamical behaviors and also some special behavior like bistable behavior. ODE models are the best choices for our purpose of study. We also use a special mathematical form of the ODE models using Kronecker products. This makes not

only the simulation and analysis more efficient, but also the analytical derivations possible. This form of ODEs was used in a toolbox KroneckerBio (Toettcher et al., 2011) and we briefly introduce this formalism in the following section.

2.1.4.1 Formalism of ODE models in KroneckerBio

As biological studies usually focus on mechanistic steps of a process, most known reactions in a signaling pathway are elementary reactions. There are overall four types of elementary reactions shown as below,

$$\begin{cases} \xrightarrow{k_{prod}} A \quad (rate = k_{prod} = \dfrac{d[A]}{dt}) \\ A \xrightarrow{k_{deg}} \quad (rate = k_{deg}[A] = -\dfrac{d[A]}{dt}) \\ A \underset{k_b}{\overset{k_f}{\rightleftharpoons}} B \quad (rate = k_f[A] - k_b[B] = \dfrac{d[A]}{dt} = -\dfrac{d[B]}{dt}) \\ A + B \underset{k_b}{\overset{k_f}{\rightleftharpoons}} C \quad (rate = k_f[A][B] - k_b[C] = \dfrac{d[A]}{dt} = \dfrac{d[B]}{dt} = -\dfrac{d[C]}{dt}) \end{cases} \tag{2.2}$$

According to the law of mass action, all the rates of these reactions can be mathematically represented with zero-order, linear and quadratic form of equations. Therefore, instead of having ODE for each species individually, KroneckerBio express the ODEs as a quadratic system as follow,

$$\frac{d\boldsymbol{x}}{dt} = \boldsymbol{A^1 x} + \boldsymbol{A^2 x} \otimes \boldsymbol{x} + \boldsymbol{k} \tag{2.3}$$

In Equation (2.3), $\boldsymbol{x}$ is a vector of all species concentrations and $\boldsymbol{x} \otimes \boldsymbol{x}$ is the Kronecker product of two $\boldsymbol{x}$ (shown below in Equation (2.4)). $\boldsymbol{A^1}$ and $\boldsymbol{A}^2$ are parametric matrices and $\boldsymbol{k}$ is a parametric vector. $\boldsymbol{A^1}$, $\boldsymbol{A}^2$ and $\boldsymbol{k}$ contains all the rate constants.

$$\boldsymbol{x} = \begin{pmatrix} x_1 \\ x_2 \\ \vdots \\ x_n \end{pmatrix}_{n\times 1} \quad , \quad \boldsymbol{x} \otimes \boldsymbol{x} = \begin{pmatrix} x_1\boldsymbol{x} \\ \vdots \\ x_n\boldsymbol{x} \end{pmatrix} = \begin{pmatrix} x_1x_1 \\ \vdots \\ x_1x_n \\ \vdots \\ x_nx_1 \\ \vdots \\ x_nx_n \end{pmatrix}_{n^2\times 1} \tag{2.4}$$

The benefit of using this mathematical form in Matlab is that stiff ODE solvers in Matlab take advantage of the Jacobian matrix to facilitate the simulation. Many of the biological systems are stiff and this form of ODEs has an explicit form of the Jacobian matrix. In addition, as the connectivity of biological systems is very low, the matrices in both Equation (2.3) and its Jacobian matrix are very sparse. Matlab has algorithms to deal with operations of sparse matrices efficiently.

2.2 Liver Fibrosis and TGF-β Homeostasis

2.2.1 Pathology of Liver Fibrosis

Liver fibrosis is a wound-healing response caused by repeated injury of the hepatic parenchyma (Bataller and Brenner, 2005, Hernandez-Gea and Friedman, 2011). The types of liver injury include ethanol abuse, virus infection, cholestasis, metabolic syndrome etc. Liver injury causes damage of liver parenchyma and a series of inflammatory responses. Both the damaged parenchymal cells and immune cells such as T cell and Kupffer cell can secrete several fibrogenic cytokines, including TGF-β1, PDGF (Platelet-Derived Growth Factor), IL-6 (Interleukin-6) etc. (Bataller and Brenner, 2005). These cytokines can induce the activation of

hepatic stellate cells (HSCs) and other source of myo-fibroblasts. Activated HSCs and myo-fibroblasts are the major source of the excessive extra-cellular matrix (ECM). They can also secrete some cytokines such as TGF-β1 to activate other cells. During liver fibrosis progression, liver parenchyma is often repeatedly injured. The process of injury, inflammation and fibrogenic cell activation described above keeps happening. As a result of the repeated injury, the injured area of parenchyma is replaced by accumulated ECM (Arthur, 1997). In liver fibrosis, not only the quantity, but also the quality of ECM is changed (Eng and Friedman, 2000). In most cases, acute injury is transient and reversible (Benyon and Iredale, 2000). However, when insults are sustained, there will be chronic inflammation as well as scar formation. If the insults are not controlled, liver fibrosis will progress to cirrhosis, an end stage of liver fibrosis and then leading to high mortality. Cirrhosis is not only characterized by large amount of ECM or large area of scar formation, but also a structural change of liver parenchyma and vasculature (Desmet and Roskams, 2004). At late stage of fibrosis or cirrhosis, bridging fibrotic scar is formed and that is called fibrotic septa (Vanheule et al., 2008). The fibrotic septa are where most ECM is accumulated and it may connect portal tracts and central veins (Sherman et al., 1990). Within the septa, there is usually a wide blood vessel called fibrotic shunt (Vollmar et al., 1998). During fibrosis progression, most sinusoids (small blood vessels bypass the liver parenchyma) will become thinner and the fibrotic shunt is where most blood flow through. This kind of distortion of vascular architecture can result in decreased liver function and liver regeneration. It

also leads to the development of portal hypertension, one major pathological phenotype in liver fibrosis.

2.2.2 Cellular Responses in Liver Fibrosis

In liver parenchyma, four major cell types are found: hepatocytes, sinusoidal endothelial cells, hepatic stellate cells (HSCs) and Kupffer cells. Hepatocytes comprise about 65% of liver mass. They are the cells that perform the metabolic function of liver. Sinusoidal endothelial cells form the sinusoid (microvascular structure in liver). These cells have small pores called fenestrae (about 200nm in diameter in normal liver) to allow efficient molecule exchange between hepatocytes and blood. HSCs reside in the space of Disse, the space between the layer of hepatocytes and sinusoidal endothelial cells. In normal liver, HSCs maintain the basal membrane-like matrix in the space of Disse, which is important for the differentiated function of parenchymal cells. Kupffer cells are specialized macrophages in the liver. They locate at the wall of sinusoids and do not circulate in the blood stream.

As we mentioned, liver fibrosis is initiated by liver injury. When liver suffers from injury, parenchymal cells like hepatocytes are damaged by the insults, such as viral infection and toxin. In fibrotic liver, sinusoidal endothelial cells close their fenestrae (defenestration) (Friedman, 2003). This can lead to changes of molecule exchange between parenchymal cells and blood, and also changes of local blood pressure. HSCs are in their quiescent state in normal liver and their secretion of ECM is limited. During fibrosis progression, HSCs become myo-fibroblast-like (activated state) and express excessive ECM (Friedman, 2000, Gressner and

Weiskirchen, 2006). Activated HSCs are also proliferative. Activation of HSCs is the major cause of excessive ECM and scar formation in liver fibrosis (other types of myo-fibroblasts in liver were also found such as, portal fibroblasts, bone marrow-derived cells and cells from EMT) (Hernandez-Gea and Friedman, 2011). The earliest activation of HSCs is associated with inflammation and paracrine stimulation by their neighboring cells, including damaged hepatocytes, injured bile duct cells and Kupffer cells (Iredale, 2007). Kupffer cells can stimulate HSC activation by secretion of cytokines such as TGF-β1 (Transforming Growth Factor-β1, an isoform of TGF-β) and PDGF (Platelet-Derived Growth Factor) (Iredale, 2007).

2.2.3 TGF-β Activation in Liver Fibrosis

Many cytokines are involved in liver fibrosis. Liver fibrosis is accompanied by repeated or chronic liver injury. The earliest response after injury is inflammation. Therefore, in liver fibrosis, inflammatory cytokines such as IL-6 (Interleukin-6), IFN-γ (Interferon-γ), TNF-α (Tumor Necrosis Factor-α) are secreted from Kupffer cells, hepatocytes as well as some immune cells in the blood (Friedman, 2000). These inflammatory cytokines can initiate the activation of myo-fibroblasts (mainly HSCs). After the inflammatory phase of fibrosis, there will be a fibrogenic phase when the activated myo-fibroblasts/HSCs reconstruct the ECM. Growth factors such as TGF-β1 and PDGF play important roles not only in the inflammatory but also the fibrogenic phase of liver fibrosis. TGF-β1 is a key cytokine that induces the activation of HSCs and other types of myo-fibroblasts in liver (i.e. portal fibroblasts and EMT of hepatocytes) (Zeisberg et al., 2007). Initial HSC activation is

stimulated by TGF-β1 via paracrine signals from Kupffer cells and injured hepatocytes. After HSCs are activated, there is an autocrine signal of TGF-β1 to maintain the activation states of HSCs (Gressner and Weiskirchen, 2006, Gressner et al., 2002). Activated HSCs are also proliferative. This is mainly due to the stimulation of PDGF (Kinnman et al., 2001). Proliferation of HSCs is also initiated by paracrine signal of PDGF and maintained by autocrine signal of PDGF (Bataller and Brenner, 2005).

TGF-β1 plays crucial role in liver fibrosis as it initiates and maintains the activation of HSCs, the major fibrogenic cells in liver fibrosis. Therefore, many studies have focused on TGF-β1 related signaling and tried to discover drug targets for liver fibrosis therapies (Salgado et al., 2000, Currier et al., 2003, Kondou et al., 2003). TGF-β1 binds to specific receptors on the cell surface and activates the Smad signaling cascade to regulate gene expression (Wrana and Attisano, 2000). Moreover, TGF-β1 is secreted in its latent form and needs to be activated so it can stimulate Smad downstream signaling (Annes et al., 2003). Thus, not only the downstream Smad signaling, but also the upstream activation of TGF-β1 is important for TGF-β1 regulations. Latent TGF-β1 is a protein complex in which TGF-β1 dimer binds to a latency-associated peptide (LAP) and LAP further associates with the latent-TGF-β1 binding protein (LTBP) (Annes et al., 2003). There are several ways that TGF-β1 can be released from LAP and become active, including high temperature, low pH, ROS, integrin, proteases (such as plasmin) (Lyons et al., 1990, Dallas et al., 2002), and thrombospondin-1 (TSP1) (Murphy-Ullrich and Poczatek, 2000, Daniel et al., 2004, Schultz-Cherry et al., 1994). Among

these activation conditions or activators, plasmin and TSP1 is highly related to hepatocytes and HSCs, respectively. In addition, plasmin is regulated by TGF-β1 signaling and TSP1 is a part of TGF-β1 autocrine of HSCs.

2.2.4 The Network of TGF-β Activation in the ECM

Previous work has studied a network of TGF-β activation including two activators, plasmin and TSP1; interplay between these two activators; and two feedback loops that active TGF-β regulates plasmin and TSP1 (Venkatraman et al., 2012). Figure 2.3 shows the major players in the network. As we mentioned earlier, plasmin and TSP1 could both activate TGF-β from its latent form. These two activators of TGF-β have a mutual antagonism that plasmin could cleave TSP1 slowly (Anonick et al., 1993) and TSP1 could inhibit plasmin by tight binding to its activation site (Anonick et al., 1993, Hogg et al., 1992). More interestingly, TGF-β could regulate plasmin by inducing the production of plasminogen activator inhibitor type 1 (PAI1) (Kutz et al., 2006) and PAI1 inhibits the urokinase pathway for plasmin activation (Vassalli et al., 1991, Venkatraman et al., 2010). TGF-β could also regulate TSP1 by inducing HSC activation.

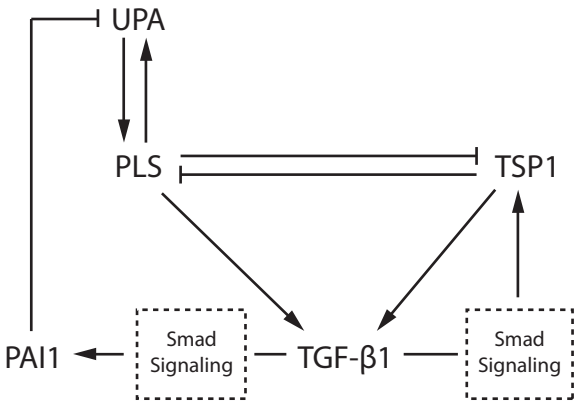

Figure 2.3 Upstream network of TGF-β activation (Venkatraman et al., 2012). Plasmin (PLS) and Thrombospondin-1 (TSP1) can both activate TGF-β. They also have mutual antagonism. Plasmin is activated from plasminogen through a positive feedback regulation of urokinase-typed plasminogen activator (UPA). TGF-β regulates plasmin activation by inducing the production of PAI1 through Smad signaling pathway. It also regulates TSP1 production through Smad signaling and hepatic stellate cell (HSC) activation. The Smad signaling pathway was modeled as a black box in (Venkatraman et al., 2012).

As shown in Figure 2.3, Smad signaling pathway was modeled as black box in (Venkatraman et al., 2012). We then initiate our series of studies from a systematic analysis of Smad signaling pathway.

3 Chapter 3: Systematic Analysis of Negative Regulatory Mechanisms in TGF-β Signaling Pathway

3.1 Introduction

Transforming Growth Factor-β (TGF-β) regulates cell migration and cell fate and TGF-β signaling is a target of pharmaceutical research (Yingling et al., 2004) for treatment of metastatic cancer and fibrotic diseases. Signal transduction from extracellular TGF-β to the cell nucleus through the Smad pathway is well documented (Massague, 1998, Shi and Massague, 2003, Attisano and Wrana, 2002, Bassing et al., 1994, Schmierer and Hill, 2005, Massague and Wotton, 2000). The TGF-β ligand binds sequentially to two heterogeneous receptors (TGF-β receptor type II and type I) on the cell membrane to form a ligand-receptor complex (Massague, 1998). The type II receptor is a constitutively active kinase, recruited by TGF-β to the type I receptor (Bassing et al., 1994). The type I receptor is activated by the type II receptor and then phosphorylates the R-Smads (Smad2 and Smad3) at two C-terminal serine residues. Upon phosphorylation, R-Smads form a homomeric complex or a heteromeric complex with Co-Smad (Smad4) (Shi and Massague, 2003, Schmierer and Hill, 2005). The key outcome of the Smad cascade is accumulation of phosphorylated R-smad (phospho-R-Smad) in the nucleus, causing widespread effects on gene regulation (Massague et al., 2000, Massague and Wotton, 2000).

Recent work by Zi *et al.* showed that cells respond differently to phospho-R-smad, depending on the temporal dynamics of Smad signaling (Zi et al., 2011). They found that early (45min) phospho-R-Smad levels, and early gene expression, had a gradual, graded dependence on the dose of TGF-β. In contrast, later (24hr) phospho-R-Smad levels controlled a distinct set of genes with ultrasensitive, sigmoidal dependence on the dose of TGF-β. These functional effects demonstrate the importance of understanding the dynamics of the Smad system.

Smad signaling is known to decrease spontaneously after TGF-β stimulation (Figure 3.1A), and this self-limiting behavior is a major determinant of Smad dynamics. Self-limiting behavior may arise from ligand-induced receptor inhibition (Afrakhte et al., 1998, Itoh et al., 1998, Ebisawa et al., 2001, Hayashi et al., 1997, Kavsak et al., 2000, Zhang et al., 2012, Eichhorn et al., 2012), phospho-R-Smad dephosphorylation (Lin et al., 2006), phospho-R-Smad degradation (Lo and Massague, 1999, Lin et al., 2000, Alarcon et al., 2009, Inui et al., 2011, Aggarwal and Massague, 2012), or other mechanisms. Extensive experimental evidence documents multiple individual mechanisms, but the relative roles and combined effects are not well understood. Dynamic measurements (time-series immuno-blots) are available from many previous studies, and this wealth of information provides an opportunity for systems-level modeling to integrate information about dynamics and to integrate mechanisms of negative regulation, toward a better understanding of the Smad system behavior.

Previous computational models of TGF-β/Smad signaling have contributed important biological insights, but they have only simulated some selected

mechanisms of negative regulation. Villar *et al.* built a model of TGF-β receptor trafficking dynamics, including ligand-induced receptor degradation, which was able to simulate some key dynamic effects such as the peak and decay of phospho-R-Smad levels (Vilar et al., 2006). Models by Klipp and co-workers extended the work of Villar *et al.* to include Smad phosphorylation and nuclear translocation (Klipp and Zi, 2007), and to include transient versus sustained Smad signaling (Zi et al., 2011), but these models simplified the negative regulation processes, giving a strong role to receptor degradation. The model by Schmierer *et al.* provided important insights into the short-term dynamics of Smad nucleo-cytoplasmic shuttling (Schmierer et al., 2008), but the only mechanism of negative regulation in this model was dephosphorylation. Other modeling studies have focused on robustness and *in silico* perturbation analysis (Melke et al., 2006, Chung et al., 2009). Mathematical models have yielded important insights, but they have not represented TGF-β/Smad negative regulation with enough detail for analyzing the contributions of different mechanisms, nor for evaluating alternative hypotheses.

In this work, we develop a series of computational models representing individual and combinations of mechanisms of R-Smad negative regulation. Comparisons between models and existing datasets first reveals negative regulations on two different time scales. Based on the time scale, we classified negative regulatory mechansims into fast- and slow- mode mechanisms. Our modeling also shows that at least one fast-mode and one slow-mode mechanisms is required for a model to fit phospho-R-Smad dynamics after short- and long-exposure to TGF-β. R-Smad Dephosphorylation has been shown to have fast and strong negative

regulation effect in the literature and is confirmed in our analysis to be a fast-mode mechanism. Although Receptor Degradation and P-R-Smad Degradation are shown to be slow-mode mechanisms in our analysis, they are falsified by our modeling and experiments. Thus, current understanding of slow-mode negative regulation in TGF-β remains unclear, and we seek to find a slow-mode mechanism which could explain phospho-R-Smad dynamics.

One of our key findings is a novel negative feedback effect, in which the phosphatase PPM1A is rapidly upregulated after TGF-β stimulation, in conjunction with declining levels of phospho-R-Smad. We further explore possible mechanisms of PPM1A upregulation via theoretical models of PPM1A sequestration. Another contribution of our work is an explanation for a previous controversy about R-Smad degradation (Lin et al., 2006, Lo and Massague, 1999, Lin et al., 2000, Alarcon et al., 2009).

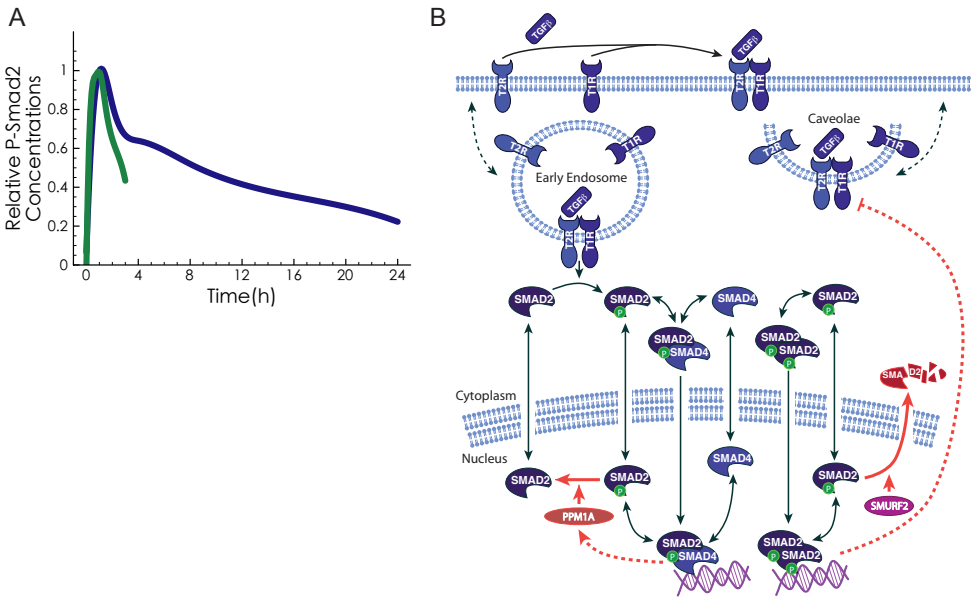

Figure 3.1 The Smad signaling pathway. (A) P-Smad2 dynamics from literature. Curves show the quantified western blot measurements of P-Smad2 from Lin *et al.* (Lin et al., 2006) (blue) and Massague *et al.* (Lo and Massague, 1999) (green) after TGF-β stimulation. (B) Pathway diagram of Smad signaling (using template from BioCarta). The dashed arrows indicate those reactions which are modeled in black box. The red arrows indicate the negative regulatory mechanisms: (1) PPM1A dephosphorylating phospho-R-Smad; (2) Smurf2 induced proteasome degradation of phospho-R-Smad; (3) I-Smad induced receptor inhibition; (4) PPM1A upregulation by Smad signaling.

3.2 Materials and Methods

3.2.1 Model Specifications

3.2.1.1 Model Structure

The reactions in our TGF-β signaling pathway model can be grouped into three sections: trafficking, Smad nucleocytoplasmic shuttling, and negative regulatory mechanisms. Our assumptions of the receptor trafficking followed those in (Klipp and Zi, 2007). For Smad nucleocytoplasmic shuttling, we followed (Schmierer et al., 2008). The only difference in Smad nucleocytoplasmic shuttling between (Klipp and Zi, 2007) and (Schmierer et al., 2008) is that in (Schmierer et al., 2008), R-Smads can form a homogeneric complex. It has been shown that R-Smads can form complex with themsevles (Clarke et al., 2009). Although the stoichiometry is not clear, we follow the simplest assumption in (Schmierer et al., 2008) that R-Smads can form homogeneric and heterogeneric complexes at the same rate. For the negative regulatory mechanisms, we tested many possibilities based on literature findings and also our hypotheses (such as PPM1A upregulation). Different mechansims are listed in Table 3.1. Here we describe each of them in details. All species names are listed in Table 8.1. All rate constants are listed in Table 8.2.

1) R-Smad Dephosphorylation was modeled as a single reaction in which nuclear phospho-R-Smad was dephosphorylated to R-Smad. The rate of dephosphorylation was proportional to the concentration of phospho-R-Smad (Reaction 33, Table 8.3).

2) Receptor Degradation was modeled according to (Klipp and Zi, 2007) as a black box in which the degradation rate of the ligand-receptor complex was proportional to the concentration of the Smad complex in the nucleus (Reaction 31-32, Table 8.3).

3) P-R-Smad Degradation was modeled as a single reaction in which nuclear phospho-R-Smad was degraded at a rate proportional to its concentration (Reaction 34, Table 8.3), assuming that Smurf2 would be unchanged in TGF-β signaling.

4) Endogenous Synthesis and Degradation of R-Smad was modeled by incorporating (a) constant production of cytoplasmic R-Smad (Reaction 35, Table 8.3) and (b) degradation of total R-Smad, proportional to the total R-Smad concentration (Reaction 35-39, Table 8.3), but independent of Smurf2-induced degradation.

5) Receptor Inhibition was modeled such that I-Smad could induce degradation, inhibition, and dephosphorylation of the ligand-receptor complex. Firstly, I-Smad (Smad7) was produced at a rate proportional to the concentration of Smad complex in the nucleus (Reaction 40-41, Table 8.3) and had a turnover rate proportional to its concentration (Reaction 42, Table 8.3). Then I-Smad could either associate with ligand receptor

complex (LRC) in the caveolae (LRC_{Cave}, Reaction 44, Table 8.3) or could associate with LRC in the early endosome (LRC_{EE}, Reaction 45, Table 8.3). After association of the LRC with I-Smad, the complex could either be dephosphorylated (Reaction 46-47, Table 8.3) or degraded (Reaction 48-49, Table 8.3).

6) PPM1A Upregulation assumed that the Smad complex in the nucleus was responsible for inducing PPM1A production. That is, the rate of induced production was proportional to the concentraion of Smad complex in the nucleus (Reaction 56-57, Table 8.3). To simulate basal (unstimulated) levels, PPM1A was also synthesized at a constant rate (Reaction 52, Table 8.3). All sources of PPM1A, unless bound, were degraded endogenously at a rate proportional to PPM1A concentration (Reaction 52, Table 8.3). Another assumption concerns the kinetics of PPM1A activity. Prior models with constant PPM1A levels used a one-step approximation for the kinetics of the dephosphorylation of phospho-R-Smad by PPM1A, but the models with explicit regulation of PPM1A employed a two-step model of catalysis (Reaction 58-61, Table 8.3) with reversible association/dissociation followed by irreversible catalysis.

7) PPM1A Stabilization assumed that PTEN could associate with phospho-R-Smad (Reaction 66, Table 8.3) and this binary complex could further associate with PPM1A to form a ternary complex pSmad:PTEN:PPM1A (Reaction 67, Table 8.3). The ternary complex could dissociate in the manner it was formed, or could alternatively release the phospho-R-Smad

alone and the PTEN-PPM1A as a binary complex (Reaction 68, Table 8.3). The PTEN-PPM1A complex was assumed to evade degradation while the unbound PPM1A would degrade (Reaction 53-54, Table 8.3). PPM1A was synthesized in the cytoplasm (Reaction 53, Table 8.3) and was imported into the nucleus at a high rate (Reaction 55, Table 8.3) so that PPM1A was predominantly in the nucleus. When PTEN bound to PPM1A, PPM1A phosphatase activity was assumed to be unchanged (Reaction 62-65, Table 8.3). We allowed the rate of PTEN-PPM1A imported into the nucleus to differ from the rate of import for unbound PPM1A, and the actual rates were estimated numerically (Reaction 71, Table 8.3). PTEN in the nucleus could be exported back into the cytoplasm (Reaction 72, Table 8.3).

3.2.1.2 Model Parameters

3.2.1.2.1 Rate Constants

The list of rate constants is shown in Table 8.2. We have retained the values of the experimentally derived parameters cited by (Klipp and Zi, 2007). We have also retained previous rates for the type I and the type II receptors and the recycling rate of the ligand-receptor complex in the caveolae, which had been strongly constrained by qualitative information. For the other rate constants that were estimated by (Klipp and Zi, 2007), we have re-estimated these parameters again in the context of our model. In particular, the rate constants for Smad

nucleocytoplasmic shuttling were modified to fit our model calibration and the new findings in (Schmierer et al., 2008). First of all, the concentrations of species in the nucleus are represented as their relative concentrations in the cytoplasm. For example, if the absolute concentration of Smad2 in the nucleus is $[Smad2_{nuc}]^{abs}$, we use the relative concentration $[Smad2_{nuc}]^{rel} = [Smad2_{nuc}]^{abs} \cdot (V_{nuc} / V_{cyt})$ instead of $[Smad2_{nuc}]^{abs}$ in our model to simulate the concentrations in two compartments. For example, the ODEs of Smad2 using absolute concentrations are:

$$\frac{d[Smad2_{cyt}]}{dt} = -kimp_{Smad2}[Smad2_{cyt}] + kexp_{Smad2}[Smad2_{nuc}]^{abs} \cdot \frac{V_{nuc}}{V_{cyt}} - kf_{Smad2}[Smad2_{cyt}][LRC_{EE}]$$

$$\frac{d[Smad2_{nuc}]^{abs}}{dt} = kimp_{Smad2}[Smad2_{cyt}] \cdot \frac{V_{cyt}}{V_{nuc}} - kexp_{Smad2}[Smad2_{nuc}]^{abs} + kdeph_{pSmad2}[pSmad2_{nuc}]^{abs}$$

After substituting $[Smad2_{nuc}]^{abs}$ with $[Smad2_{nuc}]^{rel} \cdot (V_{cyt} / V_{nuc})$:

$$\frac{d[Smad2_{cyt}]}{dt} = -kimp_{Smad2}[Smad2_{cyt}] + kexp_{Smad2}[Smad2_{nuc}]^{rel} - kf_{Smad2}[Smad2_{cyt}][LRC_{EE}]$$

$$\frac{d[Smad2_{nuc}]^{rel}}{dt} = kimp_{Smad2}[Smad2_{cyt}] - kexp_{Smad2}[Smad2_{nuc}]^{rel} + kdeph^{rel}_{pSmad2}[pSmad2_{nuc}]^{rel}$$

where

$$kdeph^{rel}_{pSmad2} = kdeph_{pSmad2} \cdot \frac{V_{cyt}}{V_{nuc}} = 3 \cdot kdeph_{pSmad2}$$

The export rates computed in (Schmierer and Hill, 2005) are identical to our $kexp_{Smad2}$ and $kexp_{Smad4}$. However, the import in (Schmierer and Hill, 2005) are actually $kimp'_{Smad2} = kimp_{Smad2} \cdot (V_{cyt} / V_{nuc})$ and $kimp'_{Smad4} = kimp_{Smad4} \cdot (V_{cyt} / V_{nuc})$. So our import rates are $kimp_{Smad2} = kimp'_{Smad2} \cdot (V_{nuc} / V_{cyt}) = 0.0027 / 3 = 0.0009 s^{-1} = 0.054 \min^{-1}$ and

$kimp_{Smad4} = kimp'_{Smad4} \cdot (V_{nuc} / V_{cyt}) = 0.0027 / 3 = 0.0009 s^{-1} = 0.054 \min^{-1}$. Note that the rates of the reactions in the nucleus (e.g. $kdeph_{pSmad2}$) are substituted because the concentrations of the reactants are relative. But all these rates are estimated so we do not need to substitute any values of them.

Secondly, it was found that the import rate of Smads complex is higher than the monomeric Smad2 (Schmierer et al., 2008). Therefore, we set the import and export rate of Smads complex according to (Schmierer et al., 2008).

3.2.1.2.2 Initial Concentrations

The initial concentrations of all species were set to their equilibrium points in unstimulated cells. The initial concentrations of the receptors followed those in (Klipp and Zi, 2007), as the rate constants for receptor trafficking were kept the same as those in (Klipp and Zi, 2007). For Smad2 and Smad4, we can derive their equilibrium concentrations based on their shuttling rates and total amount. At steady state,

$$\begin{cases} \dfrac{[Smad2_{cyt}]}{[Smad2_{nuc}]^{rel}} = \dfrac{kexp_{Smad2}}{kimp_{Smad2}} = \dfrac{0.348 min^{-1}}{0.054 min^{-1}} = 6.444 \\ [Smad2_{cyt}] + [Smad2_{nuc}]^{rel} = [Smad2_{total}]^{rel} \end{cases}$$

$$\begin{cases} \dfrac{[Smad4_{cyt}]}{[Smad4_{nuc}]^{rel}} = \dfrac{kexp_{Smad2}}{kimp_{Smad2}} = \dfrac{0.054 min^{-1}}{0.054 min^{-1}} = 1.000 \\ [Smad4_{cyt}] + [Smad4_{nuc}]^{rel} = [Smad4_{total}]^{rel} \end{cases}$$

The relative concentrations of total Smad2 and total Smad4 in HaCaT cells are 571.43nM and 1333.33nM (Zi et al., 2011, Klipp and Zi, 2007). We then calculated

the steady state concentrations in unstimulated cells as the initial concentrations showing in Table 8.1.

3.2.1.3 Model Simulation and Parameter Estimation

The model simulation and parameter estimation were performed using KroneckerBio toolbox in Matlab. The KroneckerBio toolbox basically calls the ode15s function in Matlab to solve the system of ODE equations and the fmincon function in Matlab to estimate parameters. Multiple initial guesses were generated randomly in order to achieve a more global optimum in parameter estimations. Sum of squared errors were used as the objective function to optimize the model to experimental data.

The parameters from literature were validated by simulating the exact published models. Our parameter estimation method was also applied to published models and the modeling fitting results were highly similar to that in the literature.

The parameters related to each mechanism are listed in Table 8.4. The parameters of the best-fit of each model are listed Table 8.5.

3.2.2 Biological Essays

3.2.2.1 HaCaT cell culture and TGF-β treatment

HaCaT cells (from Cell Lines Service) were cultured following the protocol provided by the manufacturer. DMEM culture medium with 10% FBS was used to culture the cells. DMEM culture medium without FBS was used during treatment of TGF-β as the serum contains TGF-β.

3.2.2.2 ELISA for phosphorylated Smad2 and total Smad2

ELISA kits (from Cell Signaling) were used to quantify phosphorylated Smad2 and total Smad2. Whole cell lysates were collected using attached cell lysis buffer and following the cell lysis protocol in the kits. Sample dilutions for phosphorylated Smad2 and total Smad2 are 1 time and 100 times respectively. Serial dilutions of one sample were measured to check the linear range of the readouts.

3.2.2.3 Western blot for total type I receptor and PPM1A

Whole cell lysates were collected using RIPA buffer from HaCaT cells for western blots. Antibodies against the type I receptor (Santa Cruz) and PPM1A (Abcam) were used following manufacturers' instructions. Primary antibody dilutions of 1:7500 and 1:250 were used for the type I receptor and PPM1A respectively. The quantification of the band intensities was preformed using ImageJ.

3.3 Results

We constructed a series of computational models (Table 3.1) examining negative regulatory mechanisms in TGF-β/Smad signaling. All models share a common skeleton (Figure 3.1B) of Smad signaling, including TGF-β receptor trafficking and Smad nucleo-cytoplasmic shuttling, based on previous models (Vilar et al., 2006, Klipp and Zi, 2007, Schmierer et al., 2008). Molecular interactions were modeled using ordinary differential equations (ODEs) for mass action kinetics, and the system of ODEs was simulated using KroneckerBio (Toettcher et al., 2011) in Matlab (Mathworks, Natick, MA). Model specifications, parameter estimation, and other computational methods are specified in Section 3.2 Materials and

Methods. The HaCaT cell line was used in the biological assays. Experimental methods are also specified in Section 3.2 Materials and Methods.

3.3.1 Modeling the Negative Regulatory Mechanisms

Negative regulatory mechanisms were simulated to obtain the dynamics of their effects and to estimate their potential contributions to the down-regulation of phospho-R-Smad (0.5-24hr). The negative regulatory mechanisms, illustrated in Figure 3.1B, include three previously published mechanisms and a fourth hypothesized mechanism that we developed during the analysis of the models. The focus of our initial modeling was the three previously reported mechanisms of negative regulation:

(1) **Receptor Inhibition**. Smad complexes can induce the production of I-Smad (Smad7) (Afrakhte et al., 1998, Itoh et al., 1998). There are three ways I-Smad can inhibit the ligand-receptor complex: (1a) It can block the activation site of the receptor kinase; (1b) I-Smad can recruit E3-ligases to target the ligand-receptor complex for degradation (**Receptor Degradation**) (Kavsak et al., 2000); and (1c) I-Smad can recruit PP1c to dephosphorylate the type I receptor kinase (Shi et al., 2004). We modeled the expression of I-Smad as a black box in which the rate of I-Smad production was proportional to the concentration of the Smad complex in the nucleus. Mechanism (1b) of I-Smad action (Receptor Degradation) was simulated in models 2, 3, and 5. All types of "receptor inhibition," (1a), (1b), and (1c), were simulated in model 8.

(2) **P-R-Smad Degradation**. R-Smad can be phosphorylated at its tail region or its linker region. We use the term phospho-R-Smad to refer to tail region phosphorylation, which is more important for gene regulatory function (Alarcon et al., 2009). Phosphorylation of nuclear R-Smad at its linker region causes Smurf2 to target R-Smad for proteasome-dependent degradation (Alarcon et al., 2009). Assuming Smurf2 concentration to be constant, and assuming linker-region phosphorylation to be proportional to tail-region phosphorylation (Alarcon et al., 2009), we simulate the rate of R-Smad degradation to be proportional to the concentration of nuclear R-Smad.

(3) **R-Smad Dephosphorylation**. Phospho-R-Smad in the nucleus is dephosphorylated specifically by PPM1A, a member of the PP2c family (Lin et al., 2006). The rate of dephosphorylation is modeled to be proportional to the concentration of phospho-R-Smad in the nucleus.

Table 3.1 Models with different negative regulatory mechanisms and the name of each mechanism. Each row represents one model. The + sign indicates that a mechanism is included in a model, and - indicates a mechanism NOT included.

Model	1	2	3	4	5	6	7	8	9	10	11
R-Smad Dephosphorylation	+	+	-	-	+	+	+	+	+	+	+
Receptor Degradation	-	+	+	-	+	-	-	-	-	-	-
P-R-Smad Degradation	-	-	-	+	+	+	+	-	-	-	+
Endogenous Synthesis and Degrdation of R-Smad	-	-	-	-	-	-	+	-	-	-	+
Receptor Inhibition	-	-	-	-	-	-	-	+	-	-	-
PPM1A Upregulation by Expression	-	-	-	-	-	-	-	-	+	-	-
PPM1A Stablization	-	-	-	-	-	-	-	-	-	+	+

3.3.2 Negative Regulation Occurs at Multiple Time Scales

R-Smad dynamics depend on the duration of TGF-β stimulation. When TGF-β is administered in excess (2ng/ml) (Bakin et al., 2000, Goumans et al., 2002) for 24hrs, phospho-R-Smad peaks at about 1hr and then decays for 24hrs (Lin et al., 2006). When TGF-β is administered for 30min and then removed (by washing following by receptor inhibition with the compound SB-431542), phospho-R-Smad is eliminated within 4hrs (Lin et al., 2006, Schmierer et al., 2008). Both short-exposure and long-exposure TGF-β treatment datasets (Figure 3.2) were utilized when building the models of negative regulation (Table 3.1, Table 8.4).

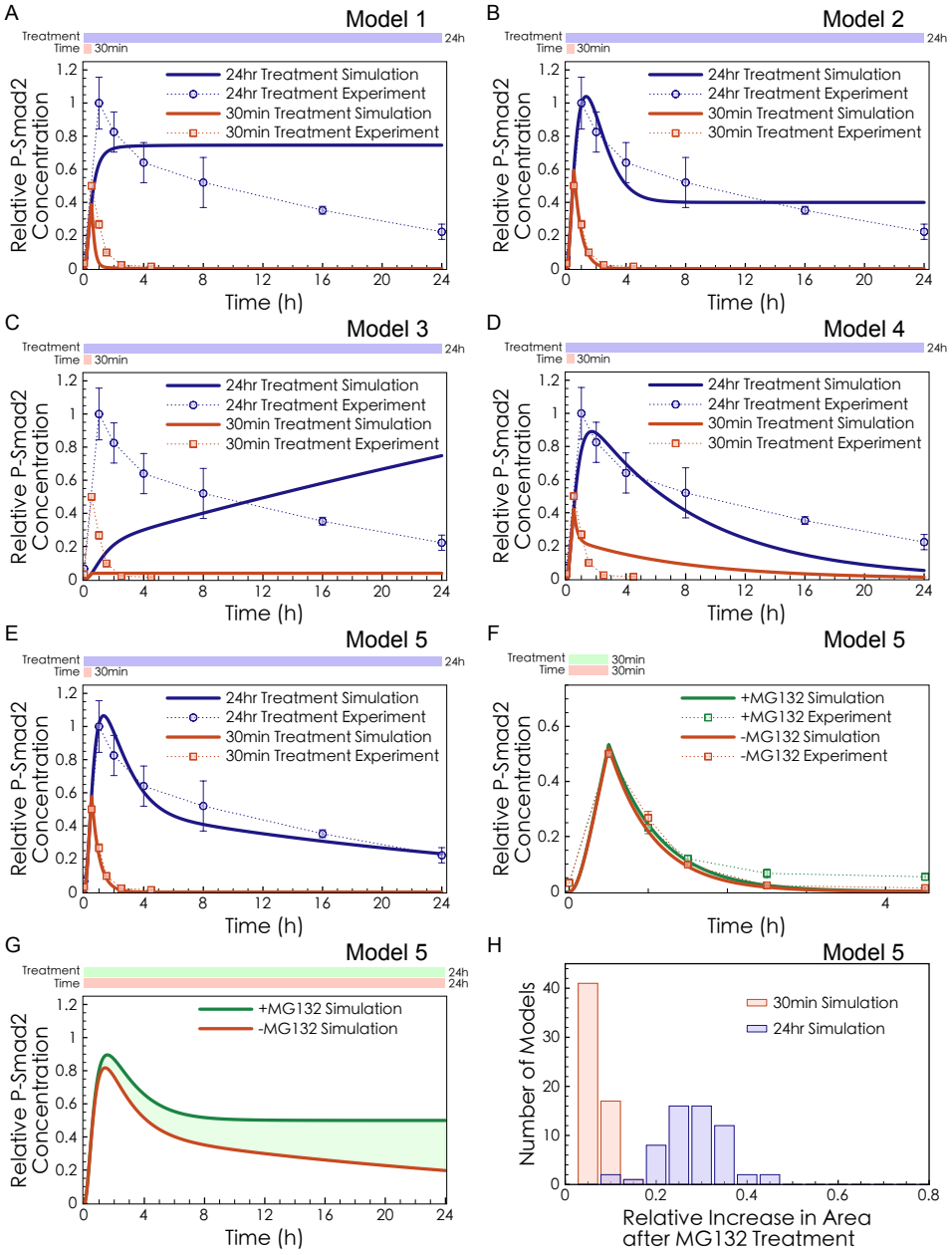
A
Model 1
Treatment
Time
30min
24h
24hr Treatment Simulation
24hr Treatment Experiment
30min Treatment Simulation
30min Treatment Experiment
Relative P-Smad2 Concentration
Time (h)
B
Model 2
C
Model 3
D
Model 4
E
Model 5
F
Model 5
+MG132 Simulation
+MG132 Experiment
-MG132 Simulation
-MG132 Experiment
G
Model 5
H
Model 5
30min Simulation
24hr Simulation
Number of Models
Relative Increase in Area after MG132 Treatment

Figure 3.2 Model fitting results with different combinations of known negative regulatory mechanisms. (A-E) Phospho-R-Smad simulations were fitted to long-exposure and short-exposure P-Smad2 experimental data from Lin *et al.* (Lin et al., 2006). In the long-exposure experiment, HaCaT cells were treated with TGF-β for 24hr (blue dots). In the short-exposure experiment, HaCaT cells were treated with TGF-β for 30min, then TGF-β was washed out and SB-431542 was added to inhibit the receptors (red dots). All P-Smad2 measurements used total cell lysate. The model simulations (solid red and blue curves) were fitted to the two sets of data simultaneously. Negative regulatory mechanisms in each model are as follows: (A) Model 1: R-Smad Dephosphorylation; (B) Model 2: R-Smad Dephosphorylation and Receptor Degradation; (C) Model 3: Receptor Degradation; (D) Model 4: P-R-Smad Degradation; (E) Model 5: R-Smad Dephosphorylation, Receptor Degradation and P-R-Smad Degradation. The reactions of each model are listed in the Supporting Information. (F-H) Predictions of the best-fit model (Model 5) in MG132 pre-treated cells. Simulation of MG132 treatment was performed by turning off the Smurf2-induced P-R-Smad Degradation (setting $kdeg_{pSmad2}=0$) in Model 5. (F) Comparison of the model prediction and experimental data from Lin *et al.* (Lin et al., 2006) in the short-exposure experiment. (G) Model prediction in the long-exposure experiment. The green shaded area shows the cumulative difference between +MG132 and -MG132. (H) A variety of models were fitted to the short-exposure and long-exposure experiments, and the cumulative difference in phospho-R-Smad2 between +MG132 and -MG132 was computed for each case. A histogram plots the cumulative differences seen in the short-exposure experiment (red) and the long-exposure experiment (blue).

Our first simulations studied the kinetics of three previously modeled mechanisms. The three mechanisms have conceptual similarities, but we were curious whether they would have different kinetic implications for the system. Multiple models, with different combinations of these mechanisms, were fitted to the long-exposure and short-exposure datasets described above.

Model 1, with R-Smad Dephosphorylation**,** was able to recapitulate the short-exposure TGF-β treatment experiment, as dephosphorylation is a fast process. This dephosphorylation model could turn off the signal once the stimulus was cut off (Figure 3.2A red curve), but it reached a steady state at about 1hr and was not able to recapitulate the extended 24hr decline of phospho-R-Smad in long-exposure TGF-β treatment (Figure 3.2A blue curve). Thus we describe R-Smad Dephosphorylation as a "fast-mode" mechanism. To explain the decline during long-exposure experiments, a complementary "slow-mode" might be provided by cumulative processes such as degradation effects. Model 2 combines Receptor Degradation and R-Smad Dephosphorylation. It succeeded in recapitulating the short-exposure TGF-β treatment very well, and it had moderately good agreement with the long-exposure dataset (Figure 3.2B). As a control, we modeled Receptor Degradation alone (Model 3), but it could not provide an early decline in the short-exposure experiment (Figure 3.2C). Thus, Receptor Degradation serves as a slow-mode mechanism as it was able to explain the gradual decline of phospho-R-Smad in the long-exposure experiment but not the steep deline of phospho-R-Smad in the short-exposure experiment. A model with P-R-Smad Degradation alone (Model 4) achieved significant negative regulation for the long-exposure case (Figure 3.2D),

because P-R-Smad Degradation would persist for many hours. However, fitted Model 4 had difficulty explaining both the short-exposure and long-exposure datasets simultaneously, in keeping with previous experimental evidence, showing that P-R-Smad Degradation is not responsible for fast-mode effects in short-exposure conditions (Lin et al., 2006). No single mechanism of negative regulation was able to explain pSmad2 behavior. We infer that the experimentally observed levels of phospho-R-Smad arise from a combination of fast-mode and slow-mode mechanisms (or from higher-order combinations of effects).

Many models have omitted P-R-Smad Degradation from simulations (Vilar et al., 2006, Klipp and Zi, 2007, Schmierer et al., 2008, Zi et al., 2011), perhaps because this mechanism was found to be insignificant in the experiments of Lin *et al.* (Lin et al., 2006). Noting that the Lin experiments used short-exposure conditions, we ask whether P-R-Smad Degradation, a slow-mode mechanism, might have greater significance during the negative regulation induced by long-exposure treatments. Model 5 incorporated R-Smad Dephosphorylation, Receptor Degradation, and P-R-Smad Degradation (Figure 3.2E). P-R-Smad Degradation was significant in this model (Figure 3.2F-H) when its effects were measured after more than 1hr of TGF-β treatment. As yet, we have no basis for knowing which type of slow-mode degradation would be most important in R-Smad signaling.

3.3.3 New Experimental Data Supports P-R-Smad Degradation Rather Than Receptor Degradation

We next tried to assess the relative impact of two slow-mode mechanisms, Receptor Degradation and P-R-Smad Degradation, on the dynamics of phospho-R-Smad in long-exposure TGF-β treatment. The rate constant for Receptor Degradation and the rate constant for P-R-Smad Degradation were varied *in silico* (Figure 3.3A), showing that many ratios were equally good at fitting the observed dynamics. Several of the successful models exhibited a strong decline in T1R, the type I receptor (Figure 3.3B). Moreover, the degree of T1R decline is correlated with the rate of Receptor Degradation and the rate of P-R-Smad Degradation (Figure 3.3C). Thus, to quantify the relative contribution of Receptor Degradation and P-R-Smad Degradation in HaCaT cells, we measured T1R experimentally at 9 time points (from 15min to 24hr) after TGF-β stimulation (with n=3 replications and significance determined by student t-test). Surprisingly, there was no significant loss of T1R in experiments (Figure 3.3D-E), even at late time points, indicating that Receptor Degradation is very weak in HaCaT cells (phospho-R-Smad time series concentrations were measured as positive control, Figure 3.3C). A weak role for Receptor Degradation has also been suggested by the experimental work of Clarke et al. (Clarke et al., 2009). Note that the set of models (Figure 3.3A) capable of explaining the dynamics of phospho-R-Smad decline all exhibited a negative correlation between the degree of Receptor Degradation and the degree of P-R-Smad Degradation (Figure 3.3F), suggesting that these two mechanisms would be balanced alternatives. In light of our experimental finding that Receptor

Degradation is a very weak effect, we next turned to P-R-Smad Degradation as the alternative slow-mode mechanism to explain the long-term decline of phospho-R-Smad.

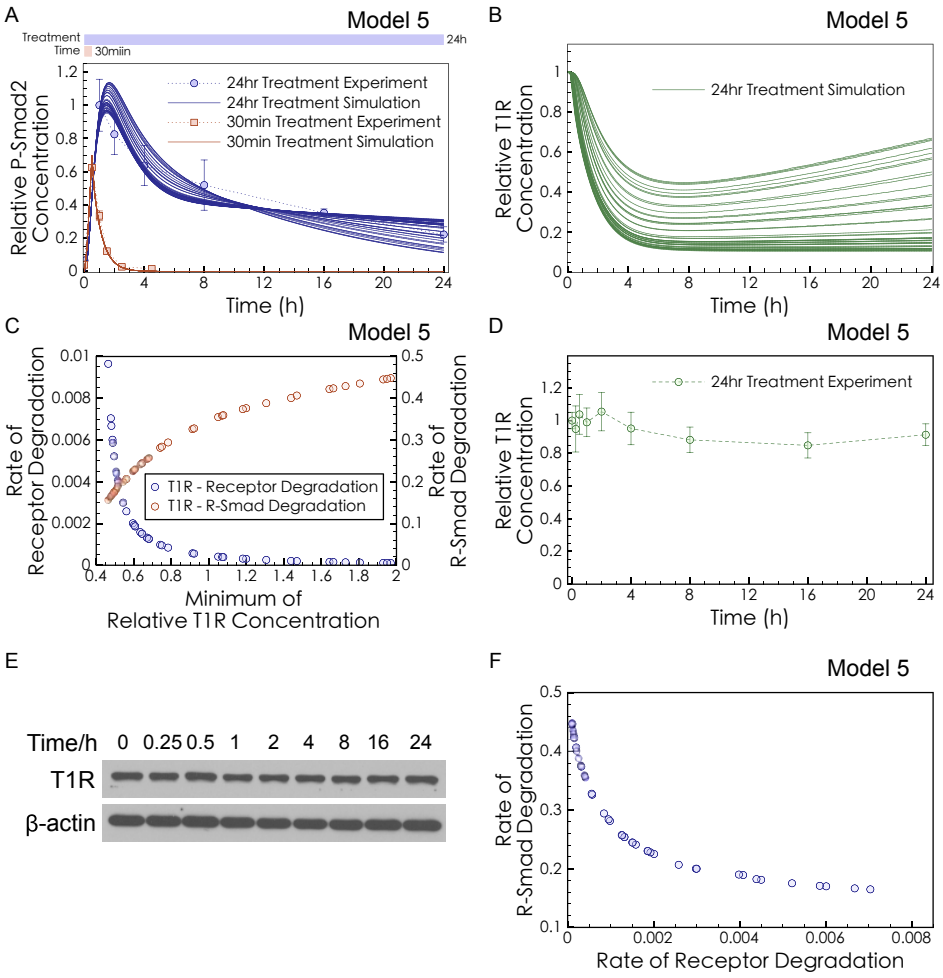

Figure 3.3 Predictions and validations of receptor degradation. (A) Different rates of I-Smad-induced receptor degradation (klid = 10-6 ~10-2) were applied to Model 5, and the rate of Smurf-induced P-R-Smad Degradation (kdegpSmad2) was fitted to the short-exposure experimental data (red dots) and the long-exposure experimental data (blue dots). All the other parameters were kept the same as those in Model 5 (B) Different Receptor Degradation rates led to different levels of the type I receptor (T1R). Green curves were generated from all models in panel (A) with klid = 10-6 ~10-2 and kdegpSmad2 estimated. (C) In the fitted models in panel (A), the T1R level has negative correlation with the Receptor Degradation rate (klid) but positive correlation with the P-R-Smad Degradation rate (kdegpSmad2). (D) Quantified data from 3 replicates of the western blot in (E). There is no significant loss of the T1R comparing the first and last data points ($P>0.05$). (E) Western blot of the T1R from whole cell lysates of HaCaT cells treated with TGF-β for 24hrs (representative of 3 replicates). (F) In the fitted models in panel (A), the rates of Receptor Degradation (klid) and P-R-Smad Degradation (kdegpSmad2) have negative correlation.

3.3.4 P-R-Smad Degradation Is Not Sufficient to Cause the Peak and Decay of Phosphorylated R-Smad

A model with R-Smad Dephosphorylation and P-R-Smad Degradation (Model 6, without Receptor Degradation) provided an excellent fit to both the long-exposure and short-exposure treatment data (Figure 3.4A). However, an unavoidable consequence of this model was dramatic decline of total R-Smad (Figure 3.4B). Previous experiments in HaCaT cells failed to observe a large fold-change of total R-Smad (Lin et al., 2006) but the amount of decline was not quantified. To clarify this potential conflict, we repeated the experimental measurement of total R-Smad levels after TGF-β treatment, using ELISA assays, a more quantitative method. Measurements of total R-Smad at 7 time points during 24hrs of TGF-β treatment showed no significant decrease of total R-Smad (Figure 3.4B-C). There is an apparent conflict between the constant level of total R-Smad (observed experimentally) and the significant degradation of R-Smad induced by TGF-β (according to Model 6). Note also that we see a plateau of phospho-R-Smad levels after 8 hrs (Figure 3.4C), but this is a minor discrepancy from the continuing decline seen by Lin *et al.* (Lin et al., 2006). The question of degradation becomes still more complex if degradation occurs in the presence of **Endogenous Synthesis and Degradation of R-Smad**, meaning the basal process of R-Smad turnover without TGF-β stimulation. We therefore expanded the model to include Endogenous Synthesis and Degradation of R-Smad (Model 7). If endogenous R-Smad is synthesized in an unphosphorylated form, and targeted by Smurf2 for degradation only in its phosphorylated form, then can P-R-Smad Degradation

explain the decline of phospho-R-Smad despite the constant levels of total R-Smad? However, Model 7 diverged strongly from the observed dynamics of phospho-R-Smad, when constrained to maintain a constant level of total R-Smad (Figure 3.4D).

Hence, our modeling analysis and experimental validation shows that current understanding of slow-mode negative regulation is not sufficient to explain phsopho-R-Smad dynamics. There might be some other mechanism that causes the peak and decline of phospho-R-Smad after the long-exposure of TGF-β.

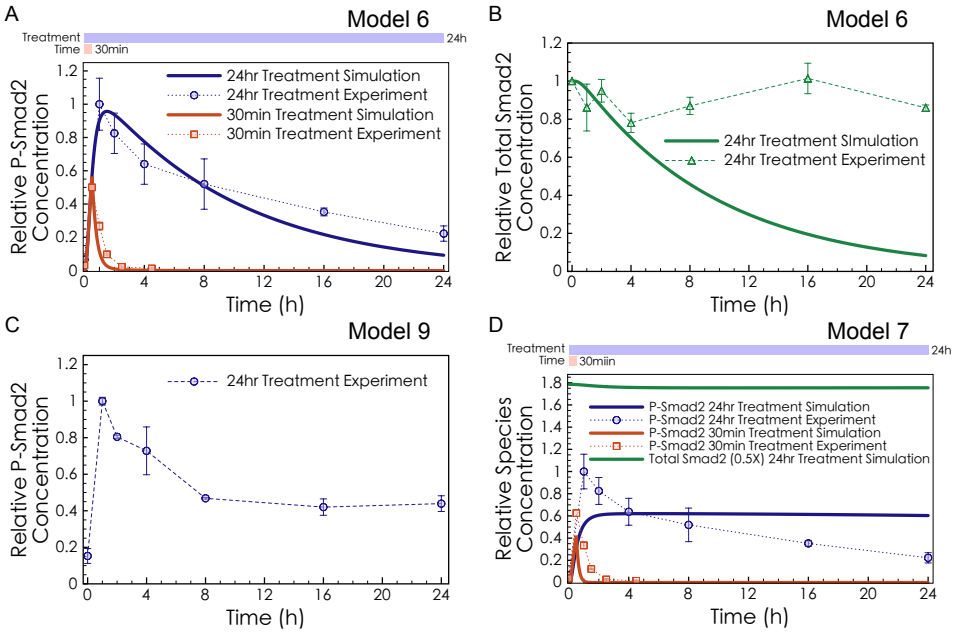

Figure 3.4 Simulations and experiments for P-R-Smad Degradation. (A) Model 6 with P-R-Smad Degradation and R-Smad Dephosphorylation (but no Receptor Degradation) was fitted to both the short-exposure (red) and long-exposure (blue) experimental data. (B) Model 6 predicted significant loss of total R-Smad (green curve), while ELISA measurements showed insignificant change ($P>0.05$, comparing the first and last data points) in total R-Smad concentration (green dots). (C) ELISA measurements of phospho-R-Smad are consistent with previous measurements performed by Western blot (Lin et al., 2006). Cell lysates were from the same samples as panel B. (D) Model 7 was fitted to the phospho-R-Smad data while constraining the total R-Smad level to be constant. Fitting used parameters $v_{Smad2} = 5.7143$ nMs^{-1} for R-Smad production, and $kdeg_{Smad2} = 0.01$ s^{-1} for R-Smad degradation.

3.3.5 Sensitivity Analysis of All Species to Two Degradation Mechanisms

Sensitivity analysis of Model 5 to perturbations in degradation rates revealed that T1R and total R-Smad are highly sensitive to changes in Receptor Degradation and P-R-Smad Degradation, respectively. Thus, our choices of T1R and total R-Smad measurements are sensitive to the mechanisms that we tested.

We performed sensitivity analysis on the parameters of Model 7 to determine which proteins levels would most sensitively reflect the behavior of degradation mechanisms in the model. We computed the local sensitivities of all species to the Receptor Degradation and P-R-Smad Degradation mechanisms. This was done by perturbing the parameters related to these mechanisms individually, and computing the effect of the perturbations on the protein levels. The parameters were perturbed by a spectrum of relative changes (from 10^{-4} to 10^{2}) with the expectation that changes within 10-fold would be most relevant. The sensitivities (Figure 3.5) indicate that the total type I receptor and total R-Smad levels have higher sensitivity than other proteins did, to the Receptor Degradation and P-R-Smad Degradation mechanisms, respectively. This confirms our choice of total T1R levels and total R-Smad levels for testing our hypotheses about receptor degradation and P-R-Smad degradation.

Different species are sensitive to different reactions or parameters in the model. This sensitivity analysis can also be applied to other species at other part of the signaling pathway. When we want to study certain mechanism or certain reaction in the pathway, it is often important to understand its sensitivity.

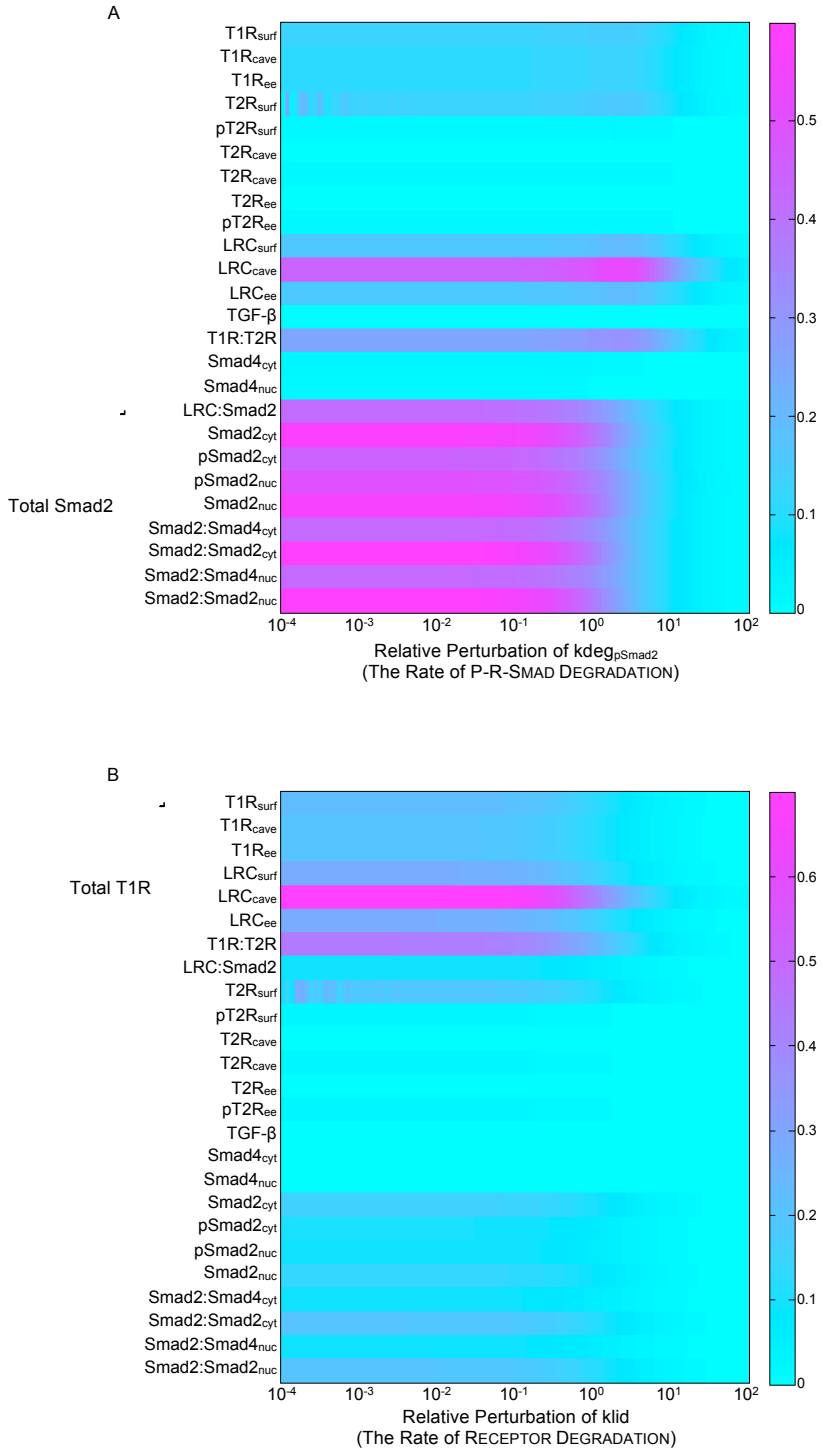

Figure 3.5 Sensitivity analysis heat map (Model 7). (A) The sensitivity of the P-R-Smad Degradation rate to each species with relative perturbations of the rate from 10^{-4} to 10^{2}. (B) The sensitivity of the receptor degradation rate to each species with relative perturbations of the rate from 10^{-4} to 10^{2}.

3.3.6 Extended I-Smad-Mediated Receptor Inhibitions

Our models (Model 1-7) were not capable of explaining experimental observations including the peak and decay of phospho-R-Smad, using only the three known negative regulatory mechanisms (Receptor Degradation, R-Smad Dephosphorylation and P-R-Smad Degradation). The loss of type I receptor caused by Receptor Degradation led us to degradation-independent I-Smad-mediated Receptor Inhibition mechanisms. One possible mechanism we considered for negative regulation of phospho-R-Smad is dephosphorylation of the receptor-ligand complex induced by I-Smad, which can recruit phosphatases in addition to E3-ligases (Shi et al., 2004). Dephosphorylation would inhibit the kinase activity of the type I receptor without affecting its concentration. The other mechanism is that I-Smad could bind to and block the active site of the type I receptor. Our model of Smad activation, adopted from previously published models, includes localization effects with caveolae and endosomes, which have distinct roles in receptor endocytosis. Because I-Smad co-localizes with caveolae (Di Guglielmo et al., 2003), we wanted to find a model fitting to the phospho-R-Smad data, in which I-Smad mainly associates with the ligand-receptor complex in caveolae, and in which the type I receptor is minimally lost. Figure 3.6 summarizes the results we got by extending the Receptor Inhibition mechanisms to include not only Receptor Degradation, but also Receptor Dephosphorylation and I-Smad Antagonism. As indicated by the red box, models were not capable of maintaining the observed concentrations of total T1R, while the I-Smad was co-localize with caveolae. We

were unable to construct an I-Smad-induced receptor inhibition mechanism that could explain the dynamics of phospho-R-Smad.

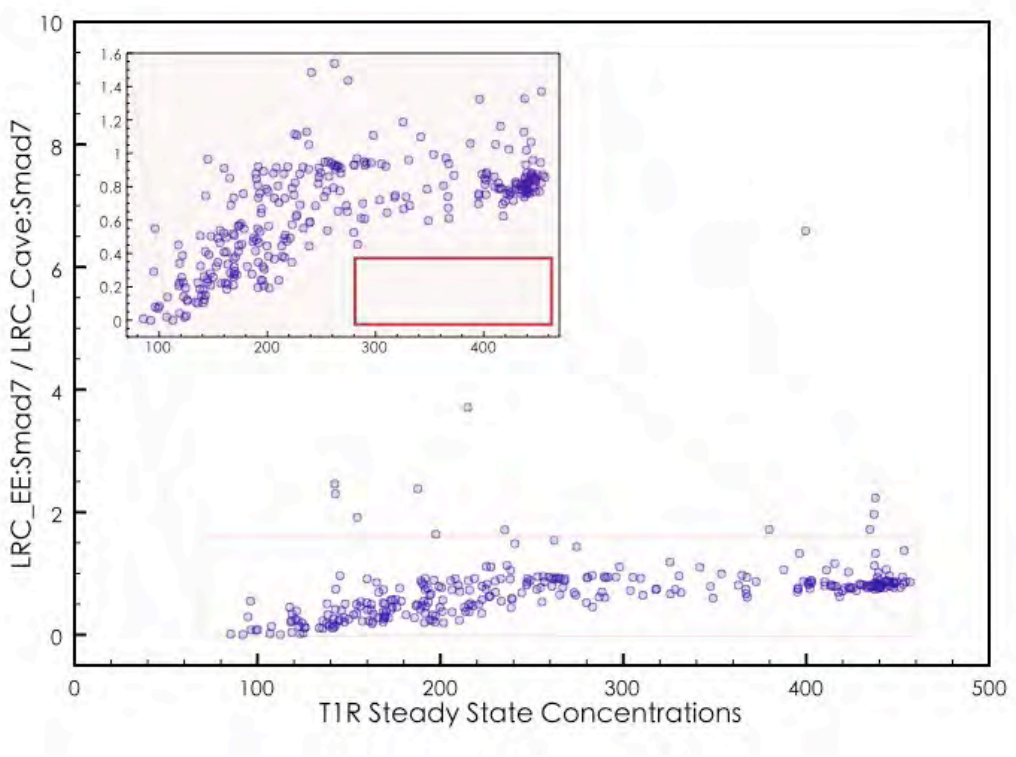

Figure 3.6 Fitted models with extended receptor inhibition mechanism (Model 8). Each blue point represents a single model. The x-axis is the type I receptor (T1R) level simulated at 24hr. The y-axis is the ratio of I-Smad-bound ligand-receptor complex in the early endosome and caveolae. We rescaled the axes to better visualize the majorities of the data points (upper left sub-figure). Models in the red box region should be able to explain both the type I receptor level and localization of I-Smad. However, no fitted model falls in the red box.

3.3.7 The Rate of Receptor Internalization Does Not Affect the Peak and Decline of phospho-R-Smad When TGF-β is Saturating

Receptor internalization has multiple effects on TGF-β/Smad signaling. Internalization is a part of signal transduction because internalization promotes association of the receptor kinase with its substrate R-Smad in the cytoplasm. At the same time, receptor internalization is also a negative regulatory mechanism as it reduces the availability of receptors on the cell surface. In other systems such as EGFR pathway, receptor internalization has been shown to cause down-regulation of downstream signals (Schoeberl et al., 2002). Thus we studied how receptor internalization could have a negative regulatory effect in our system. We first tested if varying the internalization rates in Model 1 could cause a peak and decline of phospho-R-Smad. The Adaptation Index was calculated as in Equation (3.1) to indicate the existence of a peak and decline. When a model has Adaptation Index=0, that means it has failed to show any decline of phospho-R-Smad.

$$\text{Adaptation Index} = \frac{[pSmad2]_{\max} - [pSmad2]_{t=24h}}{[pSmad2]_{t=24h}} \tag{3.1}$$

As shown in Figure 3.7A (blue curve), the Adaptation Index remained zero, even when the rate of internalization for the ligand-receptor complex (LRC) was changed by a factor of 10^{-3} to 10^{3}. This is mainly due to early reached steady state of LRC when TGF-β dose is saturating (data not shown). Although the internalization rate could not induce Model 1 to exhibit a peak and decline of phospho-R-Smad, there may be other conditions in which internalization rates would play an important role. To find such conditions, we did perturbation analysis of all rate constants in Model 1 to see if any other parameters combined with the

internalization rates could affect the Adaptation Index. We found that the Adaptation Index was most significantly increased when we decreased the production rate of T1R and increased the production rate of T2R (Figure 3.7C-D). It seems that decreasing the production rate of T1R and increasing the production rate of T2R by 10 fold in Model 1 would enhance the role of receptor internalization in the regulation of phospho-R-Smad. Indeed, inhibiting the internalization rates of LRC significantly blunted the peak of phospho-R-Smad (Figure 3.7B) and the internalization rates of LRC were positively correlated with the Adaptation Index (red curve, Figure 3.7A). However, in this scenario (low production of T1R and high production of T2R), the saturating dose of TGF-β was shifted significantly higher (Figure 3.7E-F). As shown in Figure 3.7F, 2ng/ml of TGF-β was no longer a saturating dose in this scenario. In contrast, we already know that 2ng/ml of TGF-β does saturate Smad signaling (Klipp and Zi, 2007, Zi et al., 2011). The scenario with low production of T1R and high production of T2R is not realistic for our system where 2ng/ml of TGF-β is a saturating dose, but at lower doses, receptor internalization could affect the peak and decline of phospho-R-Smad.

In summary, we have failed to identify any internalization parameters that could affect the Adaptation Index for phospho-R-Smad negative regulation, when TGF-β is saturating. In our system, we find receptor internalization does not contribute to explaining the peak and decline of phospho-R-Smad. As a result, we do not vary the parameters for receptor internalization in our analysis of negative regulatory mechanisms.

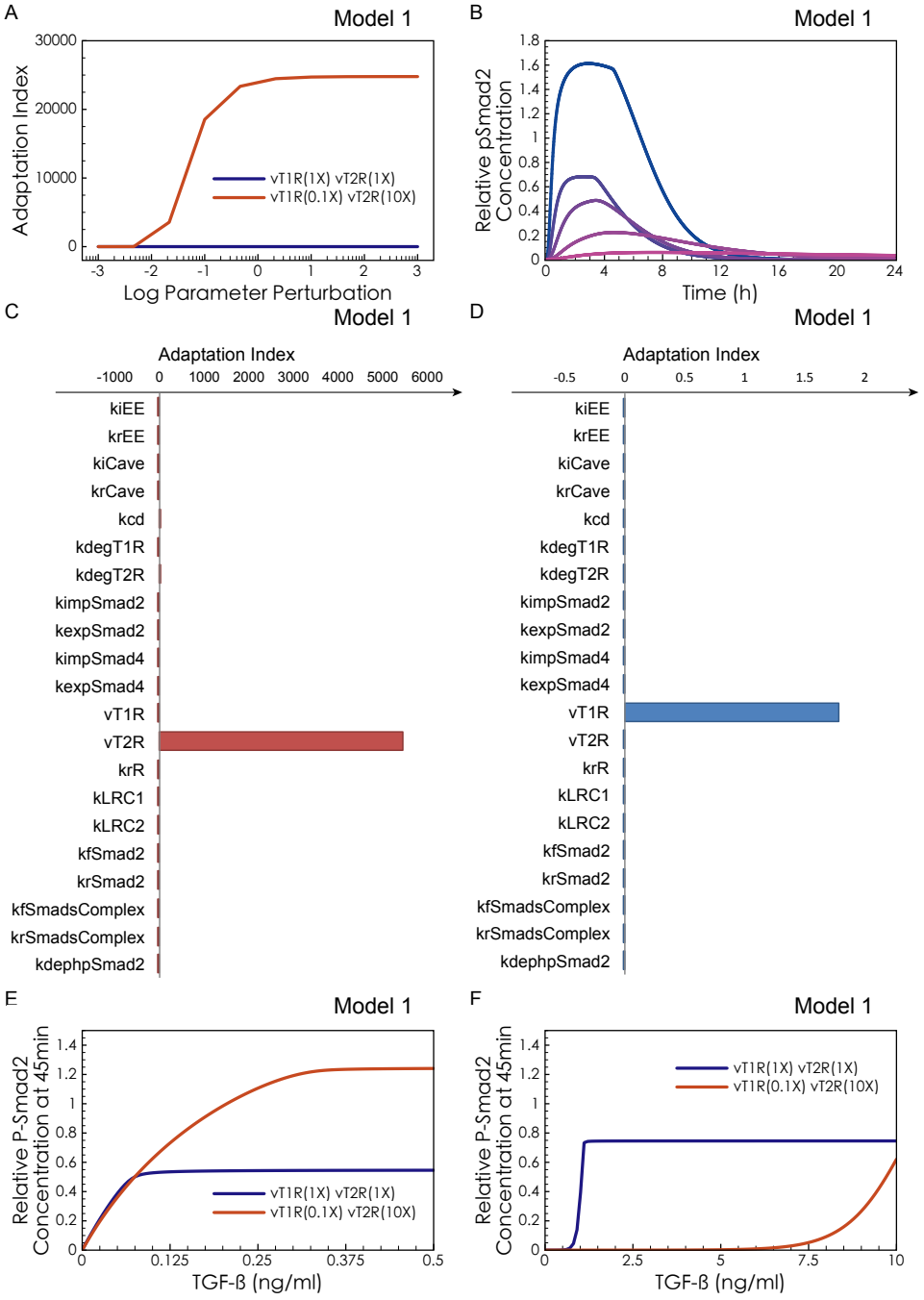
A
Model 1
Adaptation Index
30000
20000
10000
0
-3
-2
-1
0
1
2
3
Log Parameter Perturbation
vT1R(1X) vT2R(1X)
vT1R(0.1X) vT2R(10X)
B
Model 1
Relative pSmad2 Concentration
1.8
1.6
1.4
1.2
1
0.8
0.6
0.4
0.2
0
0
4
8
12
16
20
24
Time (h)
C
Model 1
Adaptation Index
-1000
0
1000
2000
3000
4000
5000
6000
kiEE
krEE
kiCave
krCave
kcd
kdegT1R
kdegT2R
kimpSmad2
kexpSmad2
kimpSmad4
kexpSmad4
vT1R
vT2R
krR
kLRC1
kLRC2
kfSmad2
krSmad2
kfSmadsComplex
krSmadsComplex
kdephpSmad2
D
Model 1
Adaptation Index
-0.5
0
0.5
1
1.5
2
kiEE
krEE
kiCave
krCave
kcd
kdegT1R
kdegT2R
kimpSmad2
kexpSmad2
kimpSmad4
kexpSmad4
vT1R
vT2R
krR
kLRC1
kLRC2
kfSmad2
krSmad2
kfSmadsComplex
krSmadsComplex
kdephpSmad2
E
Model 1
Relative P-Smad2 Concentration at 45min
1.4
1.2
1
0.8
0.6
0.4
0.2
0
0
0.125
0.25
0.375
0.5
TGF-ß (ng/ml)
vT1R(1X) vT2R(1X)
vT1R(0.1X) vT2R(10X)
F
Model 1
Relative P-Smad2 Concentration at 45min
1.4
1.2
1
0.8
0.6
0.4
0.2
0
0
2.5
5
7.5
10
TGF-ß (ng/ml)
vT1R(1X) vT2R(1X)
vT1R(0.1X) vT2R(10X)

Figure 3.7 Analysis of receptor internalization in Model 1. (A) Perturbation analysis of the rate of ligand-receptor complex (LRC) internalization. Log Parameter Perturbation is the log ratio of perturbed LRC internalization rate (the rate for internalizing early endosome and caveolae were changed with the same ratio) to its original value. Blue curve shows the result of perturbation analysis in Model 1, while red curve shows the result of perturbation analysis after changing the production rates of T1R (10-fold decrease) and T2R (10-fold increase) in Model 1. (B) Inhibition of LRC internalization in Model 1 after changing the production rates of T1R (10-fold decrease) and T2R (10-fold increase). Curves change from blue to red as LRC internalization rate decreases from 1 to 10^{-3} in log scale. (C) Adaptation Index change (x-axis) with 10-fold increase of each parameter. (D) Adaptation Index change (x-axis) with 10-fold decrease of each parameter. (E) Dose response at 45min. (F) Dose response at 45min. In panel E and F, blue curve shows dose response in Model 1, while red curve shows dose response in Model 1 after changing the production rates of T1R (10-fold decrease) and T2R (10-fold increase) in Model 1.

3.3.8 PPM1A Is Upregulated After Treatment with TGF-β

After exhausting the most widely-accepted mechanisms of Smad negative regulation, we proceeded to examine less obvious alternatives. We then systematically examined possible influences at each step along the Smad pathway, seeking quantitative consistency with the observed peak and decline of phospho-R-Smad. One scenario that could not be rejected on kinetic grounds was upregulation of PPM1A, the phosphatase targeting phospho-R-Smad. If PPM1A were to be upregulated by TGF-β signaling, this could affect the temporal decay of phospho-R-Smad. Model 9 permits the nuclear Smad complex to induce upregulation of PPM1A which in turn improved the fit of the model to the phospho-R-Smad data (Figure 3.8A), without changing the levels of T1R or total R-Smad (Figure 3.8B-C).

To test this model, we performed Western blots of the PPM1A protein after TGF-β treatment. HaCaT cells were treated with 2ng/ml of TGF-β and measured after 0.25, 0.5, 1, 2, 4, or 8hr. We found that the intensity of the PPM1A western blot band increased 2.4-fold after 1 hour of TGF-β treatment ($p<0.05$, Figure 3.8D-

E). To the best of our knowledge, this is the first study to report that TGF-β causes upregulation of the PPM1A phosphatase.

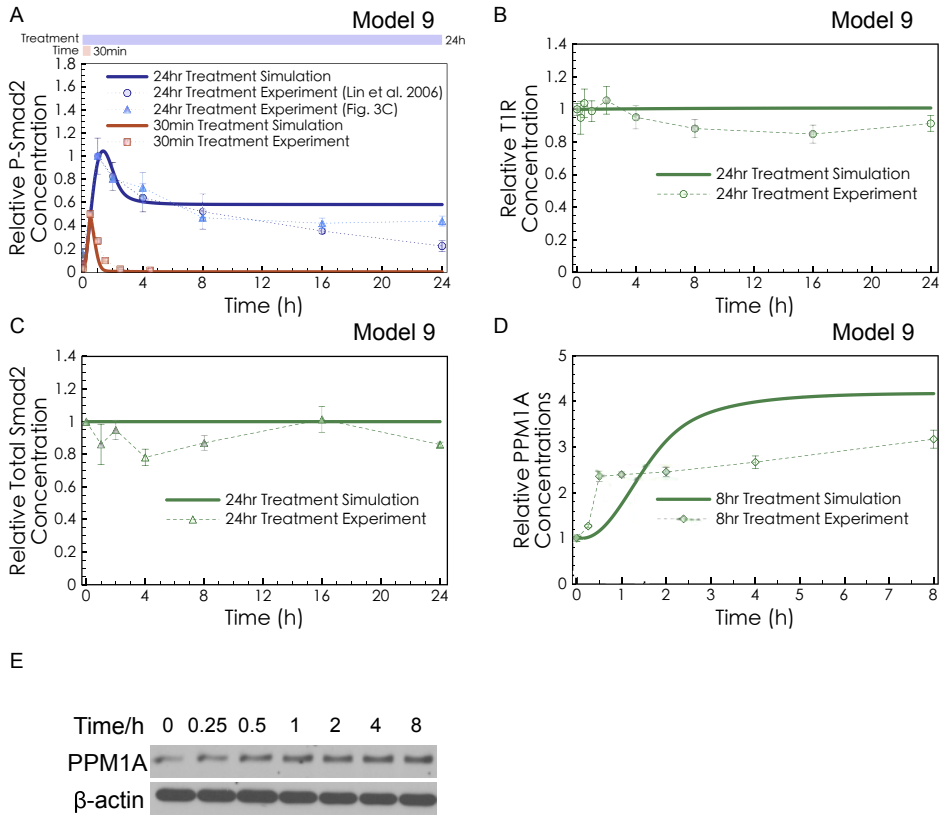

Figure 3.8 Predictions and validation of PPM1A Upregulation: (A) Model 9, in which PPM1A is upregulated by Smad complex in the nucleus, was fitted to the long-exposure and the short-exposure phospho-R-Smad experimental data. (B) Model 9 predicted unchanged T1R levels (green curve), in agreement with our experimental results (green dots). (C) Model 9 predicted unchanged total R-Smad levels (green curve), in agreement with our experimental results (green dots). (D) Model 9 predicted PPM1A upregulation under long-exposure of TGF-β (green curve). Our experimental validation showed significant upregulation of PPM1A (green dots, quantification from 3 Western blots, $P<0.05$ comparing the untreated data point and the 1hr data point). (E) Western blot of PPM1A in HaCaT cells with 2ng/ml TGF-β treatment, representative of 3 replicates.

3.3.9 Model-based Prediction of The Mechanism of PPM1A Upregulation

The time series measurements in Figure 3.8D showed a rapid increase of PPM1A protein levels, with steady state achieved by about 1hr. In contrast, the behavioral effect we were hoping to explain, the gradual down-regulation of phospho-R-Smad, lasts for at least 4hrs. The idealized Model 9 predicted PPM1A upregulation at 4hr and not 1hr (Figure 3.8E). Does the early upregulation of PPM1A fail to explain the extended down-regulation of phospho-R-Smad? We next built a hypothetical model, inspired by known PPM1A interactions, attempting to harmonize the observed effects.

Previous work does not indicate how PPM1A might be upregulated by TGF-β, but the speed of the effect suggests post-translational regulation (such as enhanced stability) or post-transcriptional regulation. PTEN has been shown in fibroblasts to associate with PPM1A and to protect PPM1A from proteasomal degradation (Bu et al., 2008). In the fibroblast context, TGF-β caused decreased levels of PPM1A, and caused dissociation of PTEN from phospho-R-Smad. It is possible that in our HaCaT system (keratinocytes), TGF-β could cause the opposite effect, upregulation of PPM1A, but also by regulating the association with PTEN. In HaCaT cells, TGF-β was reported to cause ***increased*** association between PTEN and phospho-R-Smad (Hjelmeland et al., 2005), not the dissociation observed in fibroblasts. We therefore propose model 10 (specific to HaCaT cells), in which TGF-β would induce stabilization of PPM1A by PTEN. In this model, we halted degradation of PPM1A whenever it was associated with PTEN, but PTEN was not allowed to form a

complex directly with PPM1A, (i.e., in the absence of TGF-β stimulation). Rather, a ternary complex of pSmad2:PTEN:PPM1A could form, and a PTEN:PPM1A complex could be released from the ternary complex. This recapitulates the observation that PTEN-Smad2 association is dependent on TGF-β stimulation (Hjelmeland et al., 2005). In this model, we required the upregulation of PPM1A protein to match the fast kinetics observed, but we also wanted the increased phosphatase activity against phospho-R-Smad to match the observed phospho-R-Smad dynamics. We do not know whether PPM1A activity, conformation, or localization would be changed by binding to PTEN. It is possible that PTEN-PPM1A association could cause some transient sequestration of PPM1A activity, which might delay the functional impact of PPM1A upregulation. In Model 10, we assumed that unbound PPM1A is rapidly imported into the nucleus, but PPM1A bound to PTEN has slow import into the nucleus. Because phospho-R-Smad accumulates in the nucleus, delayed nuclear import of PPM1A during PTEN-mediated stabilization would delay the functional impact of PPM1A activity, relative to the total PPM1A levels. Complete reaction equations and parameters appear in the Supporting Information. Model 10 successfully recapitulated the experimentally observed dynamics of phospho-R-Smad (Figure 3.9A); the fast kinetics of PPM1A upregulation (Figure 3.9B); and the unchanged levels of T1R and total R-Smad (Figure 3.9C-D).

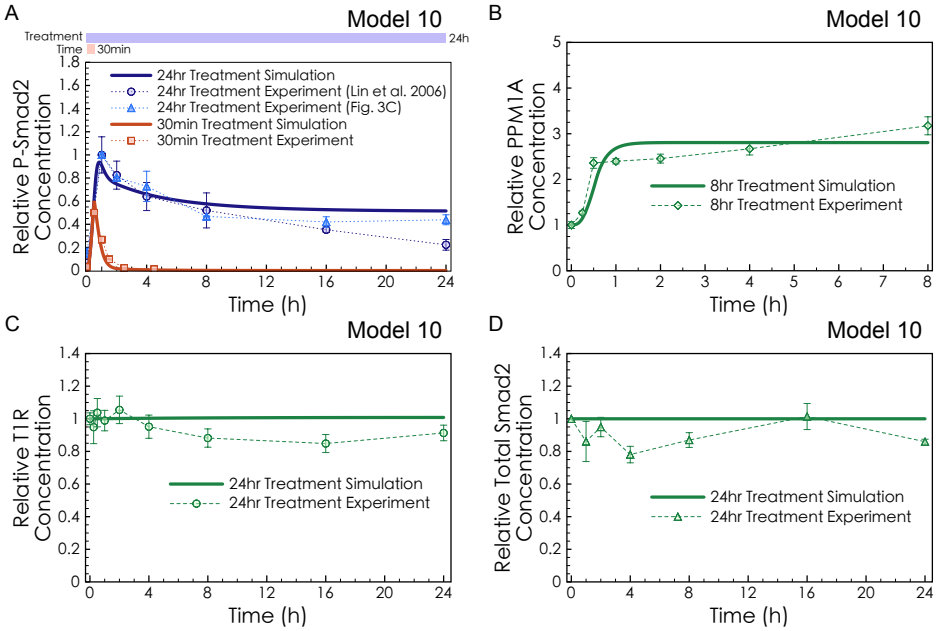

Figure 3.9 Model-based predictions of the mechanism of PPM1A Upregulation: (A) Model 10, in which PPM1A is stabilized by PTEN, was fitted to the long-exposure and the short-exposure phospho-R-Smad experimental data. (B) Model 10 predicted early PPM1A upregulation (within 1hr) under long-exposure treatments with TGF-β (green curve). This is in agreement with our experimental measurements of PPM1A (greed dots). (C) Model 10 predicted unchanged T1R levels (green curve), in agreement with our experimental results (green dots). (D) Model 10 predicted unchanged total R-Smad levels (green curve), in agreement with our experimental results (green dots).

3.3.10 The Role of P-R-Smad Degradation in the Context of PPM1A Stabilization

Model 10 is the first model in our series that is consistent with all the experimental data (including our own) for the impact of TGF-β on HaCaT cells. As shown in Figure 3.4, P-R-Smad Degradation could not by itself explain the long-term decline of phospho-R-Smad. We now examine the role of P-R-Smad Degradation in the context of Model 10 where PPM1A Stabilization is partially responsible for the Smad negative regulation. Previous studies assessed P-R-Smad Degradation using MG132 to inhibit proteasomal degradation, but with conflicting conclusions: Massague *et al.* saw a strong effect implying an important role for degradation (Lo and Massague, 1999, Alarcon et al., 2009), while Lin *et al.* found negligible effects of MG132 (Lin et al., 2006). Both protocols measured long-term behavior of pSmad2, but the Lin protocol triggered pSmad2 using a 30min exposure to TGF-β, while the Massague protocol used a 6h exposure. To examine this apparent conflict, we extended Model 10, adding Endogenous Synthesis and Degradation of R-Smad, and adding P-R-Smad Degradation, to obtain Model 11. Like Model 10, Model 11 shows a good fit to phospho-R-Smad dynamics (Figure 3.10A) and unchanged levels of total R-Smad (Figure 3.10B). Simulations of Model 11 with MG132 inhibition of proteasomal degradation show that MG132 would have minimal impact on Smad signaling, when triggered by brief exposure to TGF-β (Figure 3.10C). In surprising contrast, MG132 would have a strong impact on Smad signaling, when pSmad2 is triggered by longer exposures to TGF-β (Figure 3.10D). Figure 3.10E compares the P-Smad2 Change calculated from Figure 3.10C

(red curve) and Figure 3.10D (blue curve) with experimental data from Lin *et al.* (Lin et al., 2006) (red dots) and Alarcon *et al.* (Alarcon et al., 2009) (blue dots). The P-Smad2 Change was calculated as Equation (3.2). Model 11 thus provides mathematical support that the Lin observations and the Massague observations can occur in the same system. Finally, Model 11 demonstrates that PPM1A Stabilization, and P-R-Smad Degradation are consistent with, and sufficient to explain, the negative regulation and degradation nuances of the Smad signaling system.

$$\text{P-Smad2 Change}_{t=t_i} = \frac{[pSmad2_{total}^{-MG132}]_{t=t_i} - [pSmad2_{total}^{+MG132}]_{t=t_i}}{[pSmad2_{total}^{-MG132}]_{\max}} \qquad (3.2)$$

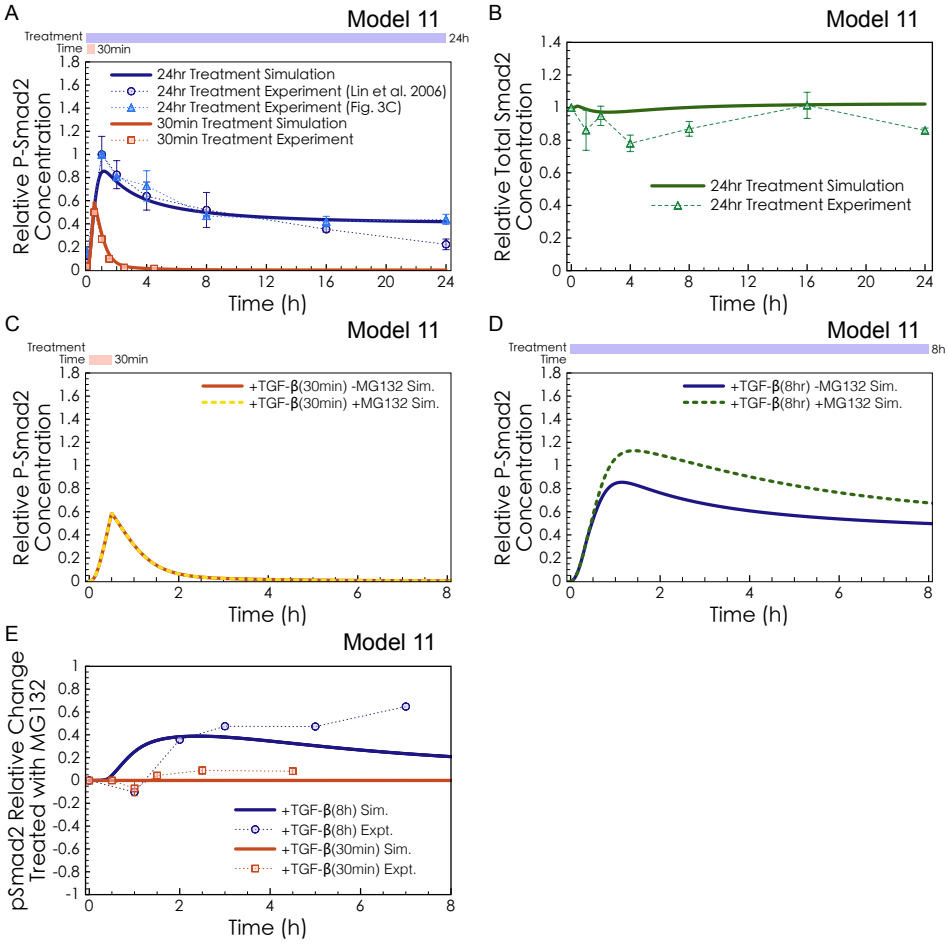

Figure 3.10 Combination of PP1MA Stabilization, P-R-Smad Degradation, R-Smad Endogenous Synthesis and Degradation: (A) Model 11, combining PP1MA Stabilization, P-R-Smad Degradation, R-Smad Endogenous Synthesis and Degradation, was fitted to the long-exposure and the short-exposure phospho-R-Smad experimental data. (B) Model 11 predicted unchanged total R-Smad levels (green curve), in agreement with our experimental results (green dots). (C) Red solid curve shows simulation of Model 11 with short-exposure (30min) of TGF-β, while the yellow dotted curve shows the same simulation except with MG132 pre-treatment. MG132 was simulated as turning off P-R-Smad Degardation ($kdeg_{pSmad2}=0$). (D) The blue solid curve shows simulation of Model 11 with long-exposure (8hr) of TGF-β, and the green dotted curve shows the same simulated except with MG132 pre-treatment. (E) The relative change in P-Smad2 levels after MG132 treatment, calculated from Eq. 1 and simulations of Model 11. The P-Smad2 change simulated using Model 11 in both short-exposure (30min, red curve) and long-exposure (8hr, blue curve) simulations was compared with the P-Smad2 change in the experimental results of Lin *et al.* (Lin et al., 2006) (30min-exposure, red dots) and Alarcon *et al.* (Alarcon et al., 2009) (6hr-exposure, blue dots). Data points from Alarcon *et al.* (Alarcon et al., 2009) were quantified from one published image. The discrepancy between our simulations and Alarcon et al for the 7hr measurement may be partially explained by MG132-independent differences. Their -MG132 control decreases much faster than that from Lin *et al.* (Lin et al., 2006) and from our experiments.

3.3.11 Transient and Sustained Signaling in the TGF-β Signaling Pathway

Our model with final model (Model 11) is also capable of producing the same dose-response behavior in short-term and long-term signals as shown by Klipp et al. (Zi et al., 2011). The phospho-R-Smad concentration at 45 min increased when the dose of TGF-β did (Figure 3.11A). But if the dose of TGF-β were high enough, the phospho-R-Smad concentration would be saturated at 45 min. The concentration of phospho-R-Smad did not remain elevated at 24 hr after TGF-β treatment unless the TGF-β dose exceeds a certain threshold (Figure 3.11B). This shows an ultrasensitive signaling response to TGF-β dose. We speculate that the saturation of the signal is mainly due to saturated TGF-β receptor, since R-Smad was not saturated (only 30% of the R-Smads were phosphorylated). If the receptors were saturated, then the dose of TGF- β only affects the duration, but not the intensity of the signal in the long-term (Figure 3.11C). This suggests that the reason for the decay of phosphorylated R-Smad with saturating TGF-β dose is down-stream regulatory mechanisms, but not the consumption of TGF-β.

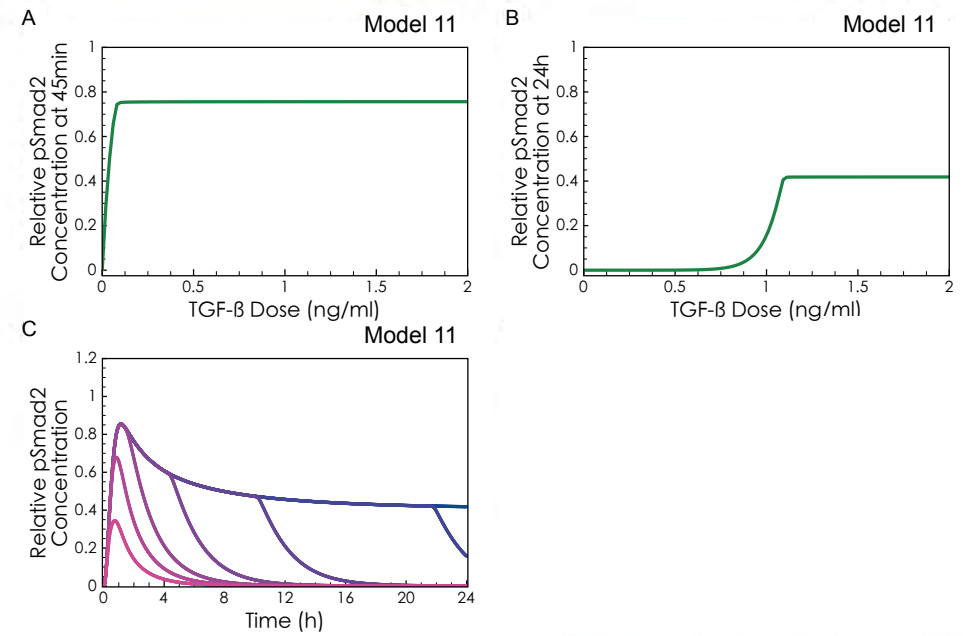

Figure 3.11 TGF-β dose response. (A) Simulated P-Smad2 levels at 45min under different doses of TGF-β treatment. (B) Simulated P-Smad2 levels at 24hr under different doses of TGF-β treatment. (C) Simulations of the P-Smad2 dynamics with different doses of TGF-β. The color of the curve turns from blue to red as TGF-β dose increases (0.025, 0.0625, 0.125, 0.25, 0.5, 1, 2ng/ml).

3.4 Discussion

Several negative regulatory mechanisms in the Smad signaling pathway have been identified and individually studied (Afrakhte et al., 1998, Itoh et al., 1998, Kavsak et al., 2000, Lin et al., 2006, Lo and Massague, 1999, Alarcon et al., 2009, Shi et al., 2004, Nakao et al., 1997). We focused our modeling and experiments on these specific mechanisms with published evidence. R-Smad Dephosphorylation by PPM1A is widely recognized to be a strong form of negative regulation, having significant fast-mode impact, but the relative importance of other mechanisms, compared with R-Smad Dephosphorylation, was not clear. We found that multiple combinations of fast-mode and slow-mode mechanisms could match the phospho-R-

Smad data moderately well, but these combinations (e.g., Models 2,5, and 6) could only recapitulate phospho-R-Smad dynamics at the expense of very strong, cumulative degradation; as much as 90% decrease of T1R at 24hr (Figure 3.3B), or 90% decrease in total R-Smad at 24hr (Figure 3.4B). Our experimental measurements in HaCaT found that total T1R protein levels did not decline significantly (Figure 3.3D) nor did total R-Smad (Figure 3.4B). This contrasts with previous work in 293T and COS-1 cells (Kavsak et al., 2000, Eichhorn et al., 2012). In (Kavsak et al., 2000), 293T cells were transfected with I-Smad which was able to induce significant receptor degradation. The significant degradation seen in (Kavsak et al., 2000) may be due to the effects of transfection (Clarke et al., 2009) or may be due to cell line differences. Although most dynamic models of signal transduction represent an amalgam of findings from multiple cell lines, our model (and the previous models we rely on) are specific to the HaCaT cell line. Thus a discrepancy with (Kavsak et al., 2000) is not necessarily a flaw of our model.

In light of our experimental measurement that TGF-β treatment does not cause any significant drop in R-Smad levels or T1R levels, we conclude that degradation effects, if they occur in HaCaT, must be counterbalanced by endogenous synthesis. Model 7 simulated a balance of synthesis and degradation (Endogenous Synthesis and Degradation of R-Smad) such that phospho-R-Smad was degraded while unphosphorylated Smad was synthesized; this model was not able to induce the observed long-term decay of phospho-R-Smad. We conclude that degradation of R-Smad or T1R, with or without endogenous synthesis, is not sufficient to explain the

slow-mode of Smad negative regulation in HaCaT cells. Degradation with synthesis remains a plausible effect but it must occur alongside other mechanisms.

After simulating all the previously published mechanisms of negative regulation, including Receptor Inhibition (See Model 8, Section 3.3.6)(Afrakhte et al., 1998, Itoh et al., 1998, Ebisawa et al., 2001, Hayashi et al., 1997, Kavsak et al., 2000), R-Smad Dephosphorylation (Lin et al., 2006), and P-R-Smad Degradation (Lo and Massague, 1999, Alarcon et al., 2009, Lin et al., 2000), no model could explain the "slow-mode" of phospho-R-Smad decline after long exposures to TGF-β, unless they violated the observations of other experiments. *In silico* exploration of hypothetical mechanisms led us to question whether PPM1A levels could change during Smad pathway activation (Model 9).

We then tested the model-inspired question, whether PPM1A is upregulated by TGF-β. PPM1A western blots showed 2.4-fold increase in PPM1A protein levels (Fig. 5D-E), suggesting a negative feedback effect, in which TGF-β upregulates PPM1A to control the levels of phospho-R-Smad. In Model 10 we studied how this novel finding might relate to the negative regulation of phospho-R-Smad. Not knowing the exact mechanism for TGF-β to cause upregulation of PPM1A, we simulated combinations of individual effects, many taken from reports in other contexts, to provide a theoretical model of PPM1A stabilization. PPM1A is known to be stabilized by PTEN (Bu et al., 2008). If TGF-β can promote PTEN-PPM1A interaction in HaCaT, that might explain the observed increase in PPM1A as a stabilization effect. Another consideration is that TGF-β can induce association between PTEN and R-Smad (Hjelmeland et al., 2005). The detailed interactions or

competitions among PTEN, R-Smad and PPM1A are not known, but we assumed that TGF-β would induce PTEN-PPM1A interaction and PPM1A stabilization through phosphorylation of R-Smad. A model simulating this assumption alone was not consistent with observations, so in Model 10 we further hypothesized that PTEN-mediated stabilization would temporarily sequester PPM1A, for example through decreased nuclear import of the PTEN-PPM1A complex. There are many plausible ways that PTEN-induced stabilization of PPM1A could sequester or delay PPM1A enzymatic activity, such as conformational change or post-translational modification. Our model shows one simplistic mechanism namely PPM1A Stabilization, with delayed nuclear import, was sufficient to reconcile the early upregulation of PPM1A total protein with later PPM1A effects on phospho-R-Smad. Our theoretical model could be useful for the design of experiments to determine how the upregulation actually occurs. Future work should test whether PPM1A is stabilized and/or sequestered by PTEN after TGF-β treatment in HaCaT, as illustrated in Models 10-11. Pull-down experiments could be applied to study the association among phospho-R-Smad, PPM1A and PTEN. The order of binding reaction might be complex and ternary complex may exist. Our model would recommend testing for PPM1A-PTEN binding at 30min-1hr to catch their peak interaction, but testing for increased PPM1A activity at 4hr, significantly later than the upregulation.

Our model and experimental validation suggested that PPM1A upregulation could be important to explain the peak and decline of phospho-R-Smad in long exposure to TGF-β. However, negative regulation of TGF-β pathway could be a

complex process and other mechanism may also be involved. Further study may also consider other effects such as scaffold proteins. Scaffold proteins can facilitate the association between receptor kinase and R-Smads. If scaffold proteins are down regulated or their activities are blocked under TGF-β treatment, phospho-R-Smad level might reduce.

Careful examination of a broader set of previous work reveals some effects that appear to be discrepancies. The steepness of phospho-R-Smad decline in HaCaT appears to differ between the experiments of Massague and colleagues in (Lo and Massague, 1999, Alarcon et al., 2009) (green curve in Figure 3.1A) versus the experiments of Lin *et al.* (Lin et al., 2006) (blue curve), which are similar to our results (Figure 3.4C) and similar to the results of (Zi et al., 2011). One possible explanation is a difference in the effective concentrations of TGF-β. TGF-β has a very short half-life, and the dissolving conditions, such as carrier protein concentration, can alter the effective concentration of TGF-β. Previous authors did not report how their TGF-β was dissolved, but we found that dissolving TGF-β without carrier protein led to a steeper decline of phospho-R-Smad, similar to Massague *et al.* (Lo and Massague, 1999, Alarcon et al., 2009) (data not shown). We believe this discrepancy in slope is a technicality of the experiments and not fundamental to the pathway analysis.

Recent work has shown the importance of TGF-β depletion as a determinant of Smad signaling kinetics, for cells treated with low doses of TGF-β (10pM and 25pM) (Clarke et al., 2009). Our work did not emphasize low-dose contexts, but our models are consistent with observed TGF-β depletion behaviors. Figure 3.11 shows

simulations of Model 11 with low-dose TGF-β treatments. Smad signaling was indeed dominated by TGF-β scarcity. When the Smad system was externally limited by TGF-β availability, self-limiting mechanisms and negative regulatory effects were not apparent. Negative self-regulation of the Smad system was strongly apparent in treatments with 2ng/ml (80pM) of TGF-β, which is the dose studied in most previous experimental and computational studies of Smad dynamics.

After successfully predicting PPM1A upregulation and achieving recapitulation of all available datasets, our final contribution was to address an existing controversy about the role of proteasomal degradation in Smad signaling. We discovered that an apparent conflict about the role of degradation was in fact a mutually consistent set of trajectories that can both emerge from a single model. Degradation is intuitively understood to be a cumulative effect seen in long-term observations, but in this case the duration of observation was irrelevant, and the crucial variable for degradation was the duration of the TGF-β stimulus. MG132 (an inhibitor of proteasomal degradation) had negligible effect on pSmad levels (at 1,2,4,6 hr), in a system triggered with 30min exposure to TGF-β, but MG132 had a significant effect on pSmad levels (at 1,2,4,6 hr), in a system triggered with long exposure to TGF-β. In other words, the importance of degradation in Smad signaling depended not on the timepoint at which p-Smad2 was measured, but rather on the duration with which the Smad system had been induced. The consistence between the two experiments can be rationalized in retrospect because degradation depends on the "area under the curve," which is large in systems with prolonged stimulus, and very small in systems with short stimulus. However, the

consistency between Lin *et al.* and Massague *et al.* was not apparent prior to modeling, and mathematical inference of kinetic implications is dramatically different from the interpretations provided by the previous authors.

Our modeling provides a consistent, quantitative, and fine-grained integration of available information about the negative regulation of phospho-R-Smad, both from published literature and from our experiments. Our integration of modeling with experiments showed that published mechanisms such as Receptor Degradation have a minor effect, and led us to discover upregulation of PPM1A. Modeling can make additional predictions (e.g., future experiments should test for peak perturbation of PPM1A binding and activity.) Also modeling has provided a new and non-obvious interpretation for the effects of MG132 treatment. When interpreting the biological meaning of observed kinetics, informal intuition can unwittingly lead to flawed conclusions. Our updated model of Smad signaling may in the future be useful to other researchers interpreting data, designing experiments, or strategizing therapeutic perturbations. The field of biochemistry has a long history of using kinetics to gain insight into mechanism. Likewise our work has studied kinetic as our concrete contribution, but the larger outcome is to shed light on mechanisms.

Our final model of TGF-β pathway made some improvement to current state-of-art of TGF-β pathway modeling. Thus, it is better to integrate our model of TGF-β pathway Venkatraman's upstream model of TGF-β activation, as the upstream model treated TGF-β signaling pathway as a black box. This integration is useful to study the important factors to the bistable behavior in the whole

system. For example, integrating the upstream and downstream networks could help to discover combination of drug targets in both upstream and downstream networks which could cause synergistic effect.

As we mentioned earlier in the introduction (Chapter 1), the upstream network takes the averaged response from Smad pathway in a population of cells. Cell-to-cell variability may also be an important factor affecting the bistable behavior of the system. It is better to integrate an upstream network with a population of downstream networks. However, to simulate such a network is time-consuming. Therefore, we sought to develop efficient algorithms to simulate or approximate network behaviors from a population of cells. Assuming molecules are mixed fast enough in the upstream network, we can integrate the upstream network and the output of a population of downstream networks.

4 Chapter 4: Approximating Cell-population Behavior of Signaling Pathways Based on Single-cell Models

4.1 Introduction

Cell-to-cell variability and heterogeneity has been paid more and more attention in study of signaling pathways and other cell behaviors. This trend emerged mainly because of advanced single-cell based techniques for biological studies developed and applied in the past decade, such as imaging and flow cytometry. The earlier studies of signaling pathways assume homogeneity of monoclonal cell populations. However, single-cell based methods show significant cell-to-cell viability in a variety of signaling pathways including EGFR pathway, NFκB pathway (Lee and Covert, 2010), TRAIL-induced apoptosis pathway (Tay et al., 2010, Spencer et al., 2009a).

Although the difference between single-cell and cell-population behaviors has been shown, most systems biology studies of signaling pathways are still based on bulk experiments because most of the knowledge and data is available in bulk experiments. Thus, systems biologists often need to compare single-cell based model to cell-population based experiments. In order to do this, Monte Carlo simulation could be used in the way that simulation results from multiple models representing multiple cells are averaged to get the cell-population simulation. However, Monte Carlo simulation usually needs a large number of simulations to converge to the

averaged results. This is very time-consuming to just simulate the cell-population behaviors and it is not possible to estimate parameters because one parameter estimation procedure often takes thousands of simulations. Therefore, it would be very useful if we can simulate cell-population behaviors using single-cell models faster. If the simulation is fast enough, we may even estimate parameters of both single-cell models and cell-to-cell variability by comparing simulated cell-population behaviors to bulk experimental data.

In this study, we developed two approaches to approximate cell-population simulation using single-cell models, assuming the initial concentrations of all species vary from cell to cell. In the first approach, we derived Population ODE that approximates the means of concentrations of all species. This approach needs only one simulation. It is significantly faster than Monte Carlo simulation which needs thousands of simulations. But in some biological systems, such as bistable systems, Population ODE does not approximate the population behavior well enough. We then developed our second approach. The second approach, Sample Reduction, is by significantly reducing the dimension of sampling space and further reduces the number of samples required. This approach is a sampling-based approach, similar to Monte Carlo simulation. However, our approach significantly reduces the sample size and facilitates the simulation of population behavior.

4.2 Materials and Methods

4.2.1 Construction of Population ODE

The Population ODE requires the $\boldsymbol{A^1}$ and $\boldsymbol{A^2}$ matrices and the $\boldsymbol{k}$ vector from single-cell models. We used KroneckerBio toolbox (Toettcher et al., 2011) in Matlab to build the models and KroneckerBio toolbox generated the $\boldsymbol{A^1}$ and $\boldsymbol{A^2}$ matrices and the $\boldsymbol{k}$ vector we need. These matrices and vector were then built into the Matlab ode files and the function ode15s in Matlab was used to simulate the Population ODE.

4.2.2 Initial Distribution of Species Concentrations and Monte Carlo Simulation

In all the cases we studied, we assumed the initial distribution of species concentration as a Gaussian distribution with expected value of its original initial concentration and with standard deviation of 20% of its original initial concentration. The variation of species with non-zero initial concentration was considered. The initial concentrations of the other species were kept 0. In Monte Carlo simulation, we randomly sampled the species with non-zero initial concentration individually as we assumed that they were independent at time 0.

In Monte Carlo simulation, it is possible that random sampling from a Gaussian distribution will generate negative values for initial concentrations. As this chance is low based on our assumption, we simply ignored those samples with negative initial concentrations.

4.2.3 Sample Reduction in the Case of Apoptosis Pathway

The sensitivity matrix was calculated at 20 different time points in this case. The time points were chosen according to $\frac{dy}{dt}$, in which y was the output species (activated caspase 3). The time steps were set to satisfy the condition below so that the larger $\frac{dy}{dt}$ was, the smaller the time step.

$$T_1\left(\left.\frac{dy}{dt}\right|_{t=T_1}\right)=T_2\left(\left.\frac{dy}{dt}\right|_{t=T_2}\right)=\cdots=T_n\left(\left.\frac{dy}{dt}\right|_{t=T_n}\right)\ ,\quad (n=20) \tag{4.1}$$

4.2.4 Integration of Upstream Network of TGF-β Activation and Downstream Smad Signaling

To integrate these two networks, we need to break up two black-box reactions in Venkatraman's model, in which TSP1 production rate and PAI1 production rate are respectively $kp1[TGF\beta]$ and $kp2[TGF\beta]$. Then we modeled these two black boxes explicitly with Smad signaling pathway. Thus, the production rates of TSP1 and PAI1 should be proportional to Smad complexes in the nucleus as these complexes are the species regulating gene expressions. We therefore set the production rates of TSP1 and PAI1 to be $kp1([Smad24_{nuc}]+[Smad22_{nuc}])$ and $kp2([Smad24_{nuc}]+[Smad22_{nuc}])$. Since TGF-β already existed in both networks, we simply merged TGF-β in both networks to a single species. Hence, we have integrated the upstream network of TGF-β activation and downstream Smad signaling. Note that the parameters *kp1* and *kp2* should not have the sample value as in Venkatraman's model because the concentrations of TGF-β and Smad complexes are different.

4.3 Results

Cell-to-cell variability may be caused by variations of different factors, such as different concentrations of molecules, mutations of molecules, and different responses to environmental change. Correspondingly, there are different ways we can introduce different types of variations to the ODE system which models cellular behaviors. In the ODE system, variations can come from initial concentrations, reaction rate constants, and time varying input functions. Variation in initial concentrations can represent different concentrations of molecules in different cells. Variation in rate constants can reflect mutations of molecules, for example. Stochastic time varying input function is a more general way to model cell-to-cell variability than the previous two. This can be used to model variation sources which are not modeled by the ODE system. Different ways of modeling variations need different simulation strategies. Here, we develop simulation strategies for one type of variations which is the variation in initial concentration of molecules. In this case, we assume that the different cells have only different initial concentrations in the ODE system. Any other part of the ODE system, including rate constants, network structure, is assumed to be the same among different cells.

4.3.1 Propagating Population ODE System Based on Single-Cell ODE Model

In Chapter 2 (Section 2.1.4), we have introduced ODE model for Mass Action Kinetics. Mass Action Kinetics can be applied to describe the rate of most biochemical reactions. We have also showed how the ODEs of any type of Mass Action Kinetics can be written in a form of Kronecker product (Section 2.1.4.1,

repeated as in Equation (4.2)). This Kronecker product form of ODEs below is the basis for our mathematical derivation of the Population ODEs.

$$\frac{d\boldsymbol{x}}{dt} = \boldsymbol{A^1 x} + \boldsymbol{A^2 x} \otimes \boldsymbol{x} + \boldsymbol{k} \tag{4.2}$$

4.3.1.1 Derived ODEs for the population mean requires the value of the covariance matrix

Simulation of cell-population result can be easily achieved by Monte-Carlo simulation. But it is time consuming because it needs to simulate multiple samples of single-cell ODE systems. To facilitate the population, we want to derive a Population ODE model based on the single-cell ODE system, and this population ODE system determines the time-evolution of the population mean of each species concentration. With this population ODE system, we are able to simulate the population mean of each species concentration without sampling. To achieve that, we denote each species concentration as $x_i = \mu_i + \delta_i$, where μ_i denotes the expected value (population mean) of all x_i , and δ_i is a variable representing the variation of species concentration among different cells. To write concentrations of all species together, we have the vector form $\boldsymbol{x} = \boldsymbol{\mu} + \boldsymbol{\delta}$. Here, both $\boldsymbol{x}(t)$ and $\boldsymbol{\delta}(t)$ are functions of t and random variables varying among different cells. In other words, we want to derive $\frac{d\boldsymbol{\mu}}{dt}$ based on $\frac{d\boldsymbol{x}}{dt}$ using the substitution $\boldsymbol{x} = \boldsymbol{\mu} + \boldsymbol{\delta}$.

Taking expected value of both sides of Equation (4.2), we have,

$$
\begin{aligned}
E\left(\frac{d\boldsymbol{x}}{dt}\right) &= \boldsymbol{A}^1 E(\boldsymbol{x}) + \boldsymbol{A}^2 E(\boldsymbol{x}\otimes\boldsymbol{x}) + \boldsymbol{k} \\
&= \boldsymbol{A}^1\boldsymbol{\mu} + \boldsymbol{A}^2 E[(\boldsymbol{\mu}+\boldsymbol{\delta})\otimes(\boldsymbol{\mu}+\boldsymbol{\delta})] + \boldsymbol{k} \\
&= \boldsymbol{A}^1\boldsymbol{\mu} + \boldsymbol{A}^2[\boldsymbol{\mu}\otimes\boldsymbol{\mu} + E(\boldsymbol{\delta}\otimes\boldsymbol{\delta})] + \boldsymbol{k}
\end{aligned}
\tag{4.3}
$$

Note that

$$
E(\boldsymbol{\delta}\otimes\boldsymbol{\delta}) = vec\begin{pmatrix} \delta_1\delta_1 & \cdots & \delta_n\delta_1 \\ \vdots & \ddots & \vdots \\ \delta_1\delta_n & \cdots & \delta_n\delta_n \end{pmatrix} = vec(\boldsymbol{C}^T) \tag{4.4}
$$

Thus,

$$
\frac{d\boldsymbol{\mu}}{dt} = E\left(\frac{d\boldsymbol{x}}{dt}\right) = \boldsymbol{A}^1\boldsymbol{\mu} + \boldsymbol{A}^2\boldsymbol{\mu}\otimes\boldsymbol{\mu} + \boldsymbol{A}^2 vec(\boldsymbol{C}^T) + \boldsymbol{k} \tag{4.5}
$$

Here, $vec(\boldsymbol{C}^T)$ denotes the vec operation of the transpose of the covariance matrix $\boldsymbol{C}$. Note that the time-evolution of $\boldsymbol{\mu}(t)$ depends on not only itself but also the covariance matrix. Equation (4.5) is also a proof to the concept that the behavior of a population of cells is different from that of a single cell. The covariance matrix $\boldsymbol{C}$ also evolves with time. Therefore, in order to compute $\boldsymbol{C}$ which is required for computing $\frac{d\boldsymbol{\mu}}{dt}$, we further derive ODEs for $vec(\boldsymbol{C}^T)$.

4.3.1.2 Approximating time-evolution of the covariance matrix by ignoring the third moment

Taking expected value of $\boldsymbol{\delta}\otimes\boldsymbol{\delta}$, we have

$$
\begin{aligned}
E[vec(\boldsymbol{C}^T)] &= E(\boldsymbol{\delta}\otimes\boldsymbol{\delta}) \\
&= E[(\boldsymbol{x}-\boldsymbol{\mu})\otimes(\boldsymbol{x}-\boldsymbol{\mu})] \\
&= E[\boldsymbol{x}\otimes\boldsymbol{x}] - \boldsymbol{\mu}\otimes\boldsymbol{\mu}
\end{aligned}
\tag{4.6}
$$

Therefore

$$\frac{dvec(\boldsymbol{C}^T)}{dt} = E\left(\frac{d\boldsymbol{x}\otimes\boldsymbol{x}}{dt}\right) - \frac{d\boldsymbol{\mu}\otimes\boldsymbol{\mu}}{dt} \tag{4.7}$$

Then we derive the two terms on the right hands side of Equation (4.7) separately. For the first term,

$$\begin{aligned}\frac{d(\boldsymbol{x}\otimes\boldsymbol{x})}{dt} &= \boldsymbol{x}\otimes\frac{d\boldsymbol{x}}{dt} + \frac{d\boldsymbol{x}}{dt}\otimes\boldsymbol{x} \\ &= \boldsymbol{x}\otimes(\boldsymbol{A}^1\boldsymbol{x} + \boldsymbol{A}^2\boldsymbol{x}\otimes\boldsymbol{x} + \boldsymbol{k}) + (\boldsymbol{A}^1\boldsymbol{x} + \boldsymbol{A}^2\boldsymbol{x}\otimes\boldsymbol{x} + \boldsymbol{k})\otimes\boldsymbol{x}\end{aligned} \tag{4.8}$$

Applying the rule $(\boldsymbol{A}\otimes\boldsymbol{B})(\boldsymbol{C}\otimes\boldsymbol{D}) = (\boldsymbol{AC})\otimes(\boldsymbol{BD})$ and taking expected value on both sides of Equation (4.8), we have

$$\begin{aligned}\frac{dE(\boldsymbol{x}\otimes\boldsymbol{x})}{dt} &= (\boldsymbol{A}^1\otimes\boldsymbol{I} + \boldsymbol{I}\otimes\boldsymbol{A}^1)E(\boldsymbol{x}\otimes\boldsymbol{x}) \\ &\quad +(\boldsymbol{A}^2\otimes\boldsymbol{I} + \boldsymbol{I}\otimes\boldsymbol{A}^2)E(\boldsymbol{x}\otimes\boldsymbol{x}\otimes\boldsymbol{x}) \\ &\quad +\boldsymbol{\mu}\otimes\boldsymbol{k} + \boldsymbol{k}\otimes\boldsymbol{\mu}\end{aligned} \tag{4.9}$$

The term $E(\boldsymbol{x}\otimes\boldsymbol{x})$ can be expressed by $\boldsymbol{\mu}$ and $vec(\boldsymbol{C}^T)$ as in Equation (4.6). Then we need to express $E(\boldsymbol{x}\otimes\boldsymbol{x}\otimes\boldsymbol{x})$ by $\boldsymbol{\mu}$ and $vec(\boldsymbol{C}^T)$ as well. To simplify the derivation, we derive $E(\boldsymbol{\delta}\otimes\boldsymbol{\delta}\otimes\boldsymbol{\delta})$ instead.

$$\begin{aligned}E(\boldsymbol{\delta}\otimes\boldsymbol{\delta}\otimes\boldsymbol{\delta}) &= E[(\boldsymbol{x}-\boldsymbol{\mu})\otimes(\boldsymbol{x}-\boldsymbol{\mu})\otimes(\boldsymbol{x}-\boldsymbol{\mu})] \\ &= E(\boldsymbol{x}\otimes\boldsymbol{x}\otimes\boldsymbol{x}) + 2\boldsymbol{\mu}\otimes\boldsymbol{\mu}\otimes\boldsymbol{\mu} \\ &\quad -E(\boldsymbol{x}\otimes\boldsymbol{x}\otimes\boldsymbol{\mu}) - E(\boldsymbol{x}\otimes\boldsymbol{\mu}\otimes\boldsymbol{x}) - E(\boldsymbol{\mu}\otimes\boldsymbol{x}\otimes\boldsymbol{x}) \\ &= E(\boldsymbol{x}\otimes\boldsymbol{x}\otimes\boldsymbol{x}) - \boldsymbol{\mu}\otimes\boldsymbol{\mu}\otimes\boldsymbol{\mu} \\ &\quad -vec(\boldsymbol{C}^T)\otimes\boldsymbol{\mu} - E(\boldsymbol{\delta}\otimes\boldsymbol{\mu}\otimes\boldsymbol{\delta}) - \boldsymbol{\mu}\otimes vec(\boldsymbol{C}^T)\end{aligned} \tag{4.10}$$

Note that

$$
\begin{aligned}
E(\boldsymbol{\delta}\otimes\boldsymbol{\mu}\otimes\boldsymbol{\delta}) &= E\left[\begin{array}{c}
\left(\begin{array}{c}\delta_1\mu_1\boldsymbol{\delta}\\ \vdots \\ \delta_1\mu_n\boldsymbol{\delta}\end{array}\right)_1 \\
\vdots \\
\left(\begin{array}{c}\delta_n\mu_1\boldsymbol{\delta}\\ \vdots \\ \delta_n\mu_n\boldsymbol{\delta}\end{array}\right)_n
\end{array}\right] \\
&= E\left[vec\left(\begin{array}{ccc}\delta_1\mu_1\boldsymbol{\delta} & \cdots & \delta_n\mu_1\boldsymbol{\delta}\\ \vdots & \ddots & \vdots \\ \delta_1\mu_n\boldsymbol{\delta} & \cdots & \delta_n\mu_n\boldsymbol{\delta}\end{array}\right)\right] \\
&= E\left\{vec\left[\boldsymbol{\mu}\otimes\left(\begin{array}{ccc}\delta_1\boldsymbol{\delta} & \cdots & \delta_n\boldsymbol{\delta}\end{array}\right)\right]\right\} \\
&= vec(\boldsymbol{\mu}\otimes\boldsymbol{C}^T)
\end{aligned}
\tag{4.11}
$$

Thus, from Equation (4.6) and Equation (4.10), we have

$$
\begin{cases}
E(\boldsymbol{x}\otimes\boldsymbol{x}) = \boldsymbol{\mu}\otimes\boldsymbol{\mu} + vec(\boldsymbol{C}^T) \\
\begin{aligned}
E(\boldsymbol{x}\otimes\boldsymbol{x}\otimes\boldsymbol{x}) &= \boldsymbol{\mu}\otimes\boldsymbol{\mu}\otimes\boldsymbol{\mu} \\
&+\boldsymbol{\mu}\otimes vec(\boldsymbol{C}^T) + vec(\boldsymbol{C}^T)\otimes\boldsymbol{\mu} + vec(\boldsymbol{\mu}\otimes\boldsymbol{C}^T) \\
&+E(\boldsymbol{\delta}\otimes\boldsymbol{\delta}\otimes\boldsymbol{\delta})
\end{aligned}
\end{cases}
\tag{4.12}
$$

Substituting with Equation (4.12), we can write Equation (4.9) as

$$
\begin{aligned}
\frac{dE(\boldsymbol{x}\otimes\boldsymbol{x})}{dt} &= (\boldsymbol{A^1}\otimes\boldsymbol{I}+\boldsymbol{I}\otimes\boldsymbol{A^1})[\boldsymbol{\mu}\otimes\boldsymbol{\mu}+vec(\boldsymbol{C}^T)] \\
&+(\boldsymbol{A^2}\otimes\boldsymbol{I}+\boldsymbol{I}\otimes\boldsymbol{A^2})[\boldsymbol{\mu}\otimes\boldsymbol{\mu}\otimes\boldsymbol{\mu} \\
&+\boldsymbol{\mu}\otimes vec(\boldsymbol{C}^T)+vec(\boldsymbol{C}^T)\otimes\boldsymbol{\mu}+vec(\boldsymbol{\mu}\otimes\boldsymbol{C}^T) \\
&+E(\boldsymbol{\delta}\otimes\boldsymbol{\delta}\otimes\boldsymbol{\delta})] \\
&+\boldsymbol{\mu}\otimes\boldsymbol{k}+\boldsymbol{k}\otimes\boldsymbol{\mu}
\end{aligned}
\tag{4.13}
$$

Hence, we have derived the first term on the right hand side of Equation (4.7). Then we need to derive the second term.

$$
\frac{d\boldsymbol{\mu}\otimes\boldsymbol{\mu}}{dt} = \boldsymbol{\mu}\otimes\frac{d\boldsymbol{\mu}}{dt}+\frac{d\boldsymbol{\mu}}{dt}\otimes\boldsymbol{\mu}
\tag{4.14}
$$

Substituting $\frac{d\boldsymbol{\mu}}{dt}$ using Equation (4.5) and applying the rule $(\boldsymbol{A}\otimes\boldsymbol{B})(\boldsymbol{C}\otimes\boldsymbol{D})=(\boldsymbol{AC})\otimes(\boldsymbol{BD})$, we have

$$\begin{aligned}\frac{d\boldsymbol{\mu}\otimes\boldsymbol{\mu}}{dt} &= (\boldsymbol{A^1}\otimes\boldsymbol{I}+\boldsymbol{I}\otimes\boldsymbol{A^1})(\boldsymbol{\mu}\otimes\boldsymbol{\mu}) \\ &\quad +(\boldsymbol{A^2}\otimes\boldsymbol{I}+\boldsymbol{I}\otimes\boldsymbol{A^2})(\boldsymbol{\mu}\otimes\boldsymbol{\mu}\otimes\boldsymbol{\mu}) \\ &\quad +(\boldsymbol{A^2}\otimes\boldsymbol{I})[vec(\boldsymbol{C}^T)\otimes\boldsymbol{\mu}]+(\boldsymbol{I}\otimes\boldsymbol{A^2})[\boldsymbol{\mu}\otimes vec(\boldsymbol{C}^T)] \\ &\quad +\boldsymbol{\mu}\otimes\boldsymbol{k}+\boldsymbol{k}\otimes\boldsymbol{\mu}\end{aligned} \tag{4.15}$$

With the first term derived in Equation (4.13) and second term derived in Equation (4.15), we have fully derived Equation (4.7) for the time-evolution of the covariance matrix as

$$\begin{aligned}\frac{dvec(\boldsymbol{C}^T)}{dt} &= E\left(\frac{d\boldsymbol{x}\otimes\boldsymbol{x}}{dt}\right)-\frac{d\boldsymbol{\mu}\otimes\boldsymbol{\mu}}{dt} \\ &= (\boldsymbol{A^1}\otimes\boldsymbol{I}+\boldsymbol{I}\otimes\boldsymbol{A^1})vec(\boldsymbol{C}^T) \\ &\quad +(\boldsymbol{A^2}\otimes\boldsymbol{I})[\boldsymbol{\mu}\otimes vec(\boldsymbol{C}^T)+vec(\boldsymbol{\mu}\otimes\boldsymbol{C}^T)] \\ &\quad +(\boldsymbol{I}\otimes\boldsymbol{A^2})[vec(\boldsymbol{C})\otimes\boldsymbol{\mu}+vec(\boldsymbol{\mu}\otimes\boldsymbol{C}^T)] \\ &\quad +(\boldsymbol{A^2}\otimes\boldsymbol{I}+\boldsymbol{I}\otimes\boldsymbol{A^2})E(\boldsymbol{\delta}\otimes\boldsymbol{\delta}\otimes\boldsymbol{\delta})\end{aligned} \tag{4.16}$$

Note that the variables in ODE for $vec(\boldsymbol{C}^T)$ include only $\boldsymbol{\mu}$ and $vec(\boldsymbol{C}^T)$ except $E(\boldsymbol{\delta}\otimes\boldsymbol{\delta}\otimes\boldsymbol{\delta})$. The term $E(\boldsymbol{\delta}\otimes\boldsymbol{\delta}\otimes\boldsymbol{\delta})$ has the same coefficent matrix as $\boldsymbol{\mu}\otimes vec(\boldsymbol{C}^T)$, $vec(\boldsymbol{C}^T)\otimes\boldsymbol{\mu}$ and $vec(\boldsymbol{\mu}\otimes\boldsymbol{C}^T)$. As $E(\boldsymbol{\delta}\otimes\boldsymbol{\delta}\otimes\boldsymbol{\delta})$ is significantly smaller than $\boldsymbol{\mu}\otimes vec(\boldsymbol{C}^T)$, $vec(\boldsymbol{C})\otimes\boldsymbol{\mu}$ and $vec(\boldsymbol{\mu}\otimes\boldsymbol{C}^T)$ in most cases, we ignore the third moment term $E(\boldsymbol{\delta}\otimes\boldsymbol{\delta}\otimes\boldsymbol{\delta})$ to approximate $\frac{dvec(\boldsymbol{C}^T)}{dt}$. By ignoring the third moment, $\frac{d\boldsymbol{\mu}}{dt}$ and $\frac{dvec(\boldsymbol{C}^T)}{dt}$ as a combined ODE system can be sloved. Thus, the time-evolution of the population mean of each species can be approximated by the new population ODE system as in Equation (4.17).

$$\begin{cases} \dfrac{d\boldsymbol{\mu}}{dt} = \boldsymbol{A^1}\boldsymbol{\mu} + \boldsymbol{A^2}\boldsymbol{\mu}\otimes\boldsymbol{\mu} + \boldsymbol{A^2}vec(\boldsymbol{C}^T) \\ \dfrac{dvec(\boldsymbol{C}^T)}{dt} = (\boldsymbol{A^1}\otimes\boldsymbol{I} + \boldsymbol{I}\otimes\boldsymbol{A^1})vec(\boldsymbol{C}^T) \\ \qquad\qquad +(\boldsymbol{A^2}\otimes\boldsymbol{I})[\boldsymbol{\mu}\otimes vec(\boldsymbol{C}^T) + vec(\boldsymbol{\mu}\otimes\boldsymbol{C}^T)] \\ \qquad\qquad +(\boldsymbol{I}\otimes\boldsymbol{A^2})[vec(\boldsymbol{C}^T)\otimes\boldsymbol{\mu} + vec(\boldsymbol{\mu}\otimes\boldsymbol{C}^T)] \end{cases} \tag{4.17}$$

This population ODE system provides us a faster way to estimate the population mean than the Monte-Carlo method. With the population ODE, we only need to simulate a larger system (n^2+n number of species, n is the number of species in the original system) once to estimate the population mean $\boldsymbol{\mu}(t)$. This population ODE system also estimates the covariance matrix as a function of time $\boldsymbol{C}^T(t)$. It not only makes the simulation more efficient, but also allows us to apply methods for ODEs such as parameter estimation and sensitivity analysis for the population behavior.

4.3.1.3 Derivation of the Jacobian matrix of the population ODEs

The Jacobian matrix of the population ODEs has an analytic solution. So we can derive the Jacobian matrix explicitly to allow faster ODE simulation.

The population ODEs in Equation (4.17) can be written in 2 blocks.

$$\boldsymbol{F}(t,\boldsymbol{x}) = \begin{pmatrix} \boldsymbol{F_\mu} \\ \boldsymbol{F_C} \end{pmatrix} = \begin{pmatrix} \dfrac{d\boldsymbol{\mu}}{dt} \\ \dfrac{dvec(\boldsymbol{C}^T)}{dt} \end{pmatrix}, \quad \boldsymbol{x} = \begin{pmatrix} \boldsymbol{\mu} \\ vec(\boldsymbol{C}^T) \end{pmatrix} \tag{4.18}$$

Therefore, the Jacobian matrix can also be writtien in 4 blocks as in Equation (4.19), and each block can be derived individually.

$$\frac{\partial \boldsymbol{F}(t,\boldsymbol{x})}{\partial \boldsymbol{x}} = \begin{pmatrix} \dfrac{\partial \boldsymbol{F}_{\boldsymbol{\mu}}}{\partial \boldsymbol{\mu}}_{n\times n} & \dfrac{\partial \boldsymbol{F}_{\boldsymbol{\mu}}}{\partial vec(\boldsymbol{C}^T)}_{n\times n^2} \\ \dfrac{\partial \boldsymbol{F}_{\boldsymbol{C}}}{\partial \boldsymbol{\mu}}_{n^2\times n} & \dfrac{\partial \boldsymbol{F}_{\boldsymbol{C}}}{\partial vec(\boldsymbol{C}^T)}_{n^2\times n^2} \end{pmatrix}_{(n^2+n)\times(n^2+n)} \tag{4.19}$$

Each block in the Jacobian matrix is derived as below. For detailed derivation, please refer to the Appendix.

$$\frac{\partial \boldsymbol{F}_{\boldsymbol{\mu}}}{\partial \boldsymbol{\mu}} = \boldsymbol{A}^{\boldsymbol{1}} + \boldsymbol{A}^{\boldsymbol{2}}(\boldsymbol{\mu}\otimes\boldsymbol{I} + \boldsymbol{I}\otimes\boldsymbol{\mu}) \tag{4.20}$$

$$\frac{\partial \boldsymbol{F}_{\boldsymbol{\mu}}}{\partial vec(\boldsymbol{C}^T)} = \boldsymbol{A}^{\boldsymbol{2}} \tag{4.21}$$

$$\begin{aligned} \frac{\partial \boldsymbol{F}_{\boldsymbol{C}}}{\partial \boldsymbol{\mu}} &= (\boldsymbol{A}^{\boldsymbol{2}}\otimes\boldsymbol{I})[\boldsymbol{I}\otimes vec(\boldsymbol{C}^T) + E(\boldsymbol{\delta}\otimes\boldsymbol{I}\otimes\boldsymbol{\delta})] \\ &\quad +(\boldsymbol{I}\otimes\boldsymbol{A}^{\boldsymbol{2}})[E(\boldsymbol{\delta}\otimes\boldsymbol{I}\otimes\boldsymbol{\delta}) + vec(\boldsymbol{C}^T)\otimes\boldsymbol{I}] \end{aligned} \tag{4.22}$$

$$\begin{aligned} \frac{\partial \boldsymbol{F}_{\boldsymbol{C}}}{\partial vec(\boldsymbol{C}^T)} &= (\boldsymbol{A}^{1}\otimes\boldsymbol{I} + \boldsymbol{I}\otimes\boldsymbol{A}^{1}) \\ &\quad +(\boldsymbol{A}^{\boldsymbol{2}}\otimes\boldsymbol{I})(\boldsymbol{\mu}\otimes\boldsymbol{I}\otimes\boldsymbol{I} + \boldsymbol{I}\otimes\boldsymbol{\mu}\otimes\boldsymbol{I}) \\ &\quad +(\boldsymbol{I}\otimes\boldsymbol{A}^{\boldsymbol{2}})(\boldsymbol{I}\otimes\boldsymbol{\mu}\otimes\boldsymbol{I} + \boldsymbol{I}\otimes\boldsymbol{I}\otimes\boldsymbol{\mu}) \end{aligned} \tag{4.23}$$

Please note that some matrices in the four equations above are even larger than the Jacobian matrix itself. For example, the size of $\boldsymbol{A}^{\boldsymbol{2}}\otimes\boldsymbol{I}$ is $n^2\times n^3$. This would take a lot of memory if we compute the Jacobian matrix based on the above four equations. Since we only need the result of the Jacobian matrix but not the intermeidate terms such as $\boldsymbol{A}^{\boldsymbol{2}}\otimes\boldsymbol{I}$, we tried to faciliate calculation of each block of the Jacobian matrix. Actually, after we looked into the details of the Kronecker product and matrix product opertations in Equation (4.22) and (4.23), we found that these equations can be simplified in terms of matrix operations. Simplifications

of Equation (4.22) and (4.23) are shown below. Please refer to the detailed derivation in the Appendix.

For Equation (4.22), we need to write $\boldsymbol{A^2}$ as a block matrix

$$\boldsymbol{A^2} = \begin{pmatrix} \boldsymbol{B}_1 & \cdots & \boldsymbol{B}_n \end{pmatrix}_{n\times n^2}, \quad \boldsymbol{B}_k = \begin{pmatrix} \boldsymbol{A^2}_{1,(k-1)n+1} & \cdots & \boldsymbol{A^2}_{1,kn} \\ \vdots & \ddots & \vdots \\ \boldsymbol{A^2}_{n,(k-1)n+1} & \cdots & \boldsymbol{A^2}_{n,kn} \end{pmatrix}_{n\times n} \tag{4.24}$$

and to write $\boldsymbol{C}^* = \boldsymbol{C} + \boldsymbol{C}^T$ as a block matrix as well

$$\boldsymbol{C}^* = \begin{pmatrix} \boldsymbol{c}_1 & \cdots & \boldsymbol{c}_n \end{pmatrix}_{n\times n}, \quad \boldsymbol{c}_i = \begin{pmatrix} \boldsymbol{C}^*_{1,1} \\ \vdots \\ \boldsymbol{C}^*_{1,n} \end{pmatrix}_{n\times 1} \tag{4.25}$$

Then, we can write Equation (4.22) as

$$\frac{\partial \boldsymbol{F}_C}{\partial \boldsymbol{\mu}} = \boldsymbol{T^1} + [\boldsymbol{A^2} vec(\boldsymbol{C})] \otimes \boldsymbol{I} + \boldsymbol{T^3} \tag{4.26}$$

where the k-th column of $\boldsymbol{T^1}$ is

$$\boldsymbol{T^1}_{:,k} = vec(\boldsymbol{C}^T \boldsymbol{B}_k^T) \tag{4.27}$$

and the k-th row of $\boldsymbol{T^3}$ is

$$\boldsymbol{T^3}_{k,:} = \boldsymbol{A^2}(\boldsymbol{c}_k \otimes \boldsymbol{I}) \tag{4.28}$$

For Equation (4.23), after simplification, we found that it can be calculated using $\frac{\partial \boldsymbol{F}_{\boldsymbol{\mu}}}{\partial \boldsymbol{\mu}}$, which we have evaluated in Equation (4.20).

$$\frac{\partial \boldsymbol{F}_C}{\partial vec(\boldsymbol{C}^T)} = \frac{\partial \boldsymbol{F}_\mu}{\partial \boldsymbol{\mu}} \otimes \boldsymbol{I} + \boldsymbol{I} \otimes \frac{\partial \boldsymbol{F}_\mu}{\partial \boldsymbol{\mu}} \tag{4.29}$$

Hence, we have simplified the calculation of the Jacobian matrix. The largest matrix required for the calculation of the Jacobian matrix has size $n \times n^2$, smaller than $n^2 \times n^3$ before simplification. Some unnecessary calculations are also avoided such as that in Equation (4.23). We can use the result of (4.20) to make the calculation of Equation (4.23) almost trivial as derived in Equation (4.29).

4.3.2 Case Study Using Population ODE System

After derivation of the population ODE system, we wanted to test the performance of this approximation approach in both speed and accuracy. Since we did not know the truth of cell-population dynamics, we compared our simulation results using population ODEs to the results from Monte-Carlo simulation with large sample size. The convergence plot for Monte-Carlo simulation was plotted to show the sample size we selected

4.3.2.1 Applying Population ODE to EGFR Pathway

EGFR (Epidermal Growth Factor Receptor) pathway is one of the most studied signaling pathways both biologically and computationally as its important function in regulating cell division, motility and apoptosis (Citri and Yarden, 2006). Because of the importance and extensive investigation, the studies of EGFR pathway have also been most widely transferred to biomedical research (Citri and Yarden, 2006). Besides its classical role in the history of signaling pathway studies,

cell-to-cell variability has also been found in EGFR pathway. Thus, we chose EGFR pathway to be our first attempt of the Population ODE.

There are dozens of models about EGFR pathway published. The earliest models studied ligand-receptor binding and receptor trafficking (Wiley and Cunningham, 1981). Then, Kholodenko *et al.* built the first model including the early target proteins in the signaling cascade, such as Grb2, Shc and SOS (Kholodenko et al., 1999). Schoeberl *et al.* added more downstream events such as Ras-dependent MAPK cascade based on Kholodenko's model (Schoeberl et al., 2002). These two models then served as platforms for more complex EGFR pathway models. Recent models include a model expanding the EGF receptor to ErbB receptor family (Chen et al., 2009), a model focusing on the ligand-specific control of the dynamics of ErbB network (Nakakuki et al., 2010), and models which have crosstalk with other pathways (Sivakumar et al., 2011). As the recent models become very large and sometimes case-specific, we chose to apply the Population ODE to Schoeberl's model (Schoeberl et al., 2002), which serves as a backbone for most of the later models.

Schoeberl's model has 29 species and 10 species out of 29 have non-zero initial concentrations. We assume that the EGF ligand outside the cell has no cell-to-cell variability. As we do not know the distribution of the concentration of the other 9 species in a population of cells, we assume the concentration of the other 9 species are normally distributed with the variance of 20% of its initial concentration. This assumption allows significant variations among different cells and also keeps only about 0.000003% concentration to be negative, which we can simply ignore. With

such assumption, we can first do a Monte-Carlo simulation to approximate the population mean over time and also check the rate of convergence using this method.

Sampled single cell simulations are plotted (Figure 4.1A). The variation among different cells could be very large. There are many different criteria to check the convergence of Monte Carlo simulation and the choice of the criterion is often context dependent. In our case, we plotted the standard error of mean (SEM) of the area under the Monte Carlo simulation trajectory (Figure 4.1B). The standard error of mean was calculated using bootstrap with 1000 sampling. As shown in Figure 4.1B, the SEM decreases with increasing sample size in Monte Carlo simulation. This means that when the sample size becomes larger, the population mean computed using Monte Carlo simulation is less variable. However, we cannot increase the sample size to infinity. To check if the Monte Carlo simulation is converged in our case, we used the criterion that the slope of the SEM curve was less than 10^{-6}. Because the SEM curve is fluctuating, we compute the slope at a specific sample size with smoothing as in Equation (4.30). In Equation (4.30), N is the sample size of a Monte Carlo simulation, k is the step size when we increase the sample size, and x is the index of the point where the slope is calculated. We highlighted the first converged point in Figure 4.1B with a red circle. Later on, we use this converged Monte Carlo simulation as a reference of the population simulation (also in Figure 4.1A).

$$slope_{N=kx} = \frac{\frac{1}{10}\sum_{i=k(x-10)}^{k(x-1)} SEM_{N=i} - SEM_{N=kx}}{k} \tag{4.30}$$

Then, we compare the converged Monte Carlo simulation with the single cell simulation in Figure 4.1C. The single cell simulation was simulated using the initial concentrations as the expected value of the initial concentrations from a population of cells. Figure 4.1C shows a significant difference between the single cell and cell population dynamics. Can our Population ODE approximate the cell population behavior better? We then plotted the converged Monte Carlo simulation together with the Population ODE simulation in Figure 4.1D. Although the Population ODE did not match the Monte Carlo simulation perfectly, it did improve significantly from the single cell simulation.

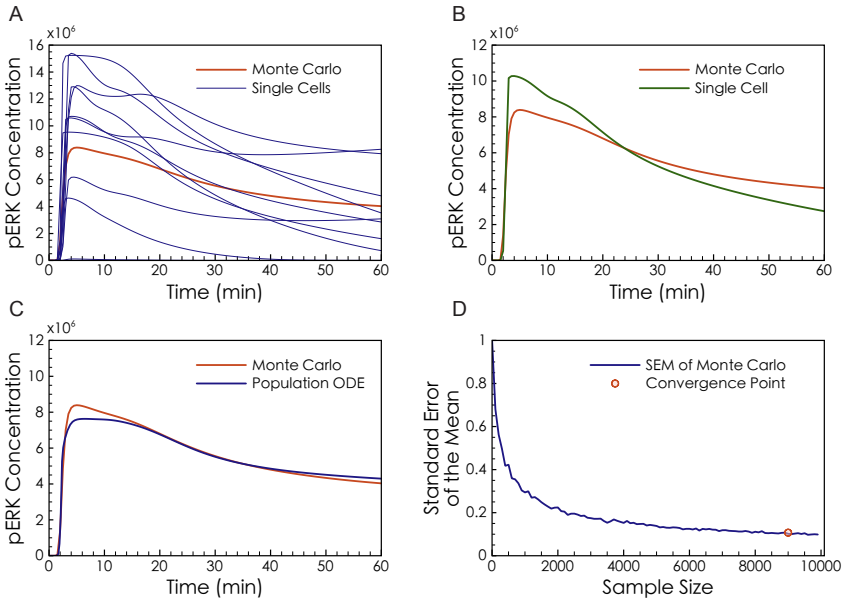

Figure 4.1 Applying Population ODE to EGFR Pathway. (A) 10 random samples of single cell simulation (blue curves) versus converged Monte Carlo simulation (red curve). (B) Convergence of Monte Carlo simulation. (C) Single cell simulation with initial concentrations equal to their expected values (green curve) versus converged Monte Carlo simulation (red curve). (D) Simulation of Population ODE (blue curve) versus Monte Carlo simulation (red curve).

4.3.2.2 Applying Population ODE to NFκB Pathway

NFκB (Nuclear Factor κ-light-chain-enhancer of activated B cells) is a family of transcription factors which regulate a variety of genes involved in cell division, apoptosis and inflammation (Hoffmann, 2002). Because of its importance in innate immune response, it is considered a potential drug target for chronic inflammatory diseases (Hoffmann, 2002). Dynamic response is important for drug development and systems biology tools such as computational modeling have been used to study NFκB pathway (Nelson, 2004). This pathway was found to have an identical behavior, which is dampened oscillation. It was also found that the oscillation is greatly affected by the cell-to-cell variability (Lee and Covert, 2010). Single-cell measurements and modeling of the variations among different cells were used to fill in the gap of cell-to-cell variability in NFκB pathway (Ashall et al., 2009, Lee et al., 2009). Thus, we find this is a good case for us to apply the Population ODE to see if it can approximate the population behavior of an oscillating system.

The first computational model for studying NFκB pathway was built to study the response of this pathway to TNF-α ligand (Hoffmann, 2002). The following work has added new components (Nelson, 2004) based on Hoffmann's Model and has also modeled the response to other ligand (Lee et al., 2009). Furthermore, computational modeling studies have also investigated single-cell dynamics in NFκB pathway. Nelson *et al.* first attempted to use single-cell time-lapse imaging combined with single-cell model to analyze the parameters that affect the oscillation of NFκB localization (Nelson, 2004). Later models were not only compared with single-cell experimental data but also utilized stochastic methods to

simulate population behaviors (Lee et al., 2009). These models showed significant heterogeneity among a population of cells. A more recent model of NFκB pathway emphasized the difference between single-cell and cell-population dynamics based on both experimental and computational results (Ashall et al., 2009).

Models of NFκB pathway exhibit many successful examples of computational methods in studying the dynamics of signaling pathways. There are also extensive experimental results confirming that the difference between single-cell and cell-population behaviors is significant. The importance of both computational modeling and cell-to-cell variability leads us to apply our Population ODE to this pathway. Unfortunately, many recent models of NFκB pathway did not use Mass Action Kinetics to model all reactions. Thus, we apply our Population ODE to the basis of NFκB pathway models (Hoffmann, 2002), in which all reactions are ruled by the Mass Action Kinetics.

Sampled single cell simulations are plotted (Figure 4.2A). Although individual cells are still oscillating at later time points, their phase becomes different. Therefore, averaged molecule oscillation is much more dampened than the molecule oscillation in a single cell. As shown by (Hoffmann, 2002), some parameter could affect the duration of oscillation. Thus, comparing single cell dynamics to cell population measurements could lead to incorrect estimation of certain parameter. In the case of NFκB pathway, we use the same criterion as that used in EGFR pathway to identify the converged Monte Carlo simulation (Figure 4.2B). Comparison between the single cell simulation and converged Monte Carlo simulation shows a significant difference of behavior (Figure 4.2C), especially the

magnitude of oscillations at later time points. This can be considered as a qualitative difference and it is important to have a population model which can be compared to population behavior. Our Population ODE also approximates the population dynamics better than single cell simulation (Figure 4.2D).

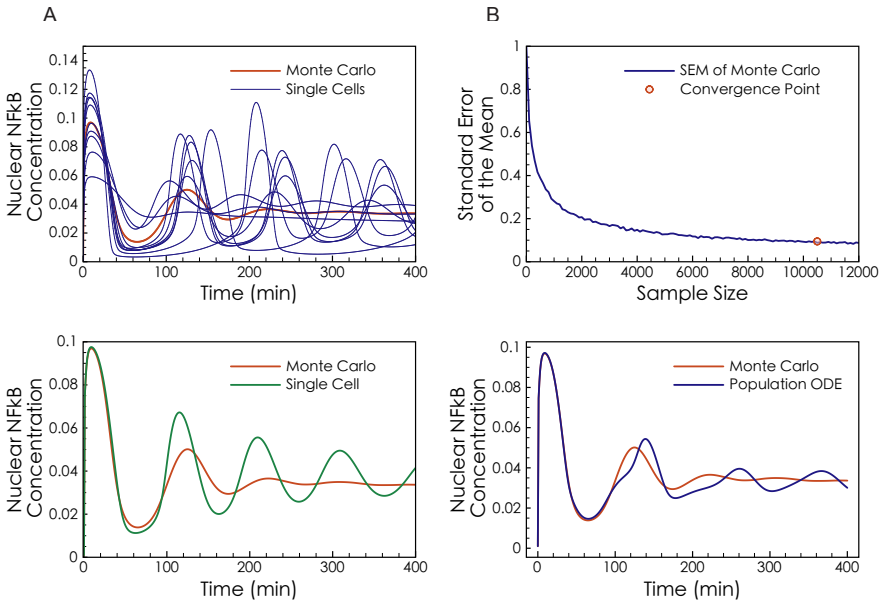

Figure 4.2 Applying Population ODE to NFκB Pathway. (A) 10 random samples of single cell simulation (blue curves) versus converged Monte Carlo simulation (red curve). (B) Convergence of Monte Carlo simulation. (C) Single cell simulation with initial concentrations equal to their expected values (green curve) versus converged Monte Carlo simulation (red curve). (D) Simulation of Population ODE (blue curve) versus Monte Carlo simulation (red curve).

4.3.2.3 Applying Population ODE to Intrinsic Apoptosis Pathway

Apoptosis is an important process in developmental biology. Researchers also try to take advantage of triggering the apoptosis signal to kill disease related cells such as cancer cells. Therefore, better understanding of the mechanism of apoptosis would lead us to better drug for developmental disease or cancer.

Apoptosis pathway is one of the earliest pathways that were found to have different behaviors between single cell and cell population. One of the reasons is that the outcome of this pathway is cell death. It is often found in a population of cells that a portion of cells went apoptosis after triggering apoptosis pathway. This leads researchers to use single cell data for apoptosis pathway studies and to unravel the cell-to-cell variability. Spencer *et al.* have studied non-genetic origins of cell-to-cell variability in TRAIL-induced apoptosis (Spencer et al., 2009b). They claim "naturally occurring differences in the levels of states of proteins regulating receptor-mediated apoptosis are the primary causes of cell-to-cell variability in the timing and probability of death in human cell lines". This supports our assumption of different initial concentrations in the way that different initial concentrations could be one of the most important factors of cell-to-cell variability.

Mathematical models have also been built to understand how analog extrinsic signals (concentration of stimulus) could lead to digital cell decisions (live or die) (Albeck et al., 2008). Here we chose to apply our Population ODE to Eissing's model (Eissing, 2004). This model has the main backbone of the caspase cascade in apoptosis pathway and it exhibits a typical bistable behavior, which is often seen in biological network. Thus, it could be a representative of a class of pathways that are bistable. These bistable systems are also often much more non-linear than other types of systems. We also want to test our Population ODE method in more extreme cases such as the bistable apoptosis pathway.

Sampled single-cell simulations are shown in Figure 4.3A. In bistable system, we usually observe a “switch-like” behavior, which means the species concentration

switch from one steady state to the other within a very short time. As in Figure 4.3A, different initial concentrations led to different time of switching but not the final steady state of activated caspase 3. Figure 4.3A also shows the population mean of activated caspase 3 from Monte Carlo simulation. This population behavior is dramatically different from any of the single-cell behaviors. We also did convergence study of Monte Carlo simulation (Figure 4.3B). Figure 4.3C shows the difference between single-cell and Monte Carlo simulations. This shows bistable systems are extreme cases in which bulk experiments can hardly be used to build single-cell models.

However, our Population ODE does not predict the population behavior accurately enough in this particular case Figure 4.3D. This leads us to develop another method (Sample Reduction) to simulate the population behavior more efficiently. We will discuss our Sample Reduction method in the next section.

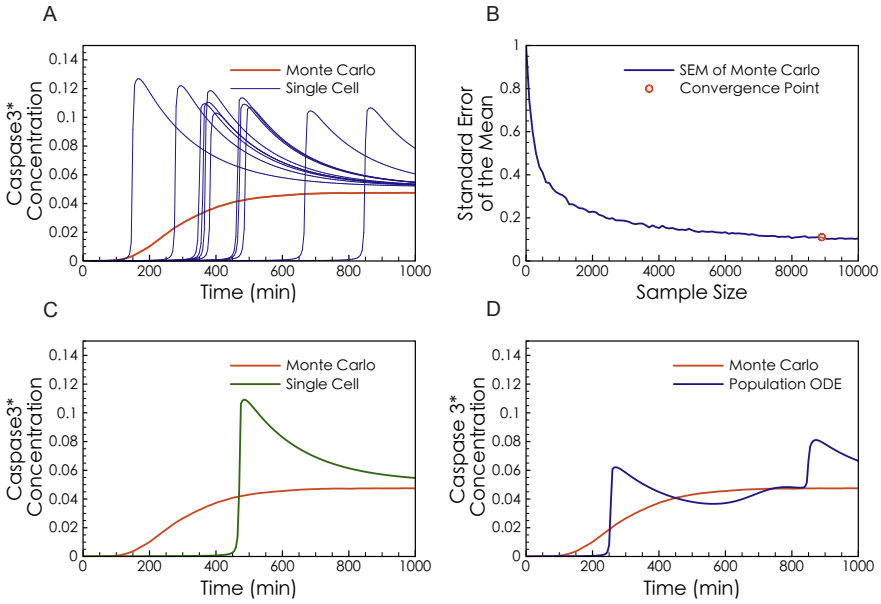

Figure 4.3 Applying Population ODE to Intrinsic Apoptosis Pathway. (A) 10 random samples of single cell simulation (blue curves) versus converged Monte Carlo simulation (red curve). (B) Convergence of Monte Carlo simulation. (C) Single cell simulation with initial concentrations equal to their expected values (green curve) versus converged Monte Carlo simulation (red curve). (D) Simulation of Population ODE (blue curve) versus Monte Carlo simulation (red curve).

4.3.3 Sample Reduction Based on Singular Value Decomposition of the Special Sensitivity Matrix

4.3.3.1 Singular Value Decomposition (SVD) of the Special Sensitivity Matrix to Reduce Sampling Space

As shown in the previous section, Population ODE does not work well in some cases, such as bistable systems. Other types of complex systems besides mono-stable, oscillatory, and bistable systems could also exist even if we have not discovered any. We therefore seek to develop more general methods to facilitate the simulation of population behavior.

The dimension of biological systems is often large. This makes the sampling space of the initial concentrations large and the sample density decreases exponentially as the dimension of the sampling space increases. Moreover, in biological systems we often have very few outputs to focus. If we consider the initial concentrations as the input, the system then has a very large input space and a very small output space (one dimension in most cases as we can simulate one output at a time). Although Monte-Carlo method implicitly projects the input space to the output space without the knowledge of their relationship, we might be able to improve the simulation efficiency by analyzing the relationship between the input space and output space. To analyze this relationship is a possible task

because the relationship between the input space and output space in embedded in the ODE system.

In our study, we utilized the sensitivity of all initial concentrations to the output species concentration at different time points. The sensitivity matrix $\boldsymbol{S}$ was calculated as in Equation (4.31). This sensitivity matrix provides us the information of how the change in the initial concentrations would affect the output dynamics. Then, by taking the Singular Value Decomposition (SVD) of this particular sensitivity matrix, we could get the most important directions in the sampling space of initial concentrations that affects the output.

$$\boldsymbol{S} = \begin{pmatrix} \left.\frac{dy}{d\boldsymbol{x}}\right|_{t=0} & \cdots & \left.\frac{dy}{d\boldsymbol{x}}\right|_{t=t_i} & \cdots & \left.\frac{dy}{d\boldsymbol{x}}\right|_{t=t_n} \end{pmatrix}$$

$$\left.\frac{dy}{d\boldsymbol{x}}\right|_{t=t_i} = \begin{pmatrix} \left.\frac{dy}{dx_1}\right|_{t=t_i} \\ \vdots \\ \left.\frac{dy}{dx_n}\right|_{t=t_i} \end{pmatrix} \tag{4.31}$$

$$\boldsymbol{S} = \boldsymbol{U}\boldsymbol{\Sigma}\boldsymbol{V} = \begin{bmatrix} \boldsymbol{u_1} & \boldsymbol{u_2} & \cdots & \boldsymbol{u_n} \end{bmatrix} \begin{bmatrix} \sigma_1 & 0 & \cdots & 0 \\ 0 & \sigma_2 & \cdots & 0 \\ \vdots & \vdots & \ddots & \vdots \\ 0 & 0 & \cdots & \sigma_n \end{bmatrix} \begin{bmatrix} \boldsymbol{v}_1^T \\ \boldsymbol{v}_2^T \\ \vdots \\ \boldsymbol{v}_n^T \end{bmatrix} \tag{4.32}$$

$$= \sum_{i=1}^{n} \sigma_i \boldsymbol{u}_i \boldsymbol{v}_i^T$$

The SVD of the sensitivity matrix $\boldsymbol{S}$ is shown in Equation (4.32). One of the most important applications of SVD is matrix approximation. We approximate the sensitivity matrix $\boldsymbol{S}$ by ignoring small singular value and their associated singular vectors. We chose to keep the large singular values of which the summation is

larger than 90% of the summation of all singular values. In such a case, the approximated sensitivity matrix $\tilde{\boldsymbol{S}}$ is written as that in Equation (4.33), in which l is the number of large singular values we keep.

$$\tilde{\boldsymbol{S}} = \sum_{i=1}^{l} \sigma_i \boldsymbol{u}_i \boldsymbol{v}_i^T \tag{4.33}$$

Then, we approximate the difference of the output $\widetilde{\Delta y}$ to be

$$\widetilde{\Delta y} = \tilde{\boldsymbol{S}} \Delta \boldsymbol{x}_0 = \sum_{i=1}^{l} \sigma_i \boldsymbol{u}_i \boldsymbol{v}_i^T \Delta \boldsymbol{x}_0 = \sum_{i=1}^{l} \sigma_i \boldsymbol{u}_i \Delta \boldsymbol{x}_0' \qquad (\Delta \boldsymbol{x}_0' = \boldsymbol{v}_i^T \Delta \boldsymbol{x}_0) \tag{4.34}$$

We can infer from Equation (4.34) that the difference of output value is approximately due to the difference of $\Delta \boldsymbol{x}_0'$. Note that the dimension of $\Delta \boldsymbol{x}_0$ is $n \times 1$ and the dimension of $\Delta \boldsymbol{x}_0'$ is $l \times 1$. We then can interpret $\Delta \boldsymbol{x}_0'$ as variations of initial concentrations in a reduced space (l-dimension), which spanned by orthogonal vectors $\boldsymbol{v}_1, \boldsymbol{v}_2, \cdots, \boldsymbol{v}_l$. When we observe a single output, l is usually much smaller than n. Thus, we can reduce the sampling space of initial concentrations from n-dimension to l-dimension and approximate the variations of the output. However, random sampling in the reduced sampling space does not reduce the sample size significantly. As the reduced space often has extremely small dimension (less than 3), we try to use orthogonal sampling in the reduced sampling space.

4.3.3.2 Orthogonal Sampling in the Reduced Space of Initial Concentrations

In typical orthogonal sampling, the sampling space is divided into equally probable subspaces. Then all subspaces are sampled once and the population mean is estimated by the sample average. In our case, we used a slightly different

orthogonal sampling strategy. We divided the sampling space into subspaces with equal sizes (not equal probabilities) and then the population mean equals a weighted sum of the samples in all subspaces. The weight for each sample is equal to the cumulative probability of the subspace it is sampled from. This modified orthogonal sampling covers the sampling space evenly. In bistable systems, the larger the variations of initial concentrations are, the larger the difference between single cell and cell population is. Therefore, it is better to make all subspaces have similar variations of initial concentrations when we use only one sample to represent a subspace in orthogonal sampling. This is done by making the sizes of subspaces identical.

As the reduced sampling space is spanned by orthogonal vectors ($\boldsymbol{v}_1, \boldsymbol{v}_2, \cdots, \boldsymbol{v}_l$), the cumulative probability in a hypercube subspace can be calculated as below in Equation (4.35). We previously assumed the initial concentrations of all species follow a multivariate Gaussian distribution with expected value $\boldsymbol{\mu}_0$ and covariance matrix $\boldsymbol{C}_0$. We also assumed that each species is independent of others. Thus, the initial covariance matrix $\boldsymbol{C}_0$ has only non-zero values on its diagonal. Assuming the starting and end points of a hypercube in direction $\boldsymbol{v}_i$ are p_i and p_i', the cumulative probability in such a hypercube is

$$P_{hypercube} = F_{mvncdf}(\boldsymbol{p}', \boldsymbol{\mu}_0', \boldsymbol{C}_0') - F_{mvncdf}(\boldsymbol{p}, \boldsymbol{\mu}_0', \boldsymbol{C}_0') \tag{4.35}$$

in which

$$\boldsymbol{p} = \begin{pmatrix} p_1 \\ \vdots \\ p_l \end{pmatrix}, \quad \boldsymbol{p}' = \begin{pmatrix} p_1' \\ \vdots \\ p_l' \end{pmatrix} \tag{4.36}$$

and $\boldsymbol{\mu}_0'$ and $\boldsymbol{C}_0'$ are projected expected values and covariance matrix in the reduced space calculated as

$$\begin{aligned}\boldsymbol{\mu}_0' &= \left(\begin{bmatrix} \boldsymbol{v}_1^T \\ \vdots \\ \boldsymbol{v}_l^T \end{bmatrix}_{l\times n} \right) \boldsymbol{\mu}_0 = \begin{bmatrix} \boldsymbol{v}_1 \bullet \boldsymbol{\mu}_0 \\ \vdots \\ \boldsymbol{v}_l \bullet \boldsymbol{\mu}_0 \end{bmatrix}_{l\times 1} \\ \boldsymbol{C}_0' &= \begin{bmatrix} \boldsymbol{v}_1^T \\ \vdots \\ \boldsymbol{v}_l^T \end{bmatrix} \boldsymbol{C}_0 \begin{bmatrix} \boldsymbol{v}_1 & \cdots & \boldsymbol{v}_l \end{bmatrix}\end{aligned} \tag{4.37}$$

Note that the projected covariance matrix $\boldsymbol{C}_0'$ has non-zero off-diagonal elements. Therefore, projected/linear combinations of initial concentrations are not independent any more.

With the cumulative probability of each subspace, we are able to estimate the population mean of the output by a weighted sum of all samples as

$$\overline{y}(t) = \sum_{i=1}^{N_{sub}} P_{hypercube(i)} y_{hypercube(i)}(t) \tag{4.38}$$

The weights are the cumulative probabilities $P_{hypercube(i)}$ of subspaces and the number of subspace N_{sub} is pre-defined. One sample is taken from the center of a subspace as the representative of the subspace (Figure 4.4).

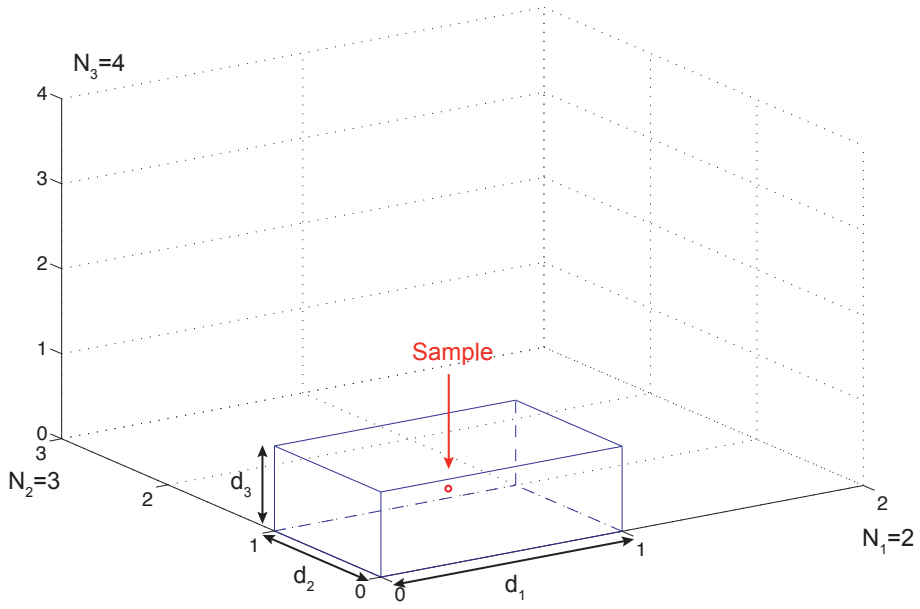

Figure 4.4 Orthogonal Sampling. The whole sampling space is divided into subspaces with uniform size (blue cuboid). The number of grid spaces in all directions are N_1=2, N_2=3, and N_3=4. One sample (center of the subspace, red sphere) is taken from one subspace.

Hypercubes of subspaces are sliced by grid lines in the reduced space (Figure 4.4). Since different directions in the reduced space have different significance according to their corresponding singular values, the number of grid spaces on each direction is determined by the corresponding singular value. We set the relationship between number of grid spaces and singluar value to be

$$\frac{N_1}{\sigma_1} = \frac{N_2}{\sigma_2} = \cdots = \frac{N_l}{\sigma_l} \tag{4.39}$$

Obviously, the total number of subspaces $N_{sub} = \prod_{i=1}^{l} N_i$. Therefore, when N_{sub} is defined, $N_1,\ldots,N_l$ can be solved. Sometimes the ratio between two singular values can be large but N_{sub} is not large. In such cases, some N_i may be smaller

than 1 and we simply ignore those directions and further reduce the dimension of the sampling space.

4.3.4 Case Study Using Sample Reduction

4.3.4.1 Applying Sample Reduction to Intrinsic Apoptosis Pathway

As shown in Section 4.3.2.3 (Figure 4.3D), Population ODEs failed to approximate the mean of activated caspase 3. We then apply our Sample Reduction method to this case. Firstly, we need to compute the special sensitivity matrix and its singular value decompostion (SVD) described above. We used 20 time points for the special sensitivity matrix and the singular values of this matrix is shown in Figure 4.5A. There were 5 species with non-zero initial concentrations in this pathway. All the 5 orthogonal vectors ($\boldsymbol{v}_1,\ldots,\boldsymbol{v}_5$) computed from SVD spanned the whole sampling spaces of initial concentrations. According to their corresponding singular values, the first orthogonal vector pointed the most important direction in the sampling space. Since the first singular value was already more than 90% of the sum of all singular values, we reduce the sampling space to a 1-dimentional reduced space, spanned by $\boldsymbol{v}_1$. Orthogonal sampling described in Section 4.3.3.2 was used and the averaged concentration of activated caspase 3 ($\overline{y}(t)$). To compare Sample Reduction and Monte Carlo simulation, we computed the normalized integrated squared error (ISE) using both methods to our reference (converged Monte Carlo simulation, $y_{ref}(t)$). The ISE is defined as in Equation (4.40) and solved numerically. As orthorgonal sampling is not random, the ISE using Sample Reduction is deterministic. However, Monte Carlo simulation uses random sampling.

To have a better approximation of the ISE, we again used bootstrap sampling (bootstrap sample size Ns=1000) to calculate the convergence of averge ISE in Monte Carlo simulation.

$$ISE_{norm} = \sqrt{\frac{\int_0^T [\bar{y}(t) - y_{ref}(t)]^2 \, dt}{\int_0^T y_{ref}(t)^2 \, dt}} \tag{4.40}$$

As shown in Figure 4.5B, when we increaed the sample size, the ISE decreased much faster using our Sample Reduction method than using Monte Carlo simulation. Therefore, much smaller sample size was required in Sample Reduction to achieve the same accuracy. Note that the ISE is larger in Sample Reduction than that in Monte Carlo simulation when the sample size is larger than a threshold. This is because we lost information of the sampling space when we reduce its dimension and there is a limit of reducing ISE in Sample Reduction by increasing the sample size (the limit can be greater than 0). However, smaller limit can be achieved by increasing the dimension of the reduced space.

As biological measurements often have large variations, 10% normalized ISE should be acceptable as a good approximation to the population mean. We therefore compared the results with 10% normalized ISE from Sample Reduction and Monte Carlo simulation to the reference. As shown in Figure 4.5C, Sample Reduction approximated the population mean as good as Monte Carlo simulation (both 10% normalized ISE), but Sample Reduction required much less sample size (N=18) than Monte Carlo simulation (N=82). Another advantage of Sample Reduction method is that it converges much faster than Monte Carlo simulation

and there is no fluctuation of the approximation because orthogonal sampling is not random. Figure 4.5D shows a smooth curve from Sample Reduction and a fluctuant curve from Monte Carlo simulation with the same sample size (N=200). The deterministic nature of our Sample Reduction method can also faciliate all types of model analysis by avoiding further sampling and averaging.

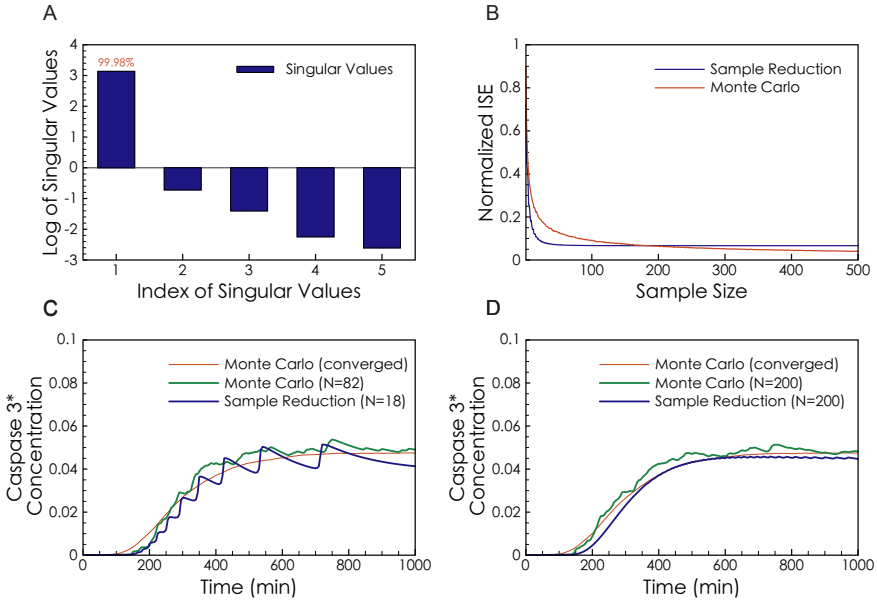

Figure 4.5 Applying sample reduction to intrinsic apoptosis pathway. (A) The singular values from largest to smallest. The red text indicates that the first singular value is 99.98% of the sum of all singular values. (B) Normalized ISE calculated as in Equation (4.40) using Monte Carlo simulation (red curve) and Sample Reduction (blue curve). (C) Monte Carlo simulation (green curve) and Sample Reduction (blue curve) with 10% normalized ISE were compared to the reference (red curve). (D) Monte Carlo simulation (green curve) and Sample Reduction (blue curve) using the same sample size (N=200) were compared to the reference (red curve).

4.3.5 Case Study of TGF-β Network

As mentioned in Chapter 2 (Section 2.2.4), previous work has studied an upstream network of TGF-β (Venkatraman et al., 2012). This network mainly consists of two TGF-β activators: plasmin and TSP1, and the urokinase system for

plasmin activation. Note that TGF-β regulates PAI1 and TSP1 by inducing their gene expression through Smad signaling pathway (Figure 2.3). In Venkatraman's model, the Smad signaling pathway was built as a black box of a single reaction. All species in this network present in the ECM and all reactions take place in the ECM except the Smad signaling. Thus, all species are secreted by a number of cells and their concentrations are averaged from a population of cells. Similar to what we have seen in previous examples of other signaling pathways, TGF-β may also induce different responses of Smad signaling in different cells. The averaged dynamics of PAI1 and TSP1 may be different from the dynamics of these proteins secreted by a single cell. Previous work used a black box for the Smad pathway and assumed all cells are identical. Since the Smad pathway exists in both feedback loops in this network, it is critical for the bistable behavior of the whole system. Therefore, we wanted to study whether the cell-to-cell variability will affect the bistable behavior of this network.

To achieve our goal, we need to integrate our Smad pathway model (Model 11, Section 3.3.10) into the upstream network of TGF-β activation as a replacement of the original black box. We also considered cell-to-cell variability of the outcome of Smad signaling pathway. This actually makes the integration of two systems very difficult as the species in the upstream network are already averaged from a population of cells. Thus, it is an integration of a population level network in the ECM and a population of single cell models inside cells. More importantly, PAI1 and TSP1 are mixed quickly (roughly at each time step of simulation) from secretion of different cells. Although this task may cause a lot of problems for the

sampling based methods such as Monte Carlo simulation, it is ideal to use our Population ODE since the outcome of the Population ODE is averaged dynamics of a population of cells. Thus, the upstream network of TGF-β activation and the Population ODE of Smad signaling pathway can be integrated as a whole ODE system and we analyze this system as the same as other ODE systems. As we have seen in Chapter 3, Smad signaling did not show a bistable behavior. We believe the Population ODE can well approximate its population dynamics.

As same as the previous examples, we assumed that the cell-to-cell variability was only due to different initial concentrations of species. The detailed settings of the integration are described in the Materials and Methods (Section 4.2). In the integrated model, there were two parameters *kp1* and *kp2* of which the meaning had been changed. They previously represented the production rates of TSP1 and PAI1 induced directly by TGF-β in (Venkatraman et al., 2012). In the integrated system, TSP1 and PAI1 expression was not induced by TGF-β but Smad complex in the nucleus, which is the output species of Smad signaling pathway. Therefore, the values of kp1 and kp2 were different in the integrated model. Then, we did the "going-up and coming-down" simulation as in (Venkatraman et al., 2012) regarding the *kp1* and *kp2* parameters. The "going-up and coming-down" simulation was done by initiating the system at a mono-stable steady state (i.e. low value of a certain parameter) and then increasing the parameter and simulate the steady state of TGF-β to get the going-up curve (blue curves, Figure 4.6A-B) until the system becomes mono-stable again. After that, the parameter was decreased and steady state of TGF-β was simulated. As shown in Figure 4.6, there was a range of *kp1*

and a range of *kp2* at which the going-up and coming-down curves did not overlap. Within these ranges, the system had two steady states even if the parameters (*kp1* and *kp2*) were fixed. This means that the integrated system could also be bistable within certain ranges of *kp1* and *kp2*.

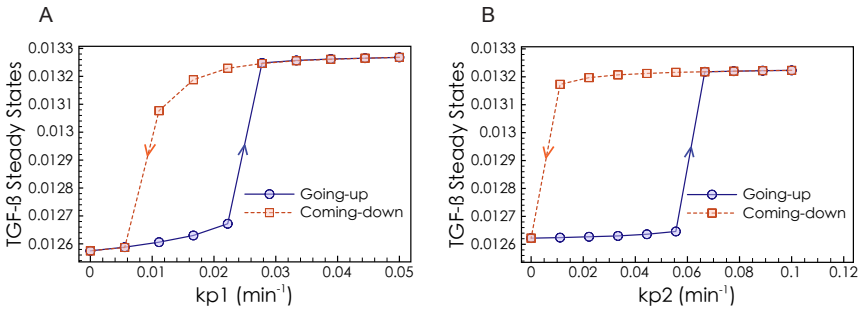

Figure 4.6 Going-up and coming-down simulation of integrated pathway of TGF-β activation and Smad signaling. (A) Simulations with increasing *kp1* from 0 to 0.05 (blue dots) and decreasing *kp1* from 0.05 to 0 (red dots). (B) Simulations with increasing *kp2* from 0 to 0.1 (blue dots) and decreasing *kp2* from 0.1 to 0 (red dots).

4.4 Discussion

In this study, we developed two methods to facilitate model simulation of the dynamical behavior of a population of cells. The first method was a new ODE system, Population ODE, derived from ODE models of single cell. The Population ODE could well approximate the expected value of species concentration in a population of cell in most cases. We have tested Population ODE in some well-known signaling pathways including EGFR pathway and NFκB pathway and Population ODE can well approximate the population behavior with a single simulation. Because Population ODE failed to approximate the cell-population behavior in bistable system, we developed our second method, Sample Reduction. Sample Reduction is a sampling-based method, similar to Monte Carlo simulation.

However, through significantly reduction of the sampling space, we were able to significantly reduce the sample size required, which makes the simulation much faster.

Cell-to-cell variability is a common phenomenon in many types of cells. Since typical computational modeling of signaling pathway simulates single-cell behavior while most biological experiments measures species from a population of cells, there is often a discrepancy between computational models and bulk experiments. Monte Carlo simulation can simulate cell-population behavior but it is often time consuming. Therefore, developing algorithms for fast simulation of population behavior can be beneficial for most computational modeling studies, not only our study of TGF-β networks. Our methods are not only faster than Monte Carlo simulation. Population ODE also has capability of using all kinds of analysis which can be applied to typical ODE models. The case of integrating TGF-β upstream network and downstream signaling shows the advantage of using Population ODE. Because we wanted to integrate a network outside the cell and a population of pathways inside cells, it is ideal to have a system as a whole to represent a population of cells. Population ODE can serve the purpose because it is still an ODE system. It may also be useful in other cases because the methods we use for ODE system can be directly applied to Population ODE as an analysis of the population behavior. In an integrated TGF-β networks, perturbation analysis or sensitivity analysis could be applied to both the upstream species and downstream species in the same system. The integrated model of TGF-β networks is a better tool to predict combination of drug targets. Synergistic effect is often seen in a

bistable system. A combination of upstream target and downstream target may exist and the integrated model has the capability of finding this kind of combination.

In the case of integrating TGF-β networks, we have seen that the bistable behavior still maintained even if we considered cell-to-cell variability. This bistable behavior was compared to a co-culture experiments in which hepatocytes and hepatic stellate cells (HSCs) were uniformly seeded in the culture dish (Venkatraman et al., 2012). In this case, although cells express TSP1 (in HSCs) and PAI1 (in both hepatocytes and HSCs) differently, the secretion was transient and the molecules were mixed in the culture medium quickly before they reach any steady state. However, in *in vivo* situation of liver fibrosis, the fibrotic regions do not distribute evenly. Therefore, two steady states of TGF-β may exist at different regions of liver tissue. The concentrations of molecules may not be affected mainly by the mixing effect but mainly by the stability of steady states. This spatial property of liver fibrosis led us to move one step further to a tissue-level model to study the spatial dynamics of a bistable system.

5 Chapter 5: Diffusion Model of TGF-β Activation Network

5.1 Introduction

Liver fibrosis is a wound-healing response caused by injury of liver parenchyma. Different types of liver injury could lead to different patterns of pathogenesis in liver fibrosis (Hernandez-Gea and Friedman, 2011). For example, chronic hepatitis C causes fibrotic septa connecting portal tracts and central vein; and biliary fibrosis has the pattern of portal-portal fibrotic septa. Among these different patterns, there is a common phenomenon that fibrotic region does not distribute uniformly in liver tissue. It is often seen that part of the tissue becomes fibrotic with accumulation of ECM and large number of hepatic stellate cells (HSCs) (Cassiman et al., 2002, Knittel et al., 1999). The fibrotic region is surrounded by normal tissue with hepatocytes as the dominant cell type and less ECM.

Previously we have briefly introduced Venkatraman's bistable model of TGF-β activation (Venkatraman et al., 2012). The two steady states of this model are related to normal and fibrotic states in liver tissue. Here we introduce the two states in more detail. Figure 5.1 shows the TGF-β activation network in Venkatraman's model. The two major players: plasmin and TSP1 are expressed mainly in hepatocytes (red cells) and activated HSCs (blue cell) respectively. In normal liver tissue, hepatocytes are dominant and also the negative feedback in this network (left part of the diagram in Figure 5.1). On the other hand, in fibrotic tissue, hepatocytes are damaged and activated HSCs are much more than that in

normal tissue. Therefore the positive feedback (right part of the diagram in Figure 5.1) is dominant in fibrotic tissue. It was shown in Venkatraman's model that one steady state of the system had high levels of TGF-β and TSP1 and low level of plasmin. This is consistent with the fibrotic state in liver when the positive feedback is dominant. The other steady state shown in Venkatraman's model has low levels of TGF-β and TSP1 and high level of plasmin. This can be explained by the dominance of the negative feedback in normal state in liver because plasmin can inhibit TSP1 irreversibly to break the positive feedback loop. The reason why TGF-β is relatively low when the negative feedback is dominant is that plasmin is a relatively weak activator of TGF-β comparing to TSP1. In summary, TGF-β-low and TGF-β-high steady state in this network can be respectively related to normal state and fibrotic state of liver tissue.

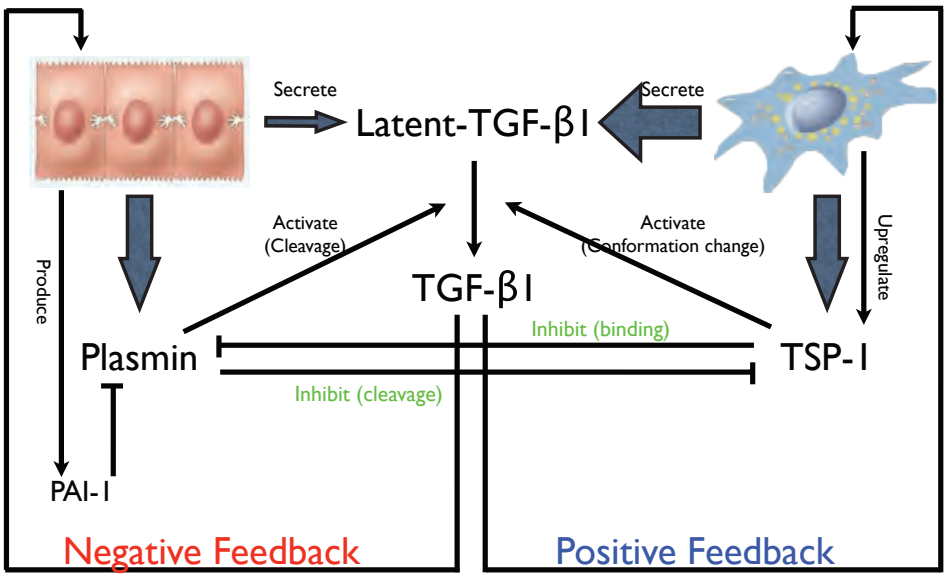

Figure 5.1 The schematic diagram of TGF-β activation network in liver fibrosis. The red cells represent hepatocytes and the blue cell represents activated HSCs (fibroblast-like).

High level of TGF-β in the fibrotic state may induce more activation of HSCs and then more ECM secretion. It has been predicted and experimentally validated that plasmin, a representative species of the normal state, has potential to switch fibrotic state to normal state (Venkatraman et al., 2012). Based on Venkatraman's model, we believe that the regression of liver fibrosis might be led by switching of fibrotic state to normal state. As we mentioned, fibrotic tissue is often surrounded by normal tissue. We thought that computational modeling could help us initiate studies of the spatial effect between normal tissue and fibrotic tissue. The molecule exchange between normal and fibrotic tissue could affect the steady state of molecules and further affect the state of the cells and even tissue. On the other hand, the accumulation of ECM in liver fibrosis could block the molecule exchange. We therefore asked how the two steady states in TGF-β activation network would affect each other and whether the accumulation of ECM could affect the reversibility of liver fibrosis.

In this study, we built our so-called diffusion model on top of Venkatraman's model of TGF-β activation network to allow species in this network to diffuse in space. The diffusion process in this model was simulated by a finite-element approximation. Instead of using partial differential equations (PDE), we discretized the space into small blocks/regions (Figure 5.2) and the diffusion of species between adjacent blocks was modeled by mass action reactions and ODEs. ODE modeling of the diffusion process allowed us to easily integrate the model of TGF-β activation network with diffusion, and to easily simulate the diffusion model.

Our diffusion model predicted a solution of a traveling wave in space. The wave propagated because one steady state affected the other steady state nearby and made it to switch. The model also predicted that the wave direction was always from TGF-β-low (normal) state to TGF-β-high (fibrotic) state. This prediction is similar to liver fibrosis regression and was also shown to be highly robust. We also experimentally confirmed that the central species of the normal state, plasmin could be blocked from reducing TGF-β activation by the low diffusion rate. Finally, we showed that our model not only predicted the direction of the wave, but also could serve as a platform to compute the wave speed.

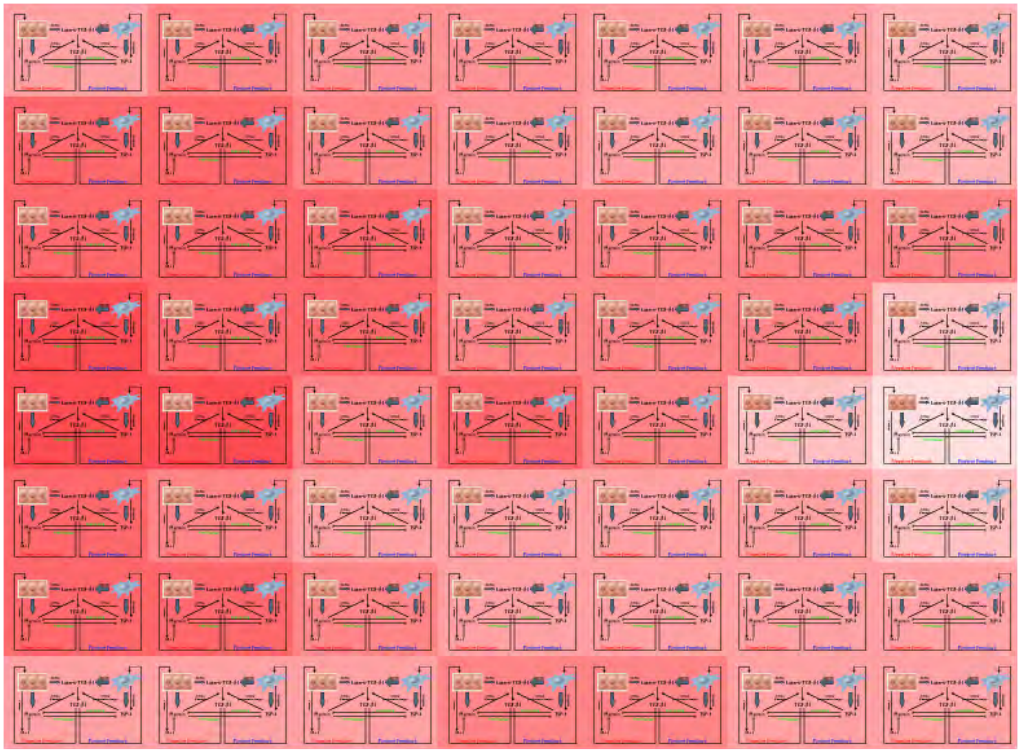

Figure 5.2 Graphical representation of the diffusion model. The whole space was discretized into small blocks and the model of TGF-β activation network (Venkatraman et al., 2012) was included in every block. Different color represents different concentration of species.

5.2 Materials and Methods

5.2.1 Simulation of the Diffusion Model

The diffusion process in our diffusion model was approximated by discretization of space and mass action reactions. As shown in Figure 5.3, a species P could have different concentrations in different regions of the space. We modeled the diffusion of species P as a set of reactions in Equation (5.1).

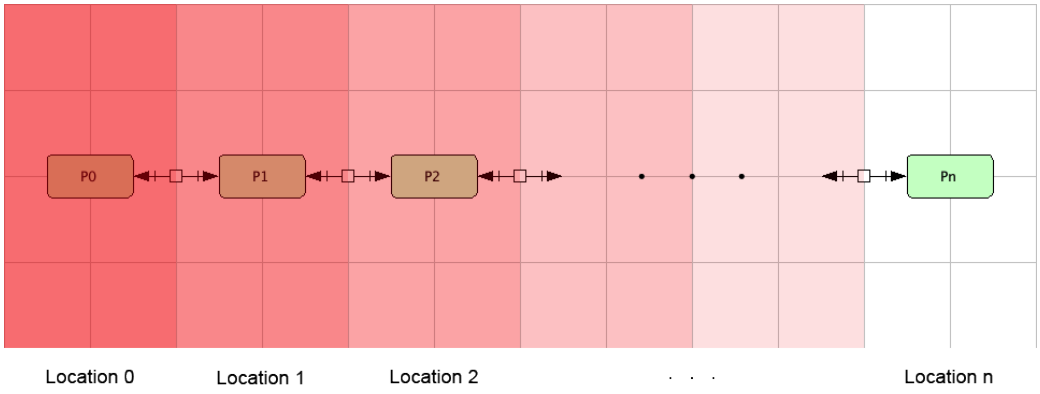

Figure 5.3 Mass action reaction as an approximation of the diffusion of a species.

$$P_0 \underset{kdiff}{\overset{kdiff}{\rightleftharpoons}} P_1 \underset{kdiff}{\overset{kdiff}{\rightleftharpoons}} \cdots \underset{kdiff}{\overset{kdiff}{\rightleftharpoons}} P_n \tag{5.1}$$

Here the diffusion rate ($kdiff$) depends on the size of the discretized space and its relationship to the diffusion coefficient (D) in physics can be expressed as in Equation (5.2). In this equation, D is defined to have the unit of cm^2/s. Thus, we defined the length of a region as l (assuming discretization is the same and uniform in all dimensions) to have the unit of cm. Then $kdiff$ has the unit of s^{-1}.

$$kdiff = \frac{D}{l^2} \tag{5.2}$$

Then, we were able to build the diffusion model as a whole ODE model. Assuming the species concentrations in a region i is a vector $\boldsymbol{x}_i$, we express the species concentrations in all regions in the whole space as a long vector as below.

$$\boldsymbol{x} = \begin{pmatrix} \boldsymbol{x}_1 \\ \vdots \\ \boldsymbol{x}_n \end{pmatrix} \tag{5.3}$$

Because the local reactions are the same in all regions and the diffusion reactions are all first order, the whole diffusion model could be written as in Equation (5.4). The function $F(t, \boldsymbol{x}_i)$ is the same for all regions. The term $\boldsymbol{Dx}$ represents the diffusion reactions and note the matrix $\boldsymbol{D}$ is different from the diffusion coefficient, D, which is a scalar.

$$\frac{d\boldsymbol{x}}{dt} = \begin{pmatrix} F(t, \boldsymbol{x}_1) \\ \vdots \\ F(t, \boldsymbol{x}_n) \end{pmatrix} + \boldsymbol{Dx} \tag{5.4}$$

The diffusion model could be large depending on the number of regions. Fortunately, the diffusion system has an explicit form of the Jacobian matrix so we can simulate the system efficiently. The Jacobian matrix of the whole system is as in Equation (5.5). Simulation was done using Matlab ODE solver ode15s.

$$\boldsymbol{J} = \begin{pmatrix} \dfrac{\partial F(t, \boldsymbol{x}_1)}{\partial \boldsymbol{x}_1} & \boldsymbol{0} & \boldsymbol{0} \\ \boldsymbol{0} & \ddots & \boldsymbol{0} \\ \boldsymbol{0} & \boldsymbol{0} & \dfrac{\partial F(t, \boldsymbol{x}_n)}{\partial \boldsymbol{x}_n} \end{pmatrix} + \boldsymbol{D} \tag{5.5}$$

5.2.2 Stochastic Simulation of ECM Accumulation

In this simulation, we assumed two stochastic events of ECM production and degradation. The rates of these two events were determined by TGF-β level as in Equation (5.6) below. The parameter k_{ECM} determined how fast ECM was regulated by TGF-β. We also set an upper bound ($[ECM]_{max}$) and a lower bound ($[ECM]_{min}$) for ECM to avoid negative or extremely high amount of ECM. $[TGF\beta]_{low}$ was the low steady state of TGF-β. This made the production rate and degradation rate balanced when TGF-β was at its low steady state (normal state).

$$\begin{cases} R_{prod} = k_{ECM}[TGF\beta]([ECM]_{max} - [ECM]) \\ R_{deg} = k_{ECM}[TGF\beta]_{low}([ECM] - [ECM]_{min}) \end{cases} \tag{5.6}$$

We simulated these two stochastic reactions using binomial τ-leap algorithm (Chatterjee et al., 2005). The amount of ECM was initated from 1 at all regions in space. After the amount of ECM was changed, we divided the diffusion rates (*kdiff*) for two adjacent regions by the averaged ECM in these two regions. The diffusion model was continuously simulated and only *kidff* in the diffusion model needs to be updated after each time step of stochastic simulation. As we set the k_{ECM} to be much smaller than the reaction rates, the change of ECM was much slower than changes of all other species and the time step of stochastic simulation is large enough for the effect of diffusion to be stablized.

5.2.3 Cell Culture Experiments

T6 cell line was cultured for 3 days in 1ml of DMEM culture medium with 10% FBS to make sure the cells were activated (T6 cells undergo self-activation on hard

surface such as plastic). In the groups without collagen, cell culture insert was not used and plasmin was added directly into the well. In those groups with collagen, collagen solution was coated on the PET membrane of culture inserts and was incubated overnight at 37°C. After that, plasmin was diluted in 500ul of DMEM medium and the solution was added into the culture insert. In such cases, the concentration of plasmin was calculated as the total amount of plasmin added divided by the total volume of medium in the well and the insert (1.5ml).

5.3 Results

5.3.1 Diffusion Effect of Bistable System Shows a Traveling Wave in Space

It has been proven mathematically that diffusion effect of simple bistable system exhibits a wave propagation behavior in space (Bates et al., 2006). It is also known from the theoretical study that the wave speed is related to the diffusion coefficient *D*. However, the direction of the traveling wave is often non-obvious in complex systems like TGF-β activation network, as it depends on the parameters of the system. We simulated our diffusion model to first confirm the traveling wave behavior and secondly to see the direction of the wave if it exists.

We did multiple simulations of the diffusion model in one-dimensional space with different diffusion rates (*kdiff*, please see the relationship between *kdiff* and the diffusion coefficient *D* in Material and Methods, Section 5.2.1). In each simulation, diffusion rate was the same for all species for simplification. Representative

simulation results are shown in Figure 5.4. In these simulations, we initiated the system with 1 region at TGF-β-low (normal) steady state and other 99 regions at TGF-β-high (fibrotic) steady state. As shown in Figure 5.4A, there was an obvious traveling wave from normal state to fibrotic state. After we decreased the diffusion rate, the traveling wave still existed but the wave speed was slower (Figure 5.4B). We also decreased the diffusion rate to extremely low values. For better visualization, we initiated the system with half normal and half fibrotic states in this case. The traveling wave completely disappeared when the diffusion rate was too low (actually lower than a threshold, data not shown) even though we simulate the system for very long time (i.e. 10^{10}s, Figure 5.4C). This disappearance of the traveling wave was an artifact of the discretization. We will show the relationship between the wave speed and the diffusion rate (*kdiff*) as well as the diffusion coefficient (D), and theoretical existence of traveling wave at low diffusion rate.

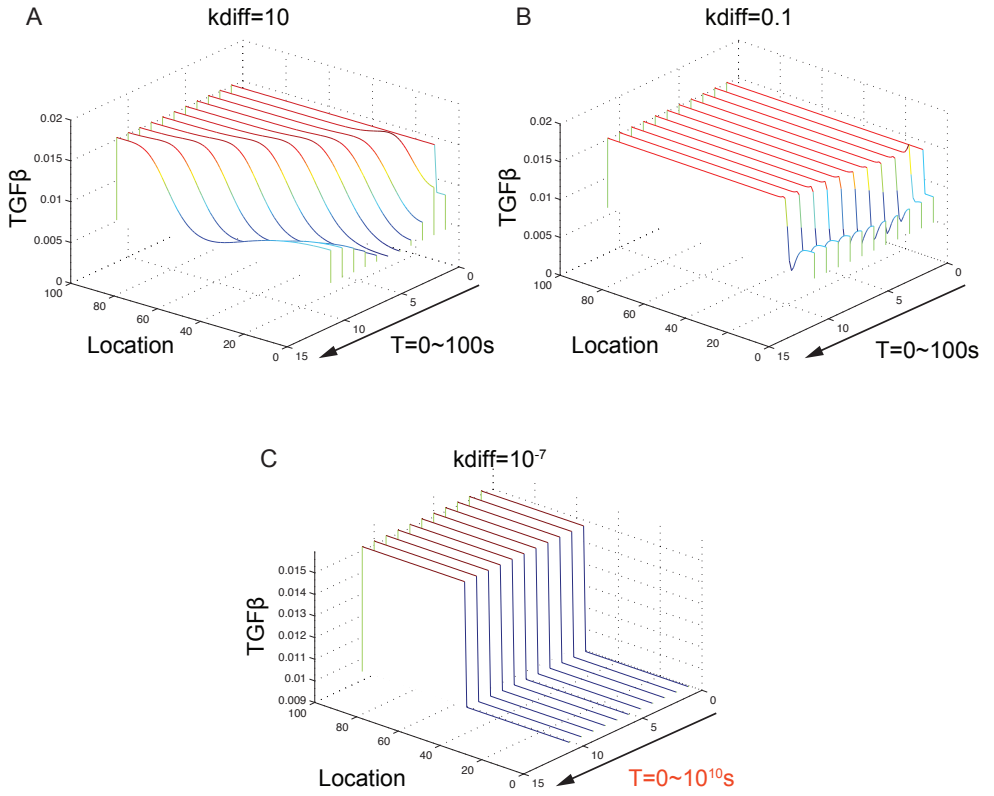

Figure 5.4 Traveling waves in the diffusion model of TGF-β activation network. Simulation of TGF-β concentration in space was plotted at 10 different time points. The color in the curves indicates the concentration of TGF-β (red: high concentration; blue: low concentration). (A) Simulation of 1D diffusion with the diffusion rate *kdiff*=10. The model was simulated from 0 to 100s. (B) Simulation of 1D diffusion with the diffusion rate *kdiff*=0.1. The model was simulated from 0 to 100s. (C) Simulation of 1D diffusion with the diffusion rate *kdiff*=10^{-7}. The model was simulated from 0 to 10^{10}s.

Note that the traveling wave was always directed from TGF-β-low (normal) steady state to TGF-β-high (fibrotic) steady state. Superisingly, this directional effect between normal and fibrotic regions is similar to liver fibrosis regression *in vivo* because fibrosis regresses spontaneously if there is no outside perturbations (i.e. liver injury) to the system. However, this direction was only a prediction of the model and it could be affected by the parameters in the local TGF-β activation network and different diffusion rates of different species. Although it is difficult to

prove the direction from normal to fibrotic tissue experimentally, we can at least analyze how robust this prediction is.

5.3.2 Robustness Analysis of the Traveling Wave Direction

In the robustness analysis, we initiated the diffusion model with half normal state and half fibrotic state in space. After perturbing parameters such as diffusion rates and rate constants, we simulated the system to see the direction of the traveling wave. It was possible that some combinations of parameters could result in no traveling wave (artifact of discretization) or even making the system mono-stable. We therefore categorized the simulation results with different parameters to four categories: 1) traveling wave from normal state to fibrotic state; 2) traveling wave from fibrotic state to normal state; 3) no traveling wave; 4) mono-stable system (Figure 5.5). It is possible that different species could have different diffusion rates in the ECM because of their molecular weights, charge and different affinities to ECM proteins. Therefore, we randomly varied diffusion rates in the range of 10^{-2} to 10^{2} for different species. Each polygon in the polar plot in Figure 5.5A shows a combination of different diffusion rates for all species and the color of the polygon indicates the category of simulation results (listed on the top of the figure). All polygons are blue in this case suggested that the wave direction from normal state to fibrotic state is highly robust to diffusion rate as well as the differences of diffusion rates among species. The rate constants in local systems could also affect the wave direction. We then varied all rate constants randomly with less than 20% perturbation for each rate constants. We chose the range 20% based on previous robustness analysis that about 80% of the models were still

bistable with 20% perturbation of each rate constants (Venkatraman et al., 2012). As shown in Figure 5.5B, most of the models showed traveling wave from normal to fibrotic state. This suggested that the wave direction from normal to fibrotic state was also highly robust to the change of reaction rates in local systems. We can also infer that this traveling wave direction depends more on the structure of TGF-β activation network (biologically validated) but less on the kinetic rates.

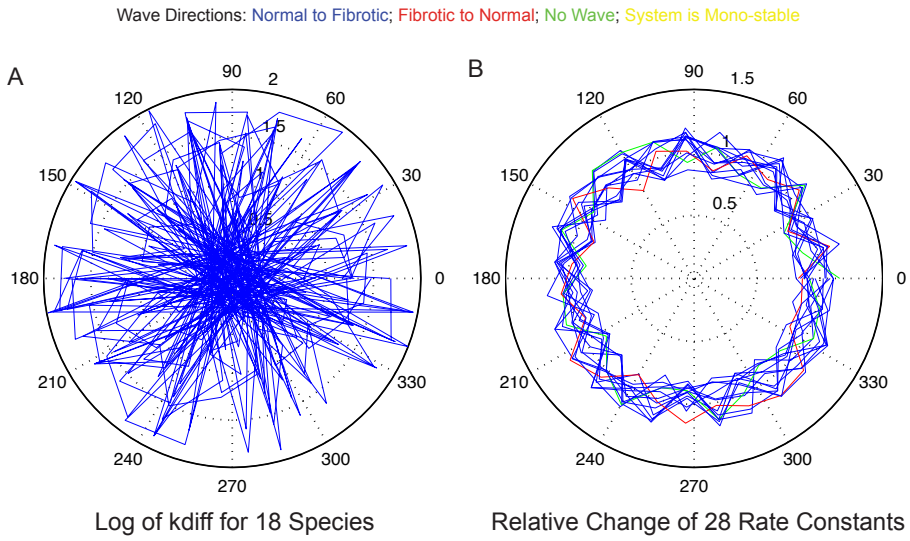

Figure 5.5 Robustness analysis of traveling wave direction. Top of the figure shows 4 categories of the simulation results with color labels. (A) The log of 18 diffusion rates (*kdiff*) for 18 species was plotted on the polar plot along 18 different angles. The radius represents the log of each *kdiff*. A combination of 18 diffusion rates was connected to a ploygon and the color labels the category of simulation results. (B) The normalized values of 28 rate constants was plotted on the polar plot along 28 different angles. The radius represents the normalized value of each rate constant. A combination of 28 rate constants was connected to a ploygon and the color labels the category of simulation results.

5.3.3 Wave Speed, Diffusion Rate and Diffusion Coefficient

Our diffusion model could predict the direction of traveling wave and our analysis showed that the wave from normal state to fibrotic state was robust. This diffusion model is also capable of predicting the speed of the wave. The wave speed

highly depends on the diffusion rates of different species, and also the reaction rates. Although these rates were not validated and our prediction of wave speed could be inaccurate, our model can still be used to compare relative change of speed at different conditions. We also show that our model simulation could be a platform for computing the wave speed when measurements of certain rates are available.

We again simulated the diffusion model in one-dimensional space for computing of the wave speed. As we have shown that the direction of the wave was only from normal state to fibrotic state, we initiated the system with 5 region at normal state (TGF-β low) and 95 other regions at fibrotic state (TGF-β high). We have also shown that too small *kdiff* could cause no wave propagation in simulation (artifact of discretization). Thus, we set *kdiff* to be large enough to have traveling wave in simulation. To compute the speed of the wave, we snapshot the wave front position at a frame rate of 100s (Figure 5.6A). The wave front position and time showed a clear linear relationship (Figure 5.6B). This means that the wave speed was a constant when it propagated through the space and we could easily compute the wave speed as the slope of the straight line in Figure 5.6B. Note that the wave speed we calculated has the unit of region/s.

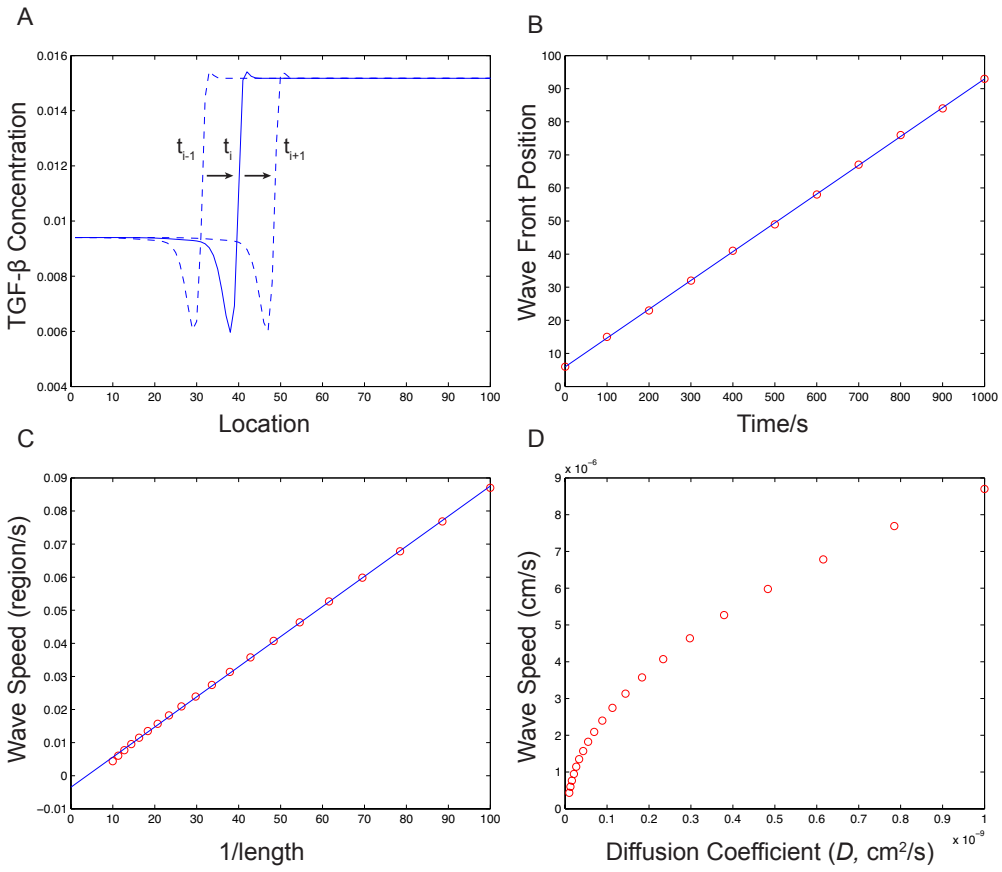

Figure 5.6 Computing the speed of the traveling wave based on simulations. (A) Wave front at three time frames (t_{i-1}, t_i and t_{i+1}). The exact position of the wave front was computed as the position having TGF-β concentration closest to the mean of two steady-state concentrations of TGF-β. (B) The wave front position at 11 time frames (red circles) and the linear curve-fit to the red circles (blue line). (C) The wave speed calculated with different *kdiff* (10^{-3} to 10^{-1}) versus the reciprocal of the length of the subspace (red circle). The blue line is the linear curve-fit to the red circles. (D) The relationship between the wave speed and diffusion coefficient.

Then we wanted to examine the relationship between *kdiff* and the wave speed. We varied *kdiff* (from 10^{-3} to 10^{-1}) and computed the wave speed for each *kdiff* using the method we described above. What does the relationship between *kdiff* and the wave speed (region/s) mean? According to the relationship between the diffusion rate (*kdiff*) and diffusion coefficient (*D*) in the Materials and Methods (Section 5.2.1), the change of the diffusion rate (*kdiff*) in the diffusion model could

mean either the change of the diffusion coefficient (D) or the change of the length (l) of the subspace, or even both. Then, is the wave speed dependent on *kdiff* or *D*? To answer this question, we set the diffusion coefficient D=10^{-5}cm^2/s, which is approximately the coefficient of proteins diffusing in water. With the *kdiff* values we set for model simulation (10^{-3} to 10^{-1}), we can calculate the length of the subspace $l = \sqrt{\frac{10^{-5}}{kdiff}}(cm)$ according to Equation (5.2). Then we plotted the wave speed (region/s) versus $\frac{1}{l}$. Figure 5.6C shows a linear relationship between wave speed (region/s) and $\frac{1}{l}$. This means that the real wave speed (cm^2/s), which equals the wave speed (region/s) times the length of subspace/region l, is a constant. Therefore, we confirmed that the wave speed was only affected by the diffusion coefficient D when the rate constants were fixed. The slope of the straight line in Figure 5.6C is actually the real wave speed (cm^2/s). We then plotted the relationship between the real wave speed and the diffusion coefficient D Figure 5.6D. The wave speed increases when the diffusion coefficient increases.

5.3.4 Plasmin Could be Blocked From Inhibiting TGF-β Activation by Low Diffusion Coefficient

Our model predicted that low diffusion coefficient could cause slow wave propagation, meaning that normal state switched its adjacent fibrotic state more slowly. When normal state switched its adjacent fibrotic state, plasmin played a central role because it could break the positive feedback loop of TSP1 and then inhibit TGF-β activation. We therefore wanted to experimentally test whether the

inhibition of TGF-β activation could be blocked by low diffusion coefficient. We used a cell culture system with cell culture inserts to do the test. As shown in Figure 5.7A, we cultured T6 cell line (rat HSCs) at the bottom of the well. Then we added plasmin into the system either directly in the well or in the culture insert with a layer of collagen gel slowing the diffusion of plasmin from top chamber to the bottom chamber. Plasmin has a short half life in culture medium so its inhibition effect decreases significantly after certain time. We measured active TGF-β after 2hr treatment of plasmin because the inhibition effect was maximized at 2hr (data not shown). Figure 5.7B shows the ELISA measurement of active TGF-β in our culture system. In the control group without plasmin treatment, T6 cells express high level of active TGF-β. Active TGF-β level was significantly reduced with high level of plasmin (500ng/ml). However, this reduction of TGF-β was significantly blocked by a thick layer of collagen (500ul in 6-well plate). This experiment confirmed that low diffusion coefficient (or excessive ECM) could block the effect of plasmin inhibiting TGF-β activation.

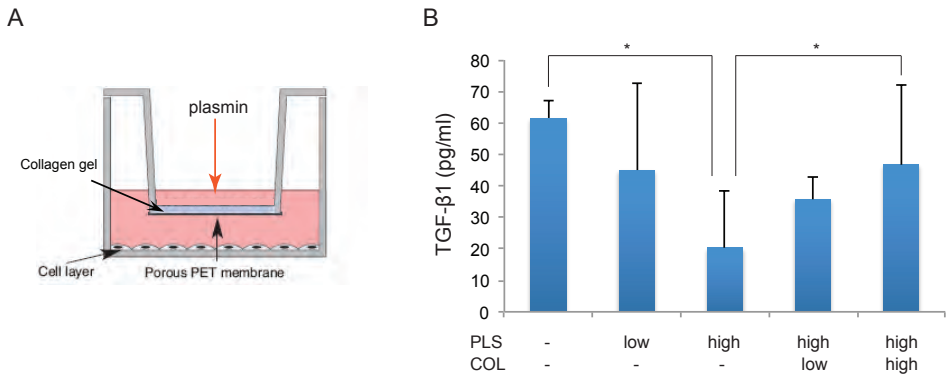

Figure 5.7 Plasmin could inhibit TGF-β activation but the inhibition could be blocked by low diffusion coefficient (thick collagen). (A) The experimental design using cell culture insert. T6 cells were cultured at the bottom (cell layer). The cell culture insert has a porous PET membrane

at its bottom. Collagen gel was coated on the PET membrane. Plasmin was added either into the culture insert or directly into the culture medium. (B) ELISA measurement of active TGF-β in the culture medium (mean of 3 biological replicates). Different concentration of plasmin were added (low: 200ng/ml; high: 500ng/ml). Different amount of collagen was coated in the culture insert for 6-well plate (low: 200ul; high: 500ul). The asterisk indicates significant changes between groups ($p<0.05$, t-test was used).

5.3.5 Stochastic Simulation of ECM Accumulation Under Chronic Injury

Based on the fact that plasmin could be blocked by excessive ECM, it is possible that the excessive ECM localized in the fibrotic tissue could block plasmin from its adjacent normal tissue and then slow down the switch of fibrotic state to normal state (a sign of fibrosis regression). It is known that high level of TGF-β could induce activation of HSCs and secretion of ECM proteins . We then wanted to simulate the effect of TGF-β-high steady state on slow accumulation of ECM. We did not know how exactly ECM proteins were regulated by TGF-β steady states and we simply simulated this as two stochastic events: ECM production and degradation. The firing rates of these events depended on TGF-β levels. After firing a event of ECM production or degradation, the amount of ECM in a certain region in space was changed, we then changed the diffusion rates according to the amount of ECM. The detailed setup and simulation method of this stochastic model are described in the Materials and Methods (Section 5.2.2).

After setting up the model, we initiated the model with all normal steady states in the whole space. Then, we introduced repeated injury, represented by sudden increase of TGF-β, to simulate liver fibrosis caused by chronic injury. The simulation result is shown in an attached movie file (Movie_5.1.mov). We can see

from the movie that at early stage, fibrotic state could be recovered back to normal. However, when ECM slowly accumulated, the wave speed (speed of regression) becomes slower and it was more and more difficult for the normal regions to switch the state of the fibrotic regions. Interestingly, this simulation result is similar to liver fibrosis progression *in vivo*. In most cases, with mild acute injury, fiborsis could regress after the injury is removed, while fibrosis progresses when the injury is chronic.

5.4 Discussion

In this study, we built a diffusion model of TGF-β activation network. This model simulated how two steady states of a bistable system would affect each other in space. The simulation results first showed a traveling wave from normal state to fibrotic state. We further confirmed by computational analysis that this direction of wave was robust. Our model could also predict the speed of the traveling wave and it showed a positive correlation between diffusion coefficient D and wave speed. Our experiment of plasmin treated HSCs suggested that plasmin could be blocked from inhibiting TGF-β activation by low diffusion. Since plasmin was a major player in the wave from normal state to fibrotic state, our experimental result was consistent with the prediction that low diffusion coefficient was correlated to low wave speed. Based on the experimental test and model prediction, we further added stochastic change of ECM into our diffusion model. With this model, we were able to simulate the effect of repeated injury causing accumulation of ECM and slowing

down the speed of regression. This predicted behavior is consistent with the observations in liver fibrosis.

This work is an initiation of studying spatial effect in liver fibrosis and other biological processes. Observation of dynamic changes of molecules or cells *in vivo* is still a challenging task in biological studies. However, computational modeling can handle the spatial dynamics quite well. In our study, we predicted a traveling wave of a bistable system in space. We also predicted that the wave speed could be significantly affected by the amount of extracellular matrix. It would be good if future studies validated our model predictions. Validating the traveling wave is a challenging task. First of all, bistable behavior in the extracellular matrix is difficult to measure. This is mostly because the molecules are not as concentrated as those in cells. Reporter genes or reporter cells may be used in the system as an indicator of the TGF-β level in the extracellular matrix, for example. Secondly, observing dynamical change in the extracellular matrix is also difficult. To validate the traveling wave, future work might still need to measure steady state changes in two chamber of culture systems. Perturbation can also be applied to the system to see if certain perturbation can change the direction of the traveling wave. This could further support the existence of traveling wave. Tissue imaging can also be used to study the effect of diffusion in liver fibrosis. Fluorescence-labeled proteins can be observed in tissue slice and its location can be easily determined from the images. The disadvantage of tissue imaging is that we cannot observe dynamic changes of the concentration of localization of molecules from tissue slice, but studies using tissue imaging is more relevant to liver fibrosis than cell culture

studies. Our modeling could also be used to generate interesting predictions which can be tested by more static measurements such as imaging of fixed tissue samples. Taking our study as an example, our final perdition of the repeated injury suggests that ECM accumulation in the fibrotic region could block the anti-fibrotic effect in its neighbor. Not only the effect from the normal tissue, but also the treatments outside the fibrotic region could be blocked. Therefore, treatments targeting the fibrotic region should be more efficient and might be even necessary.

6 Chapter 6: Conclusion

In this thesis, we used computational and systematic analysis to study TGF-β related regulations in liver fibrosis at three levels: cellular level, cell population level and tissue level.

We first studied TGF-β signaling pathway within cells. In this part of study, tightly coupled computational analysis and experiments suggested that current knowledge of negative regulations in this pathway could not explain the dynamics of phospho-R-Smad. We then sought alternative mechanisms extensively using computational analysis. We ruled out many possible mechanisms and we found that PPM1A upregulation could not be ruled out by our modeling studies. With the support of biological experiments, we finally concluded with a model which could explain all measured data from both literature and our experiments. This final model was also capable of explaining a contradiction in the literature. This level of understanding of the negative regulations in TGF-β signaling pathway could not be achieved from only a biological point of view. Computational modeling and systems biology approach gained us further insights into observed phenomenon and led us to discover novel mechanism.

Motivated by previous study of TGF-β activation network in the ECM and the fact that cell-to-cell variability is common in many types of cells, we wanted to integrate our TGF-β signaling pathway within cells with the TGF-β activation network outside the cell. The integration would obviously affected by the cell-to-cell variability and we wanted to simulate a population of cells in a faster way. We

then focused on developing two algorithms to efficiently approximate the species concentrations in a population of cells based on single-cell models. We tested the performance of our algorithms in some well-known pathway models and applied one of our algorithm, Population ODE to the problem of integrating TGF-β activation network and intracellular signaling pathway. Population ODE was used to approximate a population of intracellular pathways and the Population ODE (not the model for intracellular pathway) was integrated with the TGF-β activation network outside the cells. Population ODE is ideal for this integration because it is not sampling based. Our algorithms also have potentials to be applied to other systems when cell-to-cell variability needs to be considered.

Inspired by the simulation of a population of cells in liver fibrosis and the fact that fibrotic tissue is often distributed unevenly in liver fibrosis, we moved one step further from a population of uniformly distributed cells to spatially localized different states of tissue. The bistability of the TGF-β activation network is a good representation of two states of tissue in liver fibrosis, normal state and fibrotic state. It is difficult to observe *in vivo* how fibrotic tissue and normal tissue could affect each other in space. However, our *in silico* simulations could generate meaningful predictions. Our model simulations predicted a robust behavior that normal state could switch its adjacent fibrotic state and formed a traveling wave of regression. The speed of the wave could be reduced by excessive ECM. The effect of plasmin on inhibiting TGF-β activation was confirmed experimentally to be blocked by low diffusion. Our model was also capable to predicting the effect of repeated injury in liver fibrosis. This prediction is consistent with the fact that only repeated injury

could cause continuous accumulation of ECM. This prediction also suggested that treatments targeting fibrotic region might be more efficient.

6.1 Future Work

With the understanding of TGF-β regulations in liver fibrosis at multiple levels and multiple scales, we have improved the models and systematic studies of TGF-β and its regulations in liver fibrosis.

One of the future perspectives could be experimental validation of detaild mechanism of PPM1A upregulation. Our model analysis suggested how PPM1A could be upregulated by stabilization, but how each step of interaction happens need to be validated by more biological studies. This could be a new biological project and it could be guided by our current model.

Another future work could be improvement of our algorithms of approximating cell-population behavior. There is still some room for improvement such as reducing time steps in Population ODE simulation and better choice of the sensitivity matrix in Sample Reduction. It would be also great if these algorithms could be integrated into parameter estimation methods. Then single-cell models could be fitted to bulk experiment without the assumption that cells are identical. Applying our algorithms to other kinds of analysis such as bifurcation analysis could also be interesting.

A simple assumption of diffusion could possibly explain the progression of chronic liver disease. The diffusion model may open a new door to the field of liver fibrosis or even other biological systems. Both computational and biological studies

could consider more about the spatial behaviors. For example, late stage of liver fibrosis, cirrhosis is characterized by destruction of blood vessels in liver tissue. It is generally considered that cirrhosis is hard to be reversed. How the spatial change of liver tissue could result in irreversibility remains a question. Studies focusing on the spatial properties may help us answer this kind of questions.

7 Bibliography

AFRAKHTE, M., MOREN, A., JOSSAN, S., ITOH, S., SAMPATH, K., WESTERMARK, B., HELDIN, C. H., HELDIN, N. E. & TEN DIJKE, P. 1998. Induction of inhibitory Smad6 and Smad7 mRNA by TGF-beta family members. Biochem Biophys Res Commun, 249, 505-11.

AGGARWAL, K. & MASSAGUE, J. 2012. Ubiquitin removal in the TGF-beta pathway. Nat Cell Biol, 14, 656-7.

ALARCON, C., ZAROMYTIDOU, A. I., XI, Q., GAO, S., YU, J., FUJISAWA, S., BARLAS, A., MILLER, A. N., MANOVA-TODOROVA, K., MACIAS, M. J., SAPKOTA, G., PAN, D. & MASSAGUE, J. 2009. Nuclear CDKs drive Smad transcriptional activation and turnover in BMP and TGF-beta pathways. Cell, 139, 757-69.

ALBECK, J. G., BURKE, J. M., SPENCER, S. L., LAUFFENBURGER, D. A. & SORGER, P. K. 2008. Modeling a Snap-Action, Variable-Delay Switch Controlling Extrinsic Cell Death. PLoS Biol. 2008/12/05 ed.

ALBERGHINA, L. & WESTERHOFF, H. V. 2005. Systems biology: definitions and perspectives.

ANNES, J. P., MUNGER, J. S. & RIFKIN, D. B. 2003. Making sense of latent TGFbeta activation. J Cell Sci, 116, 217-24.

ANONICK, P. K., YOO, J. K., WEBB, D. J. & GONIAS, S. L. 1993. Characterization of the antiplasmin activity of human thrombospondin-1 in solution. Biochem J, 289 (Pt 3), 903-9.

ARTHUR, M. J. 1997. Matrix degradation in liver: a role in injury and repair. Hepatology, 26, 1069-71.

ASHALL, L., HORTON, C. A., NELSON, D. E., PASZEK, P., HARPER, C. V., SILLITOE, K., RYAN, S., SPILLER, D. G., UNITT, J. F., BROOMHEAD, D. S., KELL, D. B., RAND, D. A., SÉE, V. & WHITE, M. R. H. 2009. Pulsatile stimulation determines timing and specificity of NF-kappaB-dependent transcription. Science.

ATTISANO, L. & WRANA, J. L. 2002. Signal transduction by the TGF-beta superfamily. Science, 296, 1646-7.

BAKIN, A. V., TOMLINSON, A. K., BHOWMICK, N. A., MOSES, H. L. & ARTEAGA, C. L. 2000. Phosphatidylinositol 3-kinase function is required for transforming growth factor beta-mediated epithelial to mesenchymal transition and cell migration. J Biol Chem, 275, 36803-10.

BARABASI, A. L. & OLTVAI, Z. N. 2004. Network biology: understanding the cell's functional organization. Nat Rev Genet, 5, 101-13.

BASSING, C. H., YINGLING, J. M., HOWE, D. J., WANG, T., HE, W. W., GUSTAFSON, M. L., SHAH, P., DONAHOE, P. K. & WANG, X. F. 1994. A transforming growth factor beta type I receptor that signals to activate gene expression. Science, 263, 87-9.

BATALLER, R. & BRENNER, D. A. 2005. Liver fibrosis. J Clin Invest, 115, 209-18.

BATES, P. W., CHEN, X. & CHMAJ, A. J. J. 2006. Traveling Waves of Bistable Dynamics on a Lattice. SIAM J Math Anal, 35, 520-546.

BENYON, R. C. & IREDALE, J. P. 2000. Is liver fibrosis reversible? Gut, 46, 443-6.

BU, S., KAPANADZE, B., HSU, T. & TROJANOWSKA, M. 2008. Opposite effects of dihydrosphingosine 1-phosphate and sphingosine 1-phosphate on transforming growth factor-beta/Smad signaling are mediated through the PTEN/PPM1A-dependent pathway. J Biol Chem, 283, 19593-602.

CASSIMAN, D., LIBBRECHT, L., DESMET, V., DENEF, C. & ROSKAMS, T. 2002. Hepatic stellate cell/myofibroblast subpopulations in fibrotic human and rat livers. Journal of hepatology, 36, 200-9.

CHATTERJEE, A., VLACHOS, D. G. & KATSOULAKIS, M. A. 2005. Binomial distribution based tau-leap accelerated stochastic simulation. J Chem Phys, 122, 024112.

CHEN, W. W., SCHOEBERL, B., JASPER, P. J., NIEPEL, M., NIELSEN, U. B., LAUFFENBURGER, D. A. & SORGER, P. K. 2009. Input–output behavior of ErbB signaling pathways as revealed by a mass action model trained against dynamic data. Mol Syst Biol.

CHUNG, S. W., MILES, F. L., SIKES, R. A., COOPER, C. R., FARACH-CARSON, M. C. & OGUNNAIKE, B. A. 2009. Quantitative modeling and analysis of the transforming growth factor beta signaling pathway. Biophys J, 96, 1733-50.

CITRI, A. & YARDEN, Y. 2006. EGF–ERBB signalling: towards the systems level. Nat Rev Mol Cell Biol.

CLARKE, D. C., BROWN, M. L., ERICKSON, R. A., SHI, Y. & LIU, X. 2009. Transforming growth factor beta depletion is the primary determinant of Smad signaling kinetics. Molecular and cellular biology, 29, 2443-55.

CURRIER, A. R., SABLA, G., LOCAPUTO, S., MELIN-ALDANA, H., DEGEN, J. L. & BEZERRA, J. A. 2003. Plasminogen directs the pleiotropic effects of uPA in liver injury and repair. Am J Physiol Gastrointest Liver Physiol, 284, G508-15.

DALLAS, S. L., ROSSER, J. L., MUNDY, G. R. & BONEWALD, L. F. 2002. Proteolysis of latent transforming growth factor-beta (TGF-beta)-binding protein-1 by osteoclasts. A cellular mechanism for release of TGF-beta from bone matrix. J Biol Chem, 277, 21352-60.

DANIEL, C., WIEDE, J., KRUTZSCH, H. C., RIBEIRO, S. M., ROBERTS, D. D., MURPHY-ULLRICH, J. E. & HUGO, C. 2004. Thrombospondin-1 is a major activator of TGF-beta in fibrotic renal disease in the rat in vivo. Kidney Int, 65, 459-68.

DESMET, V. J. & ROSKAMS, T. 2004. Cirrhosis reversal: a duel between dogma and myth. Journal of hepatology, 40, 860-7.

DI GUGLIELMO, G. M., LE ROY, C., GOODFELLOW, A. F. & WRANA, J. L. 2003. Distinct endocytic pathways regulate TGF-beta receptor signalling and turnover. Nat Cell Biol, 5, 410-21.

EBISAWA, T., FUKUCHI, M., MURAKAMI, G., CHIBA, T., TANAKA, K., IMAMURA, T. & MIYAZONO, K. 2001. Smurf1 interacts with transforming growth factor-beta type I receptor through Smad7 and induces receptor degradation. J Biol Chem, 276, 12477-80.

EICHHORN, P. J., RODON, L., GONZALEZ-JUNCA, A., DIRAC, A., GILI, M., MARTINEZ-SAEZ, E., AURA, C., BARBA, I., PEG, V., PRAT, A., CUARTAS, I., JIMENEZ, J., GARCIA-DORADO, D., SAHUQUILLO, J., BERNARDS, R., BASELGA, J. & SEOANE, J. 2012. USP15 stabilizes TGF-beta receptor I and promotes oncogenesis through the activation of TGF-beta signaling in glioblastoma. Nat Med, 18, 429-35.

EISSING, T. 2004. Bistability Analyses of a Caspase Activation Model for Receptor-induced Apoptosis. Journal of Biological Chemistry.

ENG, F. J. & FRIEDMAN, S. L. 2000. Fibrogenesis I. New insights into hepatic stellate cell activation: the simple becomes complex. Am J Physiol Gastrointest Liver Physiol, 279, G7-G11.

FRIEDMAN, S. L. 2000. Molecular regulation of hepatic fibrosis, an integrated cellular response to tissue injury. J Biol Chem, 275, 2247-50.

FRIEDMAN, S. L. 2003. Liver fibrosis -- from bench to bedside. J Hepatol, 38 Suppl 1, S38-53.

GOUMANS, M. J., VALDIMARSDOTTIR, G., ITOH, S., ROSENDAHL, A., SIDERAS, P. & TEN DIJKE, P. 2002. Balancing the activation state of the endothelium via two distinct TGF-beta type I receptors. EMBO J, 21, 1743-53.

GRESSNER, A. M. & WEISKIRCHEN, R. 2006. Modern pathogenetic concepts of liver fibrosis suggest stellate cells and TGF-beta as major players and therapeutic targets. J Cell Mol Med, 10, 76-99.

GRESSNER, A. M., WEISKIRCHEN, R., BREITKOPF, K. & DOOLEY, S. 2002. Roles of TGF-beta in hepatic fibrosis. Front Biosci, 7, d793-807.

HAMMEL, P., COUVELARD, A., O'TOOLE, D., RATOUIS, A., SAUVANET, A., FLEJOU, J. F., DEGOTT, C., BELGHITI, J., BERNADES, P., VALLA, D., RUSZNIEWSKI, P. & LEVY, P. 2001. Regression of liver fibrosis after biliary drainage in patients with chronic pancreatitis and stenosis of the common bile duct. N Engl J Med, 344, 418-23.

HAYASHI, H., ABDOLLAH, S., QIU, Y., CAI, J., XU, Y. Y., GRINNELL, B. W., RICHARDSON, M. A., TOPPER, J. N., GIMBRONE, M. A., JR., WRANA, J. L. & FALB, D. 1997. The MAD-related protein Smad7 associates with the TGFbeta receptor and functions as an antagonist of TGFbeta signaling. Cell, 89, 1165-73.

HERNANDEZ-GEA, V. & FRIEDMAN, S. L. 2011. Pathogenesis of liver fibrosis. Annual review of pathology, 6, 425-56.

HJELMELAND, A. B., HJELMELAND, M. D., SHI, Q., HART, J. L., BIGNER, D. D., WANG, X. F., KONTOS, C. D. & RICH, J. N. 2005. Loss of phosphatase and tensin homologue increases transforming growth factor beta-mediated invasion with enhanced SMAD3 transcriptional activity. Cancer research, 65, 11276-81.

HOFFMANN, A. 2002. The Ikappa B-NF-kappa B Signaling Module: Temporal Control and Selective Gene Activation. Science.

HOGG, P. J., STENFLO, J. & MOSHER, D. F. 1992. Thrombospondin is a slow tight-binding inhibitor of plasmin. Biochemistry, 31, 265-9.

INUI, M., MANFRIN, A., MAMIDI, A., MARTELLO, G., MORSUT, L., SOLIGO, S., ENZO, E., MORO, S., POLO, S., DUPONT, S., CORDENONSI, M. & PICCOLO, S. 2011. USP15 is a deubiquitylating enzyme for receptor-activated SMADs. Nat Cell Biol, 13, 1368-75.

IREDALE, J. P. 2007. Models of liver fibrosis: exploring the dynamic nature of inflammation and repair in a solid organ. J Clin Invest, 117, 539-48.

IREDALE, J. P., BENYON, R. C., PICKERING, J., MCCULLEN, M., NORTHROP, M., PAWLEY, S., HOVELL, C. & ARTHUR, M. J. 1998. Mechanisms of spontaneous resolution of rat liver fibrosis. Hepatic stellate cell apoptosis and reduced hepatic expression of metalloproteinase inhibitors. J Clin Invest, 102, 538-49.

ITOH, S., LANDSTROM, M., HERMANSSON, A., ITOH, F., HELDIN, C. H., HELDIN, N. E. & TEN DIJKE, P. 1998. Transforming growth factor beta1 induces nuclear export of inhibitory Smad7. J Biol Chem, 273, 29195-201.

KAVSAK, P., RASMUSSEN, R. K., CAUSING, C. G., BONNI, S., ZHU, H., THOMSEN, G. H. & WRANA, J. L. 2000. Smad7 binds to Smurf2 to form an E3 ubiquitin ligase that targets the TGF beta receptor for degradation. Mol Cell, 6, 1365-75.

KELLEY, L. A. & STERNBERG, M. J. 2009. Protein structure prediction on the Web: a case study using the Phyre server. Nat Protoc, 4, 363-71.

KHOLODENKO, B. N., DEMIN, O. V., MOEHREN, G. & HOEK, J. B. 1999. Quantification of short term signaling by the epidermal growth factor receptor. J Biol Chem, 274, 30169-81.

KINNMAN, N., GORIA, O., WENDUM, D., GENDRON, M. C., REY, C., POUPON, R. & HOUSSET, C. 2001. Hepatic stellate cell proliferation is an early platelet-derived growth factor-mediated cellular event in rat cholestatic liver injury. Lab Invest, 81, 1709-16.

KLIPP, E. & ZI, Z. 2007. Constraint-based modeling and kinetic analysis of the smad dependent tgf-Beta signaling pathway. PLoS ONE, 2, e936.

KNITTEL, T., KOBOLD, D., PISCAGLIA, F., SAILE, B., NEUBAUER, K., MEHDE, M., TIMPL, R. & RAMADORI, G. 1999. Localization of liver myofibroblasts and hepatic stellate cells in normal and diseased rat livers: distinct roles of (myo-)fibroblast subpopulations in hepatic tissue repair. Histochemistry and cell biology, 112, 387-401.

KONDOU, H., MUSHIAKE, S., ETANI, Y., MIYOSHI, Y., MICHIGAMI, T. & OZONO, K. 2003. A blocking peptide for transforming growth factor-beta1 activation prevents hepatic fibrosis in vivo. J Hepatol, 39, 742-8.

KUTZ, S. M., HIGGINS, C. E., SAMARAKOON, R., HIGGINS, S. P., ALLEN, R. R., QI, L. & HIGGINS, P. J. 2006. TGF-beta 1-induced PAI-1 expression is E box/USF-dependent and requires EGFR signaling. Exp Cell Res, 312, 1093-105.

LEE, T. K. & COVERT, M. W. 2010. High-throughput, single-cell NF-Î¹B dynamics. Current Opinion in Genetics & Development. Elsevier Ltd.

LEE, T. K., DENNY, E. M., SANGHVI, J. C., GASTON, J. E., MAYNARD, N. D., HUGHEY, J. J. & COVERT, M. W. 2009. A Noisy Paracrine Signal Determines the Cellular NF- B Response to Lipopolysaccharide. Science Signaling.

LIN, X., DUAN, X., LIANG, Y. Y., SU, Y., WRIGHTON, K. H., LONG, J., HU, M., DAVIS, C. M., WANG, J., BRUNICARDI, F. C., SHI, Y., CHEN, Y. G., MENG, A. & FENG, X. H. 2006. PPM1A functions as a Smad phosphatase to terminate TGFbeta signaling. Cell, 125, 915-28.

LIN, X., LIANG, M. & FENG, X. H. 2000. Smurf2 is a ubiquitin E3 ligase mediating proteasome-dependent degradation of Smad2 in transforming growth factor-beta signaling. J Biol Chem, 275, 36818-22.

LO, R. S. & MASSAGUE, J. 1999. Ubiquitin-dependent degradation of TGF-beta-activated smad2. Nat Cell Biol, 1, 472-8.

LYONS, R. M., GENTRY, L. E., PURCHIO, A. F. & MOSES, H. L. 1990. Mechanism of activation of latent recombinant transforming growth factor beta 1 by plasmin. J Cell Biol, 110, 1361-7.

MASSAGUE, J. 1998. TGF-beta signal transduction. Annu Rev Biochem, 67, 753-91.

MASSAGUE, J., BLAIN, S. W. & LO, R. S. 2000. TGFbeta signaling in growth control, cancer, and heritable disorders. Cell, 103, 295-309.

MASSAGUE, J. & WOTTON, D. 2000. Transcriptional control by the TGF-beta/Smad signaling system. EMBO J, 19, 1745-54.

MELKE, P., JONSSON, H., PARDALI, E., TEN DIJKE, P. & PETERSON, C. 2006. A rate equation approach to elucidate the kinetics and robustness of the TGF-beta pathway. Biophys J, 91, 4368-80.

MURPHY-ULLRICH, J. E. & POCZATEK, M. 2000. Activation of latent TGF-beta by thrombospondin-1: mechanisms and physiology. Cytokine Growth Factor Rev, 11, 59-69.

NAKAKUKI, T., BIRTWISTLE, M. R., SAEKI, Y., YUMOTO, N., IDE, K., NAGASHIMA, T., BRUSCH, L., OGUNNAIKE, B. A., OKADA-HATAKEYAMA, M. & KHOLODENKO, B. N. 2010. Ligand-Specific c-Fos Expression Emerges from the Spatiotemporal Control of ErbB Network Dynamics. Cell. Elsevier Ltd.

NAKAO, A., AFRAKHTE, M., MOREN, A., NAKAYAMA, T., CHRISTIAN, J. L., HEUCHEL, R., ITOH, S., KAWABATA, M., HELDIN, N. E., HELDIN, C. H. & TEN DIJKE, P. 1997. Identification of Smad7, a TGFbeta-inducible antagonist of TGF-beta signalling. Nature, 389, 631-5.

NELSON, D. E. 2004. Oscillations in NF- B Signaling Control the Dynamics of Gene Expression. Science.

NUMMINEN, K., SIPILA, O. & MAKISALO, H. 2005. Preoperative hepatic 3D models: virtual liver resection using three-dimensional imaging technique. Eur J Radiol, 56, 179-84.

SALGADO, S., GARCIA, J., VERA, J., SILLER, F., BUENO, M., MIRANDA, A., SEGURA, A., GRIJALVA, G., SEGURA, J., OROZCO, H., HERNANDEZ-PANDO, R., FAFUTIS, M., AGUILAR, L. K., AGUILAR-CORDOVA, E. &

ARMENDARIZ-BORUNDA, J. 2000. Liver cirrhosis is reverted by urokinase-type plasminogen activator gene therapy. Mol Ther, 2, 545-51.

SCHMIERER, B. & HILL, C. S. 2005. Kinetic analysis of Smad nucleocytoplasmic shuttling reveals a mechanism for transforming growth factor beta-dependent nuclear accumulation of Smads. Mol Cell Biol, 25, 9845-58.

SCHMIERER, B., TOURNIER, A. L., BATES, P. A. & HILL, C. S. 2008. Mathematical modeling identifies Smad nucleocytoplasmic shuttling as a dynamic signal-interpreting system. Proc Natl Acad Sci U S A, 105, 6608-13.

SCHOEBERL, B., EICHLER-JONSSON, C., GILLES, E. D. & MULLER, G. 2002. Computational modeling of the dynamics of the MAP kinase cascade activated by surface and internalized EGF receptors. Nat Biotechnol, 20, 370-5.

SCHULTZ-CHERRY, S., RIBEIRO, S., GENTRY, L. & MURPHY-ULLRICH, J. E. 1994. Thrombospondin binds and activates the small and large forms of latent transforming growth factor-beta in a chemically defined system. J Biol Chem, 269, 26775-82.

SHERMAN, I. A., PAPPAS, S. C. & FISHER, M. M. 1990. Hepatic microvascular changes associated with development of liver fibrosis and cirrhosis. The American journal of physiology, 258, H460-5.

SHI, W., SUN, C., HE, B., XIONG, W., SHI, X., YAO, D. & CAO, X. 2004. GADD34-PP1c recruited by Smad7 dephosphorylates TGFbeta type I receptor. J Cell Biol, 164, 291-300.

SHI, Y. & MASSAGUE, J. 2003. Mechanisms of TGF-beta signaling from cell membrane to the nucleus. Cell, 113, 685-700.

SHMULEVICH, I., DOUGHERTY, E. R., KIM, S. & ZHANG, W. 2002. Probabilistic Boolean Networks: a rule-based uncertainty model for gene regulatory networks. Bioinformatics, 18, 261-74.

SIVAKUMAR, K. C., DHANESH, S. B., SHOBANA, S., JAMES, J. & MUNDAYOOR, S. 2011. A systems biology approach to model neural stem cell regulation by notch, shh, wnt, and EGF signaling pathways. OMICS, 15, 729-37.

SPENCER, S. L., GAUDET, S., ALBECK, J. G., BURKE, J. M. & SORGER, P. K. 2009a. Non-genetic origins of cell-to-cell variability in TRAIL-induced apoptosis. Nature, 459, 428-32.

SPENCER, S. L., GAUDET, S., ALBECK, J. G., BURKE, J. M. & SORGER, P. K. 2009b. Non-genetic origins of cell-to-cell variability in TRAIL-induced apoptosis. Nature. 2009/04/14 ed.

TAY, S., HUGHEY, J. J., LEE, T. K., LIPNIACKI, T., QUAKE, S. R. & COVERT, M. W. 2010. Single-cell NF-κB dynamics reveal digital activation and analogue information processing. Nature.

TOETTCHER, J. E., APGAR, J. F., CASTILLO, A. R., TIDOR, B. & WHITE, J. 2011. Recycling Circuit Simulation Techniques for Mass-Action Biochemical Kinetics. In: LI, P., SILVEIRA, L. M., FELDMANN, P. & EDS. (eds.) chapter in Simulation and Verification of Electronic and Biological Systems. Springer.

VANHEULE, E., GEERTS, A. M., VAN HUYSSE, J., SCHELFHOUT, D., PRAET, M., VAN VLIERBERGHE, H., DE VOS, M. & COLLE, I. 2008. An intravital microscopic study of the hepatic microcirculation in cirrhotic mice models: relationship between fibrosis and angiogenesis. International journal of experimental pathology, 89, 419-32.

VASSALLI, J. D., SAPPINO, A. P. & BELIN, D. 1991. The plasminogen activator/plasmin system. J Clin Invest, 88, 1067-72.

VENKATRAMAN, L., CHIA, S. M., NARMADA, B. C., WHITE, J. K., BHOWMICK, S. S., FORBES DEWEY, C., JR., SO, P. T., TUCKER-KELLOGG, L. & YU, H. 2012. Plasmin triggers a switch-like decrease in thrombospondin-dependent activation of TGF-beta1. Biophys J, 103, 1060-8.

VENKATRAMAN, L., YU, H., BHOWMICK, S. S., DEWEY, F. & TUCKER-KELLOGG, L. 2010. The steady States and dynamics of urokinase-mediated plasmin activation. Pac Symp Biocomput, 190-200.

VILAR, J. M., JANSEN, R. & SANDER, C. 2006. Signal processing in the TGF-beta superfamily ligand-receptor network. PLoS Comput Biol, 2, e3.

VOLLMAR, B., SIEGMUND, S. & MENGER, M. D. 1998. An intravital fluorescence microscopic study of hepatic microvascular and cellular derangements in developing cirrhosis in rats. Hepatology, 27, 1544-53.

WEISS, J. N., QU, Z. & GARFINKEL, A. 2003. Understanding biological complexity: lessons from the past. FASEB J, 17, 1-6.

WILEY, H. S. & CUNNINGHAM, D. D. 1981. A steady state model for analyzing the cellular binding, internalization and degradation of polypeptide ligands. Cell, 25, 433-40.

WRANA, J. L. & ATTISANO, L. 2000. The Smad pathway. Cytokine Growth Factor Rev, 11, 5-13.

YINGLING, J. M., BLANCHARD, K. L. & SAWYER, J. S. 2004. Development of TGF-beta signalling inhibitors for cancer therapy. Nature reviews. Drug discovery, 3, 1011-22.

ZEISBERG, M., YANG, C., MARTINO, M., DUNCAN, M. B., RIEDER, F., TANJORE, H. & KALLURI, R. 2007. Fibroblasts derive from hepatocytes in liver fibrosis via epithelial to mesenchymal transition. J Biol Chem, 282, 23337-47.

ZHANG, L., ZHOU, F., DRABSCH, Y., GAO, R., SNAAR-JAGALSKA, B. E., MICKANIN, C., HUANG, H., SHEPPARD, K. A., PORTER, J. A., LU, C. X. & TEN DIJKE, P. 2012. USP4 is regulated by AKT phosphorylation and directly deubiquitylates TGF-beta type I receptor. Nat Cell Biol, 14, 717-26.

ZI, Z., FENG, Z., CHAPNICK, D. A., DAHL, M., DENG, D., KLIPP, E., MOUSTAKAS, A. & LIU, X. 2011. Quantitative analysis of transient and sustained transforming growth factor-beta signaling dynamics. Molecular systems biology, 7, 492.

8 Appendix

8.1 Appendix for Chapter 3

8.1.1 Appendix Tables of Smad Pathway Models

Table 8.1 Initial Concentrations (I.C.) in nM. Nuclear species have been expressed relative to the concentrations in cytoplasm.

Species Name	Species Description	I.C.	Reference
TGF-β	The TGF-β ligand	80	(Klipp 2007)
$T1R_{Surf}$	The type I receptor on the cell surface	0.237	(Klipp 2007)
$T1R_{Cave}$	The type I receptor in the caveolae	2.092	(Klipp 2007)
$T1R_{EE}$	The type I receptor in the early endosome	2.06	(Klipp 2007)
$T2R_{Surf}$	The type II receptor on the cell surface	0.202	(Klipp 2007)
$T2R_{Cave}$	The type II receptor in the caveolae	1.778	(Klipp 2007)
$T2R_{EE}$	The type II receptor in the early endosome	1.148	(Klipp 2007)
$pT2R_{Surf}$	Ligand-bound type II receptor on the cell surface	0	
$pT2R_{Cave}$	Ligand-bound type II receptor in the caveolae	0	
$pT2R_{EE}$	Ligand-bound type II receptor in the early endosome	0	
LRC_{Surf}	The ligand-receptor complex on the cell surface	0	
LRC_{Cave}	The ligand-receptor complex in the caveolae	0	
LRC_{EE}	The ligand-receptor complex in the early endosome	0	
T1R:T2R	The T1R-T2R complex released from LRC	0	
RI	The receptor inhibitor SB-431542	600	(Schmierer 2008)
LRC_{EE}:RI	The complex of the receptor inhibitor and LRC	0	
LRC:Smad2	The complex of Smad2 and LRC	0	
$Smad2_{Cyt}$	Smad2 in the cytoplasm	494.67	(Klipp 2007)
$Smad2_{Nuc}$	Smad2 in the nucleus	76.76	(Klipp 2007)
$pSmad2_{Cyt}$	Phosphorylated Smad2 in the cytoplasm	0	
$pSmad2_{Nuc}$	Phosphorylated Smad2 in the nucleus	0	
$Smad4_{Cyt}$	Smad4 in the cytoplasm	666.65	(Klipp 2007)
$Smad4_{Nuc}$	Smad4 in the nucleus	666.65	(Klipp 2007)
$Smad2:Smad4_{Cyt}$	The complex of Smad2 and Smad4 in the cytoplasm	0	
$Smad2:Smad4_{Nuc}$	The complex of Smad2 and Smad4 in the nucleus	0	
$Smad2:Smad2_{Cyt}$	The homo-dimer of Smad2 in the cytoplasm	0	
$Smad2:Smad2_{Nuc}$	The homo-dimer of Smad2 in the nucleus	0	
Smad7	Smad7	0	
$dephLRC_{Cave}$	Dephosphorylated LRC in the caveolae	0	
$dephLRC_{EE}$	Dephosphorylated LRC in the early endosome	0	
LRC_{Cave}:Smad7	The complex of Smad7 and LRC in the caveolae	0	
LRC_{EE}:Smad7	The complex of Smad7 and LRC in the early endosome	0	
$PPM1A_{Cyt}$	PPM1A in the cytoplasm	1	
$PPM1A_{Nuc}$	PPM1A in the nucleus	100	
$PTEN_{Cyt}$	PTEN in the cytoplasm	estimated	
$PTEN_{Nuc}$	PTEN in the nucleus	0	
$pSmad2:PPM1A_{Cyt}$	The complex of pSmad2 and PPM1A in the cytoplasm	0	
$pSmad2:PPM1A:PTEN_{Cyt}$	The complex of pSmad2 and PPM1A:PTEN in the cytoplasm	0	
$pSmad2:PTEN_{Cyt}$	The complex of pSmad2 and PTEN in the cytoplasm	0	
$pSmad2:PTEN:PPM1A_{Cyt}$	The complex of pSmad2:PTEN and PPM1A in the cytoplasm	0	
$PPM1A:PTEN_{Cyt}$	The PPM1A-PTEN complex released from pSmad2:PTEN:PPM1A in the cytoplasm	0	
$pSmad2:PPM1A_{Nuc}$	The complex of pSmad2 and PPM1A in the nucleus	0	
$pSmad2:PPM1A:PTEN_{Nuc}$	The complex of pSmad2 and PPM1A:PTEN in the nucleus	0	
$PPM1A:PTEN_{Cyt}$	The PPM1A-PTEN complex released from pSmad2:PTEN:PPM1A in the nucleus	0	

Table 8.2 Rate Constants

Rate Constant Name	Values	Reference
v_{T1R}	0.0103	(Klipp 2007)
v_{T2R}	0.02869	(Klipp 2007)
ki_{EE}	0.33	(Klipp 2007)
kr_{EE}	0.033	(Klipp 2007)
ki_{Cave}	0.33	(Klipp 2007)
kr_{Cave}	0.03742	(Klipp 2007)
$kdeg_{T1R}$	0.005	(Klipp 2007)
$kdeg_{T2R}$	0.025	(Klipp 2007)
kcd	0.005	(Klipp 2007)
$kLRC_1$	estimated	
$kLRC_2$	estimated	
$kr_{Receptor}$	10000	
kfSmad2	estimated	
krSmad2	estimated	
kfSmadsComplex	estimated	
krSmadsComplex	estimated	
$kimp_{Smad2}$	0.054	(Schmierer 2008)
$kexp_{Smad2}$	0.348	(Schmierer 2008)
$kimp_{Smad4}$	0.054	(Schmierer 2008)
$kexp_{Smad4}$	0.054	(Schmierer 2008)
$kimp_{SmadsComplex}$	0.27	(Schmierer 2008)
klid	estimated	
$kdeph_{pSmad2}$	estimated	
$kdeg_{pSmad2}$	estimated	
v_{Smad2}	estimated	
$kdeg_{Smad2}$	estimated	
kSmad7	estimated	
$kfSmad7_{Cave}$	estimated	
$kbSmad7_{Cave}$	estimated	
$kfSmad7_{EE}$	estimated	
$kbSmad7_{EE}$	estimated	
$kdeph_{LRC:Smad7}$	estimated	
$kdeg_{LRC:Smad7}$	estimated	
v_{PPM1A}	estimated	
$kdeg_{PPM1A}$	estimated	
kfPPM1A	estimated	
kbPPM1A	estimated	
krPPM1A	estimated	
$kdeph_{PPM1A}$	estimated	
kfPP	estimated	
kbPP	estimated	
krPP	estimated	
kfPTEN	estimated	
kbPTEN	estimated	
$kimp_{PPM1A}$	estimated	
$kimp_{PP}$	estimated	
$kexp_{PP}$	estimated	
$kexp_{PTEN}$	estimated	
kfRI	100	(Schmierer 2008)
kbRI	684	(Schmierer 2008)

Table 8.3 Reactions Table: All reactions in Model 1-11 with rate constants labeled. (Continued on the next page)

	Reaction	Models
1	$\xrightarrow{v_{T1R}} T1R_{Surf}$	All
2	$\xrightarrow{v_{T2R}} T2R_{Surf}$	All
3	$T1R_{Surf} \underset{kr_{EE}}{\overset{ki_{EE}}{\rightleftharpoons}} T1R_{EE}$	All
4	$T1R_{Surf} \underset{kr_{Cave}}{\overset{ki_{Cave}}{\rightleftharpoons}} T1R_{Cave}$	All
5	$T2R_{Surf} \underset{kr_{EE}}{\overset{ki_{EE}}{\rightleftharpoons}} T2R_{EE}$	All
6	$T2R_{Surf} \underset{kr_{Cave}}{\overset{ki_{Cave}}{\rightleftharpoons}} T2R_{Cave}$	All
7	$pT2R_{Surf} \underset{kr_{EE}}{\overset{ki_{EE}}{\rightleftharpoons}} pT2R_{EE}$	All
8	$pT2R_{Surf} \underset{kr_{Cave}}{\overset{ki_{Cave}}{\rightleftharpoons}} pT2R_{Cave}$	All
9	$T1R_{EE} \xrightarrow{kdeg_{T1R}}$	All
10	$T2R_{EE} \xrightarrow{kdeg_{T2R}}$	All
11	$pT2R_{EE} \xrightarrow{kdeg_{T2R}}$	All
12	$TGF\beta + T2R_{Surf} \xrightarrow{kLRC_1} pT2R_{Surf}$	All
13	$pT2R_{Surf} + T1R_{Surf} \xrightarrow{kLRC_2} LRC_{Surf}$	All
14	$LRC_{Surf} \xrightarrow{ki_{EE}} LRC_{EE}$	All
15	$LRC_{EE} \xrightarrow{kr_{EE}} T1R:T2R + TGF\beta$	All
16	$LRC_{Surf} \xrightarrow{ki_{Cave}} LRC_{Cave}$	All
17	$LRC_{Cave} \xrightarrow{kr_{Cave}} T1R:T2R + TGF\beta$	All
18	$T1R:T2R \xrightarrow{krR} T1R_{Surf} + T2R_{Surf}$	All
19	$LRC_{EE} \xrightarrow{kcd}$	All
20	$LRC_{EE} + Smad2_{Cyt} \xrightarrow{kfSmad2} LRC:Smad2$	All
21	$LRC:Smad2 \xrightarrow{krSmad2} LRC_{EE} + pSmad2_{Cyt}$	All
22	$pSmad2_{Cyt} + Smad4_{Cyt} \xrightarrow{kfSmadsComplex} Smad2:Smad4_{Cyt}$	All
23	$pSmad2_{Cyt} + pSmad2_{Cyt} \xrightarrow{kfSmadsComplex} Smad2:Smad2_{Cyt}$	All
24	$pSmad2_{Nuc} + Smad4_{Nuc} \underset{krSmadsComplex}{\overset{kfSmadsComplex}{\rightleftharpoons}} Smad2:Smad4_{Nuc}$	All
25	$pSmad2_{Nuc} + pSmad2_{Nuc} \underset{krSmadsComplex}{\overset{kfSmadsComplex}{\rightleftharpoons}} Smad2:Smad2_{Nuc}$	All
26	$Smad2_{Cyt} \underset{kexp_{Smad2}}{\overset{kimp_{Smad2}}{\rightleftharpoons}} Smad2_{Nuc}$	All
27	$pSmad2_{Cyt} \underset{kexp_{Smad2}}{\overset{kimp_{Smad2}}{\rightleftharpoons}} pSmad2_{Nuc}$	All
28	$Smad4_{Cyt} \underset{kexp_{Smad4}}{\overset{kimp_{Smad4}}{\rightleftharpoons}} Smad4_{Nuc}$	All
29	$Smad2:Smad4_{Cyt} \xrightarrow{kimp_{SmadsComplex}} Smad2:Smad4_{Nuc}$	All
30	$Smad2:Smad2_{Cyt} \xrightarrow{kimp_{SmadsComplex}} Smad2:Smad2_{Nuc}$	All

31	$LRC_{Cave} + Smad2:Smad4_{Nuc} \xrightarrow{klid}$	Model(2,3,5)
32	$LRC_{Cave} + Smad2:Smad2_{Nuc} \xrightarrow{klid}$	Model(2,3,5)
33	$pSmad2_{Nuc} \xrightarrow{kdeph_{pSmad2}} Smad2_{Nuc}$	Model(1,2,5,6,7,8)
34	$pSmad2_{Nuc} \xrightarrow{kdeg_{pSmad2}}$	Model(4,5,6,7,11)
35	$\underset{kdeg_{Smad2}}{\overset{v_{Smad2}}{\rightleftharpoons}} Smad2_{Cyt}$	Model(7,11)
36	$Smad2_{Cyt} \xrightarrow{kdeg_{Smad2}}$	Model(7,11)
37	$Smad2_{Nuc} \xrightarrow{kdeg_{Smad2}}$	Model(7,11)
38	$pSmad2_{Cyt} \xrightarrow{kdeg_{Smad2}}$	Model(7,11)
39	$pSmad2_{Nuc} \xrightarrow{kdeg_{Smad2}}$	Model(7,11)
40	$Smad2:Smad4_{Nuc} \xrightarrow{kSmad7} Smad2:Smad4_{Nuc} + Smad7$	Model(8)
41	$Smad2:Smad2_{Nuc} \xrightarrow{kSmad7} Smad2:Smad2_{Nuc} + Smad7$	Model(8)
42	$Smad7 \xrightarrow{kcd}$	Model(8)
43	$LRC_{EE}:Smad7 \xrightarrow{kcd}$	Model(8)
44	$LRC_{Cave} + Smad7 \underset{krSmad7_{Cave}}{\overset{kfSmad7_{Cave}}{\rightleftharpoons}} LRC_{Cave}:Smad7$	Model(8)
45	$LRC_{EE} + Smad7 \underset{krSmad7_{EE}}{\overset{kfSmad7_{EE}}{\rightleftharpoons}} LRC_{EE}:Smad7$	Model(8)
46	$LRC_{Cave}:Smad7 \xrightarrow{kdeph_{LRC:Smad7}} dephLRC_{Cave} + Smad7$	Model(8)
47	$LRC_{EE}:Smad7 \xrightarrow{kdeph_{LRC:Smad7}} dephLRC_{EE} + Smad7$	Model(8)
48	$LRC_{Cave}:Smad7 \xrightarrow{kdeg_{LRC:Smad7}}$	Model(8)
49	$LRC_{EE}:Smad7 \xrightarrow{kdeg_{LRC:Smad7}}$	Model(8)
50	$dephLRC_{Cave} \xrightarrow{kr_{Cave}} T1R:T2R + TGF\beta$	Model(8)
51	$dephLRC_{EE} \xrightarrow{kr_{EE}} T1R:T2R + TGF\beta$	Model(8)
52	$\underset{kdeg_{PPM1A}}{\overset{v_{PPM1A}}{\rightleftharpoons}} PPM1A_{Nuc}$	Model(9)
53	$\underset{kdeg_{PPM1A}}{\overset{v_{PPM1A}}{\rightleftharpoons}} PPM1A_{Cyt}$	Model(10,11)
54	$PPM1A_{Nuc} \xrightarrow{kdeg_{PPM1A}}$	Model(10,11)
55	$PPM1A_{Cyt} \xrightarrow{kimp_{PPM1A}} PPM1A_{Nuc}$	Model(10,11)
56	$Smad2:Smad4_{Nuc} \xrightarrow{kPPM1A} Smad2:Smad4_{Nuc} + PPM1A_{Nuc}$	Model(9)
57	$Smad2:Smad2_{Nuc} \xrightarrow{kPPM1A} Smad2:Smad2_{Nuc} + PPM1A_{Nuc}$	Model(9)
58	$pSmad2_{Nuc} + PPM1A_{Nuc} \underset{kbPPM1A}{\overset{kfPPM1A}{\rightleftharpoons}} pSmad2:PPM1A_{Nuc}$	Model(9,10,11)
59	$pSmad2:PPM1A_{Nuc} \xrightarrow{kdeph_{PPM1A}} Smad2_{Nuc} + PPM1A_{Nuc}$	Model(9,10,11)
60	$pSmad2_{Cyt} + PPM1A_{Cyt} \underset{kbPPM1A}{\overset{kfPPM1A}{\rightleftharpoons}} pSmad2:PPM1A_{Cyt}$	Model(10,11)
61	$pSmad2:PPM1A_{Cyt} \xrightarrow{kdeph_{PPM1A}} Smad2_{Cyt} + PPM1A_{Cyt}$	Model(10,11)
62	$pSmad2_{Nuc} + PTEN:PPM1A_{Nuc} \underset{kbPPM1A}{\overset{kfPPM1A}{\rightleftharpoons}} pSmad2:PTEN:PPM1A_{Nuc}$	Model(10,11)
63	$pSmad2:PTEN:PPM1A_{Nuc} \xrightarrow{kdeph_{PPM1A}} Smad2_{Nuc} + PTEN:PPM1A_{Nuc}$	Model(10,11)
64	$pSmad2_{Cyt} + PTEN:PPM1A_{Cyt} \underset{kbPPM1A}{\overset{kfPPM1A}{\rightleftharpoons}} pSmad2:PTEN:PPM1A_{Cyt}$	Model(10,11)

65	$pSmad2:PTEN:PPM1A_{Cyt} \xrightarrow{kdeph_{PPM1A}} Smad2_{Cyt} + PTEN:PPM1A_{Cyt}$	Model(10,11)
66	$pSmad2_{Cyt} + PTEN_{Cyt} \underset{kbTEN}{\overset{kfPTEN}{\rightleftharpoons}} pSmad2:PTEN_{Cyt}$	Model(10,11)
67	$pSmad2:PTEN_{Cyt} + PPM1A_{Cyt} \underset{kbPP}{\overset{kfPP}{\rightleftharpoons}} pSmad2:PTEN:PPM1A_{Cyt}$	Model(10,11)
68	$pSmad2:PTEN:PPM1A_{Cyt} \xrightarrow{krPP} pSmad2_{Cyt} + PTEN:PPM1A_{Cyt}$	Model(10,11)
69	$PTEN:PPM1A_{Cyt} \xrightarrow{krPPM1A} PTEN_{Cyt} + PPM1A_{Cyt}$	Model(10,11)
70	$PTEN:PPM1A_{Nuc} \xrightarrow{krPPM1A} PTEN_{Nuc} + PPM1A_{Nuc}$	Model(10,11)
71	$PTEN:PPM1A_{Cyt} \underset{kexp_{PP}}{\overset{kimp_{PP}}{\rightleftharpoons}} PTEN:PPM1A_{Nuc}$	Model(10,11)
72	$PTEN_{Nuc} \xrightarrow{kexp_{PTEN}} PTEN_{Cyt}$	Model(10,11)
73	$LRC_{EE} + RI \underset{kbRI}{\overset{kfRI}{\rightleftharpoons}} LRC_{EE}:RI$	All

Table 8.4 Table of Negative Regulatory Mechanisms and Their Related Rate Constants

	R-Smad Dephosphorylation	Receptor Degradation	P-R-Smad Degradation	Endogenous Synthesis and Degrdation of R-Smad	Receptor Inhibitions	PPM1A Upregulation	PPM1A Stablization
$kdeph_{pSmad2}$	estimated	0	0	0	0	0	0
$kdeg_{pSmad2}$	0	0	estimated	estimated	0	0	0
v_{Smad2}	0	0	0	5.7143 $nMmin^{-1}$	0	0	0
$kdeg_{Smad2}$	0	0	0	0.01 min^{-1}	0	0	0
klid	0	estimated	0	0	0	0	0
kSmad7	0	0	0	0	estimated	0	0
$kfSmad7_{cave}$	0	0	0	0	estimated	0	0
$kbSmad7_{cave}$	0	0	0	0	estimated	0	0
$kfSmad7_{ee}$	0	0	0	0	estimated	0	0
$kbSmad7_{ee}$	0	0	0	0	estimated	0	0
$kdeph_{LRC}$	0	0	0	0	estimated	0	0
$kdeg_{LRC}$	0	0	0	0	estimated	0	0
v_{PPM1A}	0	0	0	0	0	estimated	estimated
$kdeg_{PPM1A}$	0	0	0	0	0	estimated	estimated
$kdeph_{PPM1A}$	0	0	0	0	0	estimated	estimated
kPPM1A	0	0	0	0	0	estimated	0
kfPPM1A	0	0	0	0	0	0	estimated
kbPPM1A	0	0	0	0	0	0	estimated
krPPM1A	0	0	0	0	0	0	estimated
kfPP	0	0	0	0	0	0	estimated
kbPP	0	0	0	0	0	0	estimated
kfPTEN	0	0	0	0	0	0	estimated
kbPTEN	0	0	0	0	0	0	estimated
$kimp_{PPM1A}$	0	0	0	0	0	0	estimated
$kimp_{PP}$	0	0	0	0	0	0	estimated
$kexp_{PP}$	0	0	0	0	0	0	estimated
$kexp_{PTEN}$	0	0	0	0	0	0	estimated

Table 8.5 Table of Estimated Parameters in Model 1-11. Model 8 is excluded from this table because multiple fitted models (with different parameters) were selected from the structure of Model 8. The underlined values have been manually tuned. All the others were estimated numerically with MATLAB fmincon optimization. The last parameter (for PTEN) is an initial concentration. All the other parameters are rate constants.

	Model 1	Model 2	Model 3	Model 4	Model 5	Model 6	Model 7	Model 9	Model 10	Model 11
$kLRC_1$ ($nM^{-1}min^{-1}$)	213.3	862.4	125.5	219.9	23.56	2388	34.11	0.9068	10.33	45.07
$kLRC_2$ ($nM^{-1}min^{-1}$)	3459	1218	4706	62.49	10.63	0.1182	1025	0.04956	0.7638	0.02404
kfSmad2 ($nM^{-1}min^{-1}$)	0.03958	0.02400	7.395e-4	0.1599	0.03533	0.6500	0.01185	0.9100	0.07978	1.873
krSmad2 ($nM^{-1}min^{-1}$)	2.443e5	35.22	2299	1332	7479	2.036e5	99.44	8183	317.8	4.543e3
kfSmadsComplex ($nM^{-1}min^{-1}$)	0.4670	5.871e-3	1.001e-3	2.586e-5	2.452e-4	3.122e-4	0.01329	1.074	0.1555	0.2867
krSmadsComplex ($nM^{-1}min^{-1}$)	0.2858	0.2927	0.1605	2.297e-3	0.03971	0.05235	0.1560	4.194	3.095	1.720
$kdeph_{pSmad2}$ (min^{-1})	999.6	0.3706	0	0	3.145	11.06	9.676	0	0	0
$kdeg_{pSmad2}$ (min^{-1})	0	0	0	0.6789	0.3058	0.9444	3.163	0	0	0.4516
v_{Smad2} ($nMmin^{-1}$)	0	0	0	0	0	0	5.714	0	0	5.714
$kdeg_{Smad2}$ (min^{-1})	0	0	0	0	0	0	0.01000	0	0	0.01000
klid ($nM^{-1}min^{-1}$)	0	0.01371	8.250e-3	0	5.231e-4	0	0	0	0	0
v_{PPM1A} ($nMmin^{-1}$)	0	0	0	0	0	0	0	0.1000	7.000	7.000
$kdeg_{PPM1A}$ (min^{-1})	0	0	0	0	0	0	0	0.01000	0.07000	0.07000
$kdeph_{PPM1A}$ (min^{-1})	0	0	0	0	0	0	0	0.3980	16.01	1.502
kPPM1A (min^{-1})	0	0	0	0	0	0	0	1.178e-3	0	0
kfPPM1A ($nM^{-1}min^{-1}$)	0	0	0	0	0	0	0	45.63	7.153e-3	0.2117
kbPPM1A (min^{-1})	0	0	0	0	0	0	0	7.354	1.088	6.500
krPPM1A (min^{-1})	0	0	0	0	0	0	0	0	1.137e-8	1.604e-7
kfPP ($nM^{-1}min^{-1}$)	0	0	0	0	0	0	0	0	66.60	2.422
kbPP (min^{-1})	0	0	0	0	0	0	0	0	5.457e-8	7.366e-8
krPP (min^{-1})	0	0	0	0	0	0	0	0	0.08566	0.4037
kfPTEN ($nM^{-1}min^{-1}$)	0	0	0	0	0	0	0	0	104.3	20.48
kbPTEN (min^{-1})	0	0	0	0	0	0	0	0	5.506e-7	6.788e-7
$kimp_{PPM1A}$ (min^{-1})	0	0	0	0	0	0	0	0	7.000	0.01406
$kimp_{PP}$ (min^{-1})	0	0	0	0	0	0	0	0	2.861e-3	1.978e-3
$kexp_{PP}$ (min^{-1})	0	0	0	0	0	0	0	0	2.180e-7	1.145e-7
$kexp_{PTEN}$ (min^{-1})	0	0	0	0	0	0	0	0	0.5330	0.03268
$PTEN_{Cyt}$ (nM)	0	0	0	0	0	0	0	0	180.3	174.9

8.2 Appendix for Chapter 4

8.2.1 Derivation of the Jacobian Matrix of the Population ODE

8.2.1.1 Derivation of Each Block in the Jacobian Matrix

The Jacobian Matrix of the Population ODE can be divided into four blocks as shown in Equation (4.19) and the result of the derivation of all blocks are shown in Equation (4.20) to (4.23). Here we show how these equations are derived.

One rule that we applied for our derivation is chain rule for the differentiation of the kronecker product of two vectors.

$$\frac{\partial \boldsymbol{a} \otimes \boldsymbol{b}}{\partial \boldsymbol{c}} = \boldsymbol{a} \otimes \frac{\partial \boldsymbol{b}}{\partial \boldsymbol{c}} + \frac{\partial \boldsymbol{a}}{\partial \boldsymbol{c}} \otimes \boldsymbol{b} \tag{8.1}$$

For Equation (4.20), we differentiate $\boldsymbol{F}_{\boldsymbol{\mu}}$ with respect to $\boldsymbol{\mu}$

$$\begin{aligned} \frac{\partial \boldsymbol{F}_{\boldsymbol{\mu}}}{\partial \boldsymbol{\mu}} &= \frac{\partial [\boldsymbol{A}^{\boldsymbol{1}}\boldsymbol{\mu} + \boldsymbol{A}^{\boldsymbol{2}}\boldsymbol{\mu} \otimes \boldsymbol{\mu} + \boldsymbol{A}^{\boldsymbol{2}} vec(\boldsymbol{C}^T)]}{\partial \boldsymbol{\mu}} \\ &= \boldsymbol{A}^{\boldsymbol{1}} + \boldsymbol{A}^{\boldsymbol{2}}(\boldsymbol{\mu} \otimes \frac{\partial \boldsymbol{\mu}}{\partial \boldsymbol{\mu}} + \frac{\partial \boldsymbol{\mu}}{\partial \boldsymbol{\mu}} \otimes \boldsymbol{\mu}) \\ &= \boldsymbol{A}^{\boldsymbol{1}} + \boldsymbol{A}^{\boldsymbol{2}}(\boldsymbol{\mu} \otimes \boldsymbol{I} + \boldsymbol{I} \otimes \boldsymbol{\mu}) \end{aligned} \tag{8.2}$$

For Equation (4.21), we differentiate $\boldsymbol{F}_{\boldsymbol{\mu}}$ with respect to $vec(\boldsymbol{C}^T)$

$$\begin{aligned} \frac{\partial \boldsymbol{F}_{\boldsymbol{\mu}}}{\partial vec(\boldsymbol{C}^T)} &= \frac{\partial [\boldsymbol{A}^{\boldsymbol{1}}\boldsymbol{\mu} + \boldsymbol{A}^{\boldsymbol{2}}\boldsymbol{\mu} \otimes \boldsymbol{\mu} + \boldsymbol{A}^{\boldsymbol{2}} vec(\boldsymbol{C}^T)]}{\partial vec(\boldsymbol{C}^T)} \\ &= \boldsymbol{A}^{\boldsymbol{2}} \end{aligned} \tag{8.3}$$

For Equation (4.22), we differentiate $\boldsymbol{F}_{\boldsymbol{C}}$ with respect to $\boldsymbol{\mu}$

$$\begin{aligned}\frac{\partial \boldsymbol{F}_C}{\partial \boldsymbol{\mu}} &= \cancel{\frac{\partial[(\boldsymbol{A}^1 \otimes \boldsymbol{I} + \boldsymbol{I} \otimes \boldsymbol{A}^1) vec(\boldsymbol{C}^T)]}{\partial \boldsymbol{\mu}}} \\ &+ \frac{\partial\{(\boldsymbol{A}^2 \otimes \boldsymbol{I})[\boldsymbol{\mu} \otimes vec(\boldsymbol{C}^T) + vec(\boldsymbol{\mu} \otimes \boldsymbol{C}^T)]\}}{\partial \boldsymbol{\mu}} \\ &+ \frac{\partial\{(\boldsymbol{I} \otimes \boldsymbol{A}^2)[vec(\boldsymbol{C}) \otimes \boldsymbol{\mu} + vec(\boldsymbol{\mu} \otimes \boldsymbol{C}^T)]\}}{\partial \boldsymbol{\mu}}\end{aligned} \tag{8.4}$$

Please note that

$$\begin{aligned}\frac{\partial vec(\boldsymbol{\mu} \otimes \boldsymbol{C}^T)}{\partial \boldsymbol{\mu}} &= \frac{\partial E(\boldsymbol{\delta} \otimes \boldsymbol{\mu} \otimes \boldsymbol{\delta})}{\partial \boldsymbol{\mu}} \\ &= E\left(\boldsymbol{\delta} \otimes \boldsymbol{\mu} \otimes \cancel{\frac{\partial \boldsymbol{\delta}}{\partial \boldsymbol{\mu}}} + \frac{\partial \boldsymbol{\delta} \otimes \boldsymbol{\mu}}{\partial \boldsymbol{\mu}} \otimes \boldsymbol{\delta} \right) \\ &= E\left[\left(\boldsymbol{\delta} \otimes \frac{\partial \boldsymbol{\mu}}{\partial \boldsymbol{\mu}} + \cancel{\frac{\partial \boldsymbol{\delta}}{\partial \boldsymbol{\mu}}} \otimes \boldsymbol{\mu} \right) \otimes \boldsymbol{\delta} \right] \\ &= E(\boldsymbol{\delta} \otimes \boldsymbol{I} \otimes \boldsymbol{\delta})\end{aligned} \tag{8.5}$$

Therefore, we have

$$\begin{aligned}\frac{\partial \boldsymbol{F}_C}{\partial \boldsymbol{\mu}} &= (\boldsymbol{A}^2 \otimes \boldsymbol{I}) \left[\frac{\partial \boldsymbol{\mu} \otimes vec(\boldsymbol{C}^T)}{\partial \boldsymbol{\mu}} + E(\boldsymbol{\delta} \otimes \boldsymbol{I} \otimes \boldsymbol{\delta}) \right] \\ &+ (\boldsymbol{I} \otimes \boldsymbol{A}^2) \left[\frac{\partial vec(\boldsymbol{C}^T) \otimes \boldsymbol{\mu}}{\partial \boldsymbol{\mu}} + E(\boldsymbol{\delta} \otimes \boldsymbol{I} \otimes \boldsymbol{\delta}) \right] \\ &= (\boldsymbol{A}^2 \otimes \boldsymbol{I}) \left[\boldsymbol{\mu} \otimes \cancel{\frac{\partial vec(\boldsymbol{C}^T)}{\partial \boldsymbol{\mu}}} + \frac{\partial \boldsymbol{\mu}}{\partial \boldsymbol{\mu}} \otimes vec(\boldsymbol{C}^T) + E(\boldsymbol{\delta} \otimes \boldsymbol{I} \otimes \boldsymbol{\delta}) \right] \\ &+ (\boldsymbol{I} \otimes \boldsymbol{A}^2) \left[vec(\boldsymbol{C}^T) \otimes \frac{\partial \boldsymbol{\mu}}{\partial \boldsymbol{\mu}} + \cancel{\frac{\partial vec(\boldsymbol{C}^T)}{\partial \boldsymbol{\mu}}} \otimes \boldsymbol{\mu} + E(\boldsymbol{\delta} \otimes \boldsymbol{I} \otimes \boldsymbol{\delta}) \right] \\ &= (\boldsymbol{A}^2 \otimes \boldsymbol{I}) \left[\boldsymbol{I} \otimes vec(\boldsymbol{C}^T) + E(\boldsymbol{\delta} \otimes \boldsymbol{I} \otimes \boldsymbol{\delta}) \right] \\ &+ (\boldsymbol{I} \otimes \boldsymbol{A}^2) \left[vec(\boldsymbol{C}^T) \otimes \boldsymbol{I} + E(\boldsymbol{\delta} \otimes \boldsymbol{I} \otimes \boldsymbol{\delta}) \right]\end{aligned} \tag{8.6}$$

For Equation (4.23), we differentiate $\boldsymbol{F}_C$ with respect to $vec(\boldsymbol{C}^T)$

$$\begin{aligned}\frac{\partial \boldsymbol{F}_C}{\partial vec(\boldsymbol{C}^T)} &= \frac{\partial[(\boldsymbol{A^1}\otimes\boldsymbol{I}+\boldsymbol{I}\otimes\boldsymbol{A^1})vec(\boldsymbol{C}^T)]}{\partial vec(\boldsymbol{C}^T)} \\ &+\frac{\partial\{(\boldsymbol{A^2}\otimes\boldsymbol{I})[\boldsymbol{\mu}\otimes vec(\boldsymbol{C}^T)+vec(\boldsymbol{\mu}\otimes\boldsymbol{C}^T)]\}}{\partial vec(\boldsymbol{C}^T)} \\ &+\frac{\partial\{(\boldsymbol{I}\otimes\boldsymbol{A^2})[vec(\boldsymbol{C}^T)\otimes\boldsymbol{\mu}+vec(\boldsymbol{\mu}\otimes\boldsymbol{C}^T)]\}}{\partial vec(\boldsymbol{C}^T)}\end{aligned} \tag{8.7}$$

Applying the chain rule in Equation (8.1), we have

$$\begin{cases}\dfrac{\partial \boldsymbol{\mu}\otimes vec(\boldsymbol{C}^T)}{\partial vec(\boldsymbol{C}^T)} = \boldsymbol{\mu}\otimes\boldsymbol{I}^{\boldsymbol{2}}_{n^2\times n^2} = \boldsymbol{\mu}\otimes\boldsymbol{I}\otimes\boldsymbol{I} \\ \dfrac{\partial vec(\boldsymbol{C}^T)\otimes\boldsymbol{\mu}}{\partial vec(\boldsymbol{C}^T)} = \boldsymbol{I}^{\boldsymbol{2}}_{n^2\times n^2}\otimes\boldsymbol{\mu} = \boldsymbol{I}\otimes\boldsymbol{I}\otimes\boldsymbol{\mu}\end{cases} \tag{8.8}$$

To derive $\dfrac{\partial vec(\boldsymbol{\mu}\otimes\boldsymbol{C}^T)}{\partial vec(\boldsymbol{C}^T)}$, we denote $\boldsymbol{C}^T$ as in its column vectors

$$\boldsymbol{C}^T = \begin{pmatrix} \boldsymbol{c}_1 & \cdots & \boldsymbol{c}_n \end{pmatrix}_{n\times n}, \quad \boldsymbol{c}_i = \begin{pmatrix} E(\delta_i\delta_1) \\ \vdots \\ E(\delta_i\delta_n) \end{pmatrix}_{n\times 1} \tag{8.9}$$

Then applying the chain rule in Equation (8.1), we have

$$\begin{aligned}\frac{\partial vec(\boldsymbol{\mu}\boldsymbol{C}^T)}{\partial vec(\boldsymbol{C}^T)} &= \partial\begin{pmatrix} \boldsymbol{\mu}\otimes\boldsymbol{c}_1 \\ \vdots \\ \boldsymbol{\mu}\otimes\boldsymbol{c}_n \end{pmatrix} / \partial vec(\boldsymbol{C}^T) \\ &= \begin{pmatrix} \dfrac{\partial\boldsymbol{\mu}\otimes\boldsymbol{c}_1}{\partial\boldsymbol{c}_1} & \boldsymbol{0} & \boldsymbol{0} \\ \boldsymbol{0} & \ddots & \boldsymbol{0} \\ \boldsymbol{0} & \boldsymbol{0} & \dfrac{\partial\boldsymbol{\mu}\otimes\boldsymbol{c}_n}{\partial\boldsymbol{c}_n} \end{pmatrix} \\ &= \begin{pmatrix} \boldsymbol{\mu}\otimes\boldsymbol{I} & \boldsymbol{0} & \boldsymbol{0} \\ \boldsymbol{0} & \ddots & \boldsymbol{0} \\ \boldsymbol{0} & \boldsymbol{0} & \boldsymbol{\mu}\otimes\boldsymbol{I} \end{pmatrix} \\ &= \boldsymbol{I}\otimes\boldsymbol{\mu}\otimes\boldsymbol{I}\end{aligned} \tag{8.10}$$

Substituting the derivatives in Equation (8.7) using Equation (8.8) and (8.10), we have Equation (4.23) derived as

$$\begin{aligned}\frac{\partial \boldsymbol{F}_C}{\partial vec(\boldsymbol{C}^T)} &= (\boldsymbol{A}^1 \otimes \boldsymbol{I} + \boldsymbol{I} \otimes \boldsymbol{A}^1) \\ &+(\boldsymbol{A}^2 \otimes \boldsymbol{I})(\boldsymbol{\mu} \otimes \boldsymbol{I} \otimes \boldsymbol{I} + \boldsymbol{I} \otimes \boldsymbol{\mu} \otimes \boldsymbol{I}) \\ &+(\boldsymbol{I} \otimes \boldsymbol{A}^2)(\boldsymbol{I} \otimes \boldsymbol{\mu} \otimes \boldsymbol{I} + \boldsymbol{I} \otimes \boldsymbol{I} \otimes \boldsymbol{\mu})\end{aligned} \tag{8.11}$$

8.2.1.2 Simplification of Equation (4.22)

Equation (4.22) can be separated into four terms as below, and we simplify each term individually.

$$\begin{aligned}&\frac{\partial \boldsymbol{F}_C}{\partial \boldsymbol{\mu}} = \boldsymbol{T}^1 + \boldsymbol{T}^2 + \boldsymbol{T}^3 + \boldsymbol{T}^4 \\ &\begin{cases}\boldsymbol{T}^1 = (\boldsymbol{A}^2 \otimes \boldsymbol{I})[\boldsymbol{I} \otimes vec(\boldsymbol{C}^T)] \\ \boldsymbol{T}^2 = (\boldsymbol{A}^2 \otimes \boldsymbol{I})E(\boldsymbol{\delta} \otimes \boldsymbol{I} \otimes \boldsymbol{\delta}) \\ \boldsymbol{T}^3 = (\boldsymbol{I} \otimes \boldsymbol{A}^2)E(\boldsymbol{\delta} \otimes \boldsymbol{I} \otimes \boldsymbol{\delta}) \\ \boldsymbol{T}^4 = (\boldsymbol{I} \otimes \boldsymbol{A}^2)[vec(\boldsymbol{C}^T) \otimes \boldsymbol{I}]\end{cases}\end{aligned} \tag{8.12}$$

For simplification of these four terms, we need to write $\boldsymbol{A}^2$ as a block matrix

$$\boldsymbol{A}^2 = \begin{pmatrix} \boldsymbol{B}_1 & \cdots & \boldsymbol{B}_n \end{pmatrix}_{n \times n^2}, \quad \boldsymbol{B}_k = \begin{pmatrix} \boldsymbol{A}^2_{1,(k-1)n+1} & \cdots & \boldsymbol{A}^2_{1,kn} \\ \vdots & \ddots & \vdots \\ \boldsymbol{A}^2_{n,(k-1)n+1} & \cdots & \boldsymbol{A}^2_{n,kn} \end{pmatrix}_{n \times n} \tag{8.13}$$

and to write $\boldsymbol{C}^T$ as a block matrix (same as that in Equation (8.9))

$$\boldsymbol{C}^T = \begin{pmatrix} \boldsymbol{c}_1 & \cdots & \boldsymbol{c}_n \end{pmatrix}_{n \times n}, \quad \boldsymbol{c}_i = \begin{pmatrix} E(\delta_i \delta_1) \\ \vdots \\ E(\delta_i \delta_n) \end{pmatrix}_{n \times 1} \tag{8.14}$$

Please note that

$$E(\boldsymbol{\delta}\otimes\boldsymbol{I}\otimes\boldsymbol{\delta})=\begin{pmatrix} E[\delta_1(\boldsymbol{I}\otimes\boldsymbol{\delta})] \\ \vdots \\ E[\delta_n(\boldsymbol{I}\otimes\boldsymbol{\delta})] \end{pmatrix}=\begin{pmatrix} \boldsymbol{I}\otimes E(\delta_1\boldsymbol{\delta}) \\ \vdots \\ \boldsymbol{I}\otimes E(\delta_n\boldsymbol{\delta}) \end{pmatrix}=\begin{pmatrix} \boldsymbol{I}\otimes\boldsymbol{c}_1 \\ \vdots \\ \boldsymbol{I}\otimes\boldsymbol{c}_n \end{pmatrix} \tag{8.15}$$

Then we can simplify the first term $\boldsymbol{T^1}$ as

$$\begin{aligned} \boldsymbol{T^1} &= (\boldsymbol{A^2}\otimes\boldsymbol{I})[\boldsymbol{I}\otimes vec(\boldsymbol{C}^T)] \\ &= \begin{pmatrix} \boldsymbol{B}_1\otimes\boldsymbol{I} & \cdots & \boldsymbol{B}_n\otimes\boldsymbol{I} \end{pmatrix}\begin{bmatrix} vec(\boldsymbol{C}^T) & \boldsymbol{0} & \boldsymbol{0} \\ \boldsymbol{0} & \ddots & \boldsymbol{0} \\ \boldsymbol{0} & \boldsymbol{0} & vec(\boldsymbol{C}^T) \end{bmatrix} \\ &= \begin{bmatrix} (\boldsymbol{B}_1\otimes\boldsymbol{I})vec(\boldsymbol{C}^T) & \cdots & (\boldsymbol{B}_n\otimes\boldsymbol{I})vec(\boldsymbol{C}^T) \end{bmatrix} \end{aligned} \tag{8.16}$$

Applying the rule $vec(\boldsymbol{AB})=(\boldsymbol{B}^T\otimes\boldsymbol{I})\boldsymbol{A}$, we have

$$\boldsymbol{T^1}=\begin{bmatrix} vec(\boldsymbol{C}^T\boldsymbol{B}_1^T) & \cdots & vec(\boldsymbol{C}^T\boldsymbol{B}_n^T) \end{bmatrix} \tag{8.17}$$

We can simplify the second term $\boldsymbol{T^2}$ as

$$\begin{aligned} \boldsymbol{T^2} &= (\boldsymbol{A^2}\otimes\boldsymbol{I})E(\boldsymbol{\delta}\otimes\boldsymbol{I}\otimes\boldsymbol{\delta}) \\ &= \begin{pmatrix} \boldsymbol{B}_1\otimes\boldsymbol{I} & \cdots & \boldsymbol{B}_n\otimes\boldsymbol{I} \end{pmatrix}\begin{pmatrix} \boldsymbol{I}\otimes\boldsymbol{c}_1 \\ \vdots \\ \boldsymbol{I}\otimes\boldsymbol{c}_n \end{pmatrix} \\ &= \sum_{k=1}^{n}(\boldsymbol{B}_k\otimes\boldsymbol{I})(\boldsymbol{I}\otimes\boldsymbol{c}_k) \end{aligned} \tag{8.18}$$

Applying the rule $(\boldsymbol{A}\otimes\boldsymbol{B})(\boldsymbol{C}\otimes\boldsymbol{D})=(\boldsymbol{AC})\otimes(\boldsymbol{BD})$, we have

$$\boldsymbol{T^2}=\sum_{k=1}^{n}\boldsymbol{B}_k\otimes\boldsymbol{c}_k \tag{8.19}$$

We can simplify the third term $\boldsymbol{T^3}$ as

$$
\begin{aligned}
\boldsymbol{T^3} &= (\boldsymbol{I} \otimes \boldsymbol{A^2}) E(\boldsymbol{\delta} \otimes \boldsymbol{I} \otimes \boldsymbol{\delta}) \\
&= \begin{pmatrix} \boldsymbol{A^2} & \boldsymbol{0} & \boldsymbol{0} \\ \boldsymbol{0} & \ddots & \boldsymbol{0} \\ \boldsymbol{0} & \boldsymbol{0} & \boldsymbol{A^2} \end{pmatrix} \begin{pmatrix} \boldsymbol{I} \otimes \boldsymbol{c}_1 \\ \vdots \\ \boldsymbol{I} \otimes \boldsymbol{c}_n \end{pmatrix} \\
&= \begin{pmatrix} \boldsymbol{A^2}(\boldsymbol{I} \otimes \boldsymbol{c}_1) \\ \vdots \\ \boldsymbol{A^2}(\boldsymbol{I} \otimes \boldsymbol{c}_1) \end{pmatrix}
\end{aligned} \tag{8.20}
$$

The k-th row in $\boldsymbol{T^3}$ is

$$
\begin{aligned}
\boldsymbol{T^3_{k,:}} &= \boldsymbol{A^2}(\boldsymbol{I} \otimes \boldsymbol{c}_k) \\
&= \begin{pmatrix} \boldsymbol{B}_1 & \cdots & \boldsymbol{B}_n \end{pmatrix} \begin{pmatrix} \boldsymbol{c}_k & \boldsymbol{0} & \boldsymbol{0} \\ \boldsymbol{0} & \ddots & \boldsymbol{0} \\ \boldsymbol{0} & \boldsymbol{0} & \boldsymbol{c}_k \end{pmatrix} \\
&= \begin{pmatrix} \boldsymbol{B}_1\boldsymbol{c}_k & \cdots & \boldsymbol{B}_n\boldsymbol{c}_k \end{pmatrix}
\end{aligned} \tag{8.21}
$$

We can simplify the fourth term $\boldsymbol{T^4}$ as

$$
\begin{aligned}
\boldsymbol{T^4} &= (\boldsymbol{I} \otimes \boldsymbol{A^2})[vec(\boldsymbol{C}^T) \otimes \boldsymbol{I}] \\
&= \begin{pmatrix} \boldsymbol{A^2} & \boldsymbol{0} & \boldsymbol{0} \\ \boldsymbol{0} & \ddots & \boldsymbol{0} \\ \boldsymbol{0} & \boldsymbol{0} & \boldsymbol{A^2} \end{pmatrix} \begin{pmatrix} \boldsymbol{c}_1 \otimes \boldsymbol{I} \\ \vdots \\ \boldsymbol{c}_n \otimes \boldsymbol{I} \end{pmatrix} \\
&= \begin{pmatrix} \boldsymbol{A^2}(\boldsymbol{c}_1 \otimes \boldsymbol{I}) \\ \vdots \\ \boldsymbol{A^2}(\boldsymbol{c}_n \otimes \boldsymbol{I}) \end{pmatrix}
\end{aligned} \tag{8.22}
$$

Thus, all four terms of $\dfrac{\partial \boldsymbol{F}_C}{\partial \boldsymbol{\mu}}$ have been simplified for computation. The largest matrix needed for computation has the size of n^3, which is much smaller than that without simplification (n^5).

8.2.1.3 Simplification of Equation (4.23)

Applying the rule $(\boldsymbol{A}\otimes\boldsymbol{B})(\boldsymbol{C}\otimes\boldsymbol{D})=(\boldsymbol{AC})\otimes(\boldsymbol{BD})$, and because kronecker product is bilinear, the Equation (4.23) can be written as

$$\begin{aligned}\frac{\partial \boldsymbol{F}_C}{\partial vec(\boldsymbol{C}^T)} &= (\boldsymbol{A}^1\otimes\boldsymbol{I}+\boldsymbol{I}\otimes\boldsymbol{A}^1)\\ &\quad+(\boldsymbol{A}^2\otimes\boldsymbol{I})(\boldsymbol{\mu}\otimes\boldsymbol{I}\otimes\boldsymbol{I}+\boldsymbol{I}\otimes\boldsymbol{\mu}\otimes\boldsymbol{I})\\ &\quad+(\boldsymbol{I}\otimes\boldsymbol{A}^2)(\boldsymbol{I}\otimes\boldsymbol{\mu}\otimes\boldsymbol{I}+\boldsymbol{I}\otimes\boldsymbol{I}\otimes\boldsymbol{\mu})\\ &= (\boldsymbol{A}^1\otimes\boldsymbol{I}+\boldsymbol{I}\otimes\boldsymbol{A}^1)\\ &\quad+[\boldsymbol{A}^2(\boldsymbol{\mu}\otimes\boldsymbol{I}+\boldsymbol{I}\otimes\boldsymbol{\mu})]\otimes\boldsymbol{I}\\ &\quad+\boldsymbol{I}\otimes[\boldsymbol{A}^2(\boldsymbol{\mu}\otimes\boldsymbol{I}+\boldsymbol{I}\otimes\boldsymbol{\mu})]\\ &= [\boldsymbol{A}^1+\boldsymbol{A}^2(\boldsymbol{\mu}\otimes\boldsymbol{I}+\boldsymbol{I}\otimes\boldsymbol{\mu})]\otimes\boldsymbol{I}\\ &\quad+\boldsymbol{I}\otimes[\boldsymbol{A}^1+\boldsymbol{A}^2(\boldsymbol{\mu}\otimes\boldsymbol{I}+\boldsymbol{I}\otimes\boldsymbol{\mu})]\\ &= \frac{\partial \boldsymbol{F}_{\boldsymbol{\mu}}}{\partial \boldsymbol{\mu}}\otimes\boldsymbol{I}+\boldsymbol{I}\otimes\frac{\partial \boldsymbol{F}_{\boldsymbol{\mu}}}{\partial \boldsymbol{\mu}}\end{aligned} \tag{8.23}$$

This simplification allow us to use the previous calculated matrix $\frac{\partial \boldsymbol{F}_{\boldsymbol{\mu}}}{\partial \boldsymbol{\mu}}$ and it has only the size of n^2 which is much smaller than that without simplification (n^5).